Human iPSC-derived cerebral organoids model features of Leigh Syndrome and reveal abnormal corticogenesis

Alejandra I. Romero-Morales[1], Gabriella L. Robertson[1], Anuj Rastogi[1], Megan L. Rasmussen[1], Hoor Temuri[1], Gregory Scott McElroy[3], Ram Prosad Chakrabarty[3], Lawrence Hsu[2], Paula M. Almonacid[4], Bryan A. Millis[1,5], Navdeep S. Chandel[3,6], Jean-Philippe Cartailler[2], and Vivian Gama[1,2,7]

[1]Vanderbilt University, Cell and Developmental Biology, Nashville, TN.
[2]Vanderbilt University, Creative Data Solutions, Vanderbilt Center for Stem Cell Biology, Nashville, TN
[3]Northwestern University, Feinberg School of Medicine Department of Medicine Division of Pulmonary and Critical Care Medicine, Chicago, IL
[4]Universidad EAFIT, School of Economics and Finances, Colombia
[5]Vanderbilt University, Vanderbilt Biophotonics Center, Nashville, TN
[6]Northwestern University, Feinberg School of Medicine Department of Biochemistry and Molecular Genetics, Chicago, IL
[7]Vanderbilt University, Vanderbilt Brain Institute, Nashville, TN

Corresponding author

Correspondence should be addressed to:

Vivian Gama
PMB407935
465 21st Avenue South, 4150A
Vanderbilt University
Nashville, TN 37240-7935
Tel: (615) 875-9490
vivian.gama@vanderbilt.edu

Running title: Modeling the effect of Leigh syndrome-associated mutations using human cerebral organoids

Keywords: Leigh syndrome, stem cells, mitochondria, neural precursor cells, neural rosettes, brain organoids

Summary

Leigh syndrome (LS) is a rare, inherited neurometabolic disorder that presents with bilateral brain lesions, caused by defects in the mitochondrial respiratory chain and associated nuclear-encoded proteins. We generated iPSCs from three patient-derived LS fibroblast lines and identified, by whole-exome and mitochondrial sequencing, unreported mutations in pyruvate dehydrogenase (GM0372, PDH; GM13411, MT-ATP6/PDH) and dihydrolipoyl dehydrogenase (GM01503, DLD). LS-derived iPSC lines were viable and generally capable of differentiating into key progenitor populations, but we identified several abnormalities in three-dimensional differentiation models of brain development. LS-derived cerebral organoids showed defects in neural epithelial bud generation, size, and cortical architecture at 100 days. The double mutant MT-ATP6/PDH line produced organoid neural progenitor cells with abnormal mitochondrial morphology characterized by fragmentation and disorganization and showed an increased generation of astrocytes. These studies aim to provide a comprehensive phenotypic characterization of available patient-derived cell lines that can be used as LS model systems.

67 **Introduction**

68 Leigh syndrome (LS), or sub-acute necrotizing encephalomyelopathy, is an inherited
69 neurometabolic disorder that affects the central nervous system (CNS) (Baertling et al., 2014;
70 Gerards et al., 2016; Leigh, 1951; Sorbi and Blass, 1982). LS is a rare, progressive, early-onset
71 disease with a prevalence of 1 in 40,000 live births (Lake et al., 2016). The pathologic features of
72 LS are focal, bilateral lesions in one or more areas of the CNS, including the brainstem, thalamus,
73 basal ganglia, cerebellum, and spinal cord. The most common underlying cause is defective
74 oxidative phosphorylation (OXPHOS), due to mutations in genes encoding complexes of the
75 mitochondrial respiratory chain (Baertling et al., 2014; Lake et al., 2015, 2016). The LS phenotype
76 caused by mitochondrial-encoded gene mutations can be rescued by mitochondrial replacement,
77 highlighting the importance of this organelle in LS disease progression (Ma et al., 2015).

78 The availability of animal models and brain tissue from biopsies has provided critical insight
79 into this disease. However, our understanding of the etiology and pathology of complex
80 neurological diseases like LS would benefit from human-derived platforms such as induced
81 pluripotent stem cell-derived models (Inak et al., 2021; Lorenz et al., 2017; Quadrato et al., 2016).
82 The ability to reprogram somatic cells into induced pluripotent stem cells (iPSCs), followed by
83 differentiation into specific lineages has become a useful tool for complex disease modeling
84 (Kelava and Lancaster, 2016; Di Lullo and Kriegstein, 2017; Pașca, 2018; Quadrato et al., 2016).
85 In the context of LS, iPSCs have been successfully generated from patients with mutations in
86 mitochondrially encoded ATP Synthase Membrane Subunit 6 (MT-ATP6) (Galera-Monge et al.,
87 2016; Grace et al., 2019; Lorenz et al., 2017; Ma et al., 2015), mitochondrially encoded
88 NADH:Ubiquinone Oxidoreductase Core Subunit 3 (MT-ND3) subunit (Hattori et al., 2016) and
89 the nuclear-encoded gene Surfeit locus protein 1 (SURF1) (Inak et al., 2019, 2021). These iPSC-
90 model systems have been proposed for drug discovery (Inak et al., 2017; Lorenz et al., 2017) as
91 well as testing platforms for potential metabolic rescue treatments (Ma et al., 2015).

92 Many studies have used LS patient fibroblasts commercially available at the Coriell Institute
93 (Galera-Monge et al., 2016; Hinman et al., 1989; Huh et al., 1990; Iyer et al., 2012; Johnson et
94 al., 2019; Ma et al., 2015; Sorbi and Blass, 1982; Vo et al., 2007; Zheng et al., 2016a). Here we
95 report our findings on the genomic and phenotypic characterization of iPSCs derived from these
96 three LS fibroblast lines. Whole exome and mitochondrial sequencing revealed previously
97 unidentified mutations in these patient-derived cell lines. Three-dimensional differentiation of
98 these LS mutant iPSCs into neural rosettes and cerebral organoids resulted in severe
99 abnormalities. LS-iPSC-derived 100-day cerebral organoids showed decreased size as well as
100 defects in the generation of neural epithelial buds. Corticogenesis was impaired in all LS mutant
101 cell lines. MT-ATP6/PDH showed a decrease in gene expression in neural progenitor and cortical
102 plate markers at day 30, while all three LS lines showed a reduction of the cortical layer markers
103 CTIP2, TBR1, SATB2, and BRN2 at day 100. These results point to aberrant corticogenesis as a
104 driver of LS pathogenesis and demonstrate the utility of iPSC-derived systems to recapitulate
105 CNS phenotypes and to test potential strategies to restore neurogenesis in LS.
106

107 **Results**

108 **Genomic characterization of Leigh syndrome fibroblasts.**

109 Due to the limited genomic information available for the three cell lines, we performed whole-
110 exome sequencing (WES) and mitochondrial sequencing of the fibroblasts before reprogramming
111 (Figure 1A-D and Supplemental Figure 1; data repository with the raw and analyzed WES and
112 mitochondrial results can be found at https://www.ncbi.nlm.nih.gov/sra/PRJNA626388 &
113 https://vandydata.github.io/Romero-Morales-Gama-Leigh-Syndrome-WES/). Comparison
114 between the high impact, moderate impact, and all variants for identified INDELs and SNPs
115 showed a significant overlap between the three cell lines (Supplemental Figure 1A & B). In-depth
116 analysis of the top 15 high-impact SNPs (Supplemental Figure 1C) also confirmed an overlap
117 between genotypes, with only three genes with confirmed SNPs related to neurological diseases

118 (*FRG2C* for bipolar disorder and *CDC27* and *KIR2DL4* for white matter microstructure
119 measurements) (Buniello et al., 2019).

120 Targeted analysis of the genes associated with Leigh syndrome (Lake et al., 2016) revealed
121 a loss of function insertion/deletion (INDEL) frameshift in pyruvate dehydrogenase complex
122 (PDHc) E1 alpha 1 subunit or pyruvate dehydrogenase (PDHA1, c.79delC, p.Arg27fs) in the cell
123 lines GM03672 and GM13411 (Figure 1E). A single-nucleotide polymorphism (SNP) in the PDHc
124 E3 subunit or dihydrolipoyl dehydrogenase (DLD, c.100A>G, p.Thr34Ala) was identified in
125 GM01503 (Figure 1E). In addition to being part of the PDHc, DLD is also a component of the α-
126 ketoglutarate and branched-chain α-ketoacid dehydrogenase complexes (Craigen, 1996).
127 Despite the lack of genomic data, dysfunction of the PDH complex was previously suggested in
128 GM03672 and GM01503 as the main driver of the disease in these patients (Hinman et al., 1989;
129 Huh et al., 1990; Sorbi and Blass, 1982) (Supplemental Table 1). To our knowledge, mutations in
130 the nuclear genome of GM13411 have not been reported to date.

131 Mitochondrial sequencing identified several SNPs in all the cell lines (Figure 1D). A loss of
132 function SNP in the MT-ATP6 gene was identified in the GM13411 line. This mutation was
133 reported in the original clinical case (Pastores et al., 1994). The authors described the T to G
134 transition at the 8993 position that results in the substitution of a highly conserved leucine residue
135 for an arginine (L156R). MT-ATP6 is part of the F0 domain of ATP synthase that functions as a
136 proton channel (Figure 1E). The L156R substitution prevents the induction of c-ring rotation
137 (rotation of an oligomeric assembly of c-subunits of the ATP synthase (Kühlbrandt and Davies,
138 2016)), resulting in decreased ATP synthesis (Uittenbogaard et al., 2018). Heteroplasmy analysis
139 of fibroblasts showed a 92% frequency of this mutation in the cell population, which is consistent
140 with previous reports (Galera-Monge et al., 2016; Iyer et al., 2012; Pastores et al., 1994).

141

142 **Characterization of iPSCs derived from commercially available Leigh syndrome**
143 **fibroblasts.**

144 Metabolic remodeling is a crucial step toward reprogramming somatic cells into iPSCs
145 (Mathieu and Ruohola-Baker, 2017; Panopoulos et al., 2012; Rasmussen and Gama, 2020;
146 Rastogi et al., 2019; Wu et al., 2016). Reprogramming of fibroblasts was performed as previously
147 described (Takahashi et al., 2007) (Supplemental Figure 2A); we generated iPSC clones from a
148 healthy age-matched control and the three LS cell lines. Pluripotency was evaluated using the
149 microarray-based analysis PluriTest (Müller et al., 2011). All three LS cell lines showed a high
150 pluripotency score and a low novelty score (Supplemental Figure 2B-C), congruent with the
151 transcriptional profile of pluripotent stem cells. Moreover, all the reprogrammed cells expressed
152 the pluripotent markers *NANOG* and *POU5F1* (*OCT4)* (Supplemental Figure 2D) and had a
153 normal karyotype. The MT-ATP6/PDH cell line showed increased levels of NANOG ($p<0.0001$)
154 compared to the control.

155 To assess the ability of the LS and control cell lines to differentiate into the three germ layers,
156 we performed trilineage differentiation as previously described (Kuang et al., 2019; Roberts et al.,
157 2019). Commitment to ectodermal fate was evaluated by immunofluorescence staining of the
158 marker PAX6 (Figure 2A and B), as well as the mRNA expression of the genes *GATA3* and *PAX6*
159 using RT-qPCR (Figure 2C). The endoderm lineage was assessed by protein expression of the
160 marker SOX17 (Figure 2A and B) and by the expression of the genes *CDX2* and *SOX17* (Figure
161 2C). Finally, mesodermal lineage was confirmed by the staining of the protein markers Brachyury
162 and CXCR4 (Figure 2A and B) and the expression of the genes *TBXT* and *NCAM* (Figure 2C).
163 No significant differences were detected among the different lines when compared to control.
164 Clinical data available from the patient with the PDH mutation reports elevated blood pyruvate
165 levels (Schubert and Vilarinho, 2020; Sofou et al., 2014). High concentrations of pyruvate in the
166 media have been shown to potentiate the differentiation of human embryonic stem cells (hESCs)
167 into endodermal and mesodermal lineages in a lineage-specific fashion (Song et al., 2019),
168 suggesting a differential capacity of these cells to preferentially commit into certain cell fates due
169 to metabolic dysregulation.

170

171 **Two-dimensional neural differentiation is not significantly altered by Leigh syndrome-**
172 **associated mutations.**

173 To determine if the LS mutations impact the commitment and development of the neural
174 lineage, neural progenitor cells (NPCs) were generated by a dual SMAD inhibition protocol
175 (Chambers et al., 2009) (Supplemental Figure 3A). NPCs expressed expected neural markers
176 PAX6, NESTIN, and SOX2 (Figure 3A and Supplemental Figure 3B), with no significant
177 differences between the LS cell lines and control (Figure 3B and Supplemental Figure 3B). The
178 multipotent capacity of NPCs to generate neurons, astrocytes, and oligodendrocytes was
179 evaluated using immunostaining and quantification of mRNA levels by RT-qPCR as previously
180 reported (Chambers et al., 2009; TCW et al., 2017; Vescovi and Snyder, 1999). We identified a
181 significant increase in the mean fluorescence intensity of the astrocyte marker S100β in the DLD
182 mutant line ($p=0.0185$). These results suggest an increased capacity of these cells to commit to
183 the astrocyte lineage. No other differences were observed at protein or mRNA level in the
184 neuronal or oligodendrocyte progenitor lineage. (Figure 3A-C). Thus, LS NPCs are multipotent,
185 capable of differentiation into the main cellular populations of the nervous system.

186 Neural cell death is a hallmark of LS; thus, we performed a cell viability assay to investigate
187 the sensitivity of the LS-derived NPCs to different apoptotic stimuli (Supplemental Figure 3C).
188 Treatment with DNA damaging agents, etoposide and neocarzinostatin, as well as the
189 microtubule depolymerizing agent nocodazole, did not show increased sensitivity to cell death in
190 LS NPCs compared to control. To evaluate the susceptibility of the NPCs to mitochondrial
191 damage, we treated these cells with the mitochondrial oxidative phosphorylation uncoupler,
192 CCCP. No difference was observed in the viability of the LS NPCs compared to control-treated
193 with this mitochondrial toxicant.

194

195 **LS mutations cause morphological alterations in three-dimensional models of**
196 **neurodevelopment.**

197 Previous studies using cells from LS patients carrying homozygous *SURF1* (c.769G>A and
198 c.530T>G) and MT-ATP6 (m.9185T>C) mutations showed an abnormal generation of neural
199 lineages (Lorenz et al., 2017) and impaired neurogenesis in cerebral organoids (Inak et al., 2019).
200 Therefore, we investigated the effects of the PDH, DLD, and MT-ATP6/PDH LS mutations on
201 neurogenesis using three-dimensional models of neural development as described previously
202 (Lancaster and Knoblich, 2014; Romero-Morales et al., 2019). Most of these three-dimensional
203 neural systems start with the formation of neuralized embryoid bodies (EBs). EBs are generated
204 from a single cell suspension (Itskovitz-Eldor et al., 2000) plated in ultra-low attachment
205 microwells with neural induction media (Figure 4A). EB diameter was measured on day 5 before
206 plating on Matrigel-coated imaging plates. All three LS mutant lines showed increased diameter
207 compared to control (Figure 4B, PDH vs control & DLD vs control: $p<0.0001$, MT-ATP6/PDH vs
208 control: $p=0.0209$).

209 To investigate the effects of LS-associated mutations in the early stages of CNS
210 development, we generated neural rosettes using EBs grown in the presence of SMAD inhibitor
211 media (Figure 4A) (Elkabetz et al., 2008; Zhang et al., 2001). These structures have previously
212 been established to recapitulate the early neural tube formation stage of development (Elkabetz
213 et al., 2008; Wilson and Stice, 2006). Neural rosettes were stained with the tight junction marker
214 ZO-1 (Elkabetz et al., 2008; Hříbková et al., 2018) and the centrosomal marker CDK5RAP2
215 (Figure 4C). Quantification of the number of neural rosettes per field of view showed a reduction
216 in these structures in the DLD mutant compared to controls (Figure 4D, $p<0.001$). Consistent with
217 the overall increase in EB diameter (Figure 4B), lumen area quantification showed an increase in
218 the PDH and MT-ATP6/PDH mutants, while the DLD mutant line showed a decrease in their area
219 relative to controls (Figure 4E PDH: $p<0.0001$, DLD: $p=0.0236$ and MT-ATP6/PDH: $p<0.0001$).
220 The neural rosettes obtained from all cell lines followed the expected morphological changes

221 described previously (Hříbková et al., 2018). The polymerization of α-tubulin and the generation
222 of the ZO-1 ring at the apical region of the rosettes are conserved in the LS mutants. Increased
223 neural rosette lumen size has previously been associated with activation of the TGFβ pathway
224 (Medelnik et al., 2018), Notch and sonic hedgehog (SHH) pathway, and inhibition of WNT i
225 (Elkabetz et al., 2008). Large rosette formation is thought to be a consequence of coalescence or
226 fusion of smaller rosettes (Fedorova et al., 2019) or apical domain opening and expansion rather
227 than a process dependent on cell proliferation (Medelnik et al., 2018).
228
229 **Leigh syndrome-associated mutations disrupt corticogenesis in cerebral organoids.**
230 To investigate the effects of these mutations during corticogenesis, we generated cerebral
231 organoids from LS iPSCs (Supplemental Figure 4A). Differences between the cell lines became
232 apparent as early as the neuroepithelial bud expansion phase. After Matrigel embedding, the MT-
233 ATP6/PDH mutant cell line showed poor budding with large areas of non-neuroepithelial cells
234 (Supplemental Figure 4B). Defective organoid formation in this cell line was significantly higher
235 than control and the other two LS cell lines (Supplemental Figure 4C). A previous report showed
236 that when iPSCs generated from fibroblasts harboring the same T8993G mitochondrial mutation
237 were differentiated into EBs, there was rapid regression and death after 7 days in suspension,
238 while the monolayer culture did not show obvious deficits in cell growth (Grace et al., 2019). Given
239 that the neuroectoderm expansion phase happens during days 7-10, the degeneration of the MT-
240 ATP6/PDH organoids after embedding may be consistent with these reports. Higher metabolic
241 requirements are associated with NPC proliferation and migration in three-dimensional scaffolds
242 and development (Fang et al., 2020; Homem et al., 2015). As the PDH mutant line did not show
243 this particular phenotype during the expansion of the neural epithelium, the presence of the
244 additional mitochondrial mutation in the MT-ATP6/PDH line resulted in the reduction of organoid
245 formation efficiency.

246 Cerebral organoid growth was tracked for 100 days (Supplemental Figure 4D). Growth
247 differences in the average diameter of the organoids became significant at day 80 between the
248 control and the PDH mutant line ($p< 0.05$). At days 90 and 100, organoids derived from all LS cell
249 lines were significantly smaller than the controls ($p< 0.05$). Phenotypic information available about
250 the patient from which the PDH mutant cell line was derived indicates that this particular patient
251 presented with microcephaly. Hence, we were able to mimic an aspect of the patient phenotype
252 *in vitro* using the cerebral organoid model system.

253 To assess the effect of the LS mutations on development during the first stages of neural
254 development, we collect mRNA of day 30 organoids to evaluate the pattern of expression of the
255 different NPC and cortical markers by RT-qPCR (Supplemental Figure 5A). NPC marker *SOX2*
256 expression was reduced in all three LS mutants (PDH: $p=0.0156$, DLD $p=0.0303$, MT-ATP6/DPH:
257 $p<0.0001$). Progenitor markers *NESTIN* and *PAX6* expression were also increased in PDH
258 mutant organoids ($p=0.0156$ and $p=0.0134$, respectively). In the case of MT-ATP6/PDH
259 organoids, there was a significant reduction in the expression of *PAX6* ($p=0.0231$) and a
260 significant increase in the expression of the intermediate progenitor cell (IPC) marker *TBR2*
261 ($p=0.0224$). The cortical plate marker *CTIP2* was found to be reduced in both DLD ($p=0.0080$)
262 and MT-ATP6/PDH ($p<0.0001$); and the neuronal marker βIII-TUBULIN (*TUBB3*) was reduced in
263 MT-ATP6/PDH ($p=0.0302$). No significant differences were noted in the expression of the
264 glycoprotein *REELIN* or the cortical plate marker *TBR1* among the different genotypes.

265 The reduction in the expression of the neural progenitor markers *SOX2* and *PAX6* in the MT-
266 ATP6/PDH concomitantly with the increase in *TBR2* may suggest a premature commitment into
267 intermediate progenitor cells (IPCs) (Englund, 2005; Hutton and Pevny, 2011; Sansom et al.,
268 2009). This premature differentiation into IPCs and the reduced expression of committed neuronal
269 markers such as *CTIP2* and *TUBB3* may suggest an inability to acquire a neuronal fate in this
270 particular genotype.

271 To assess if the differences observed at an mRNA level were maintained at the protein level,
272 as well as to analyze the overall cytoarchitecture of the organoids at day 30 timepoint, brain
273 organoids were sectioned and stained for the ventricular zone (VZ), subventricular zone (sVZ),
274 and cortical plate (CP) markers (Supplemental Figure 5 B-E). Day 30 organoids were obtained
275 from at least 3 independent batches of differentiation and representative images were obtained
276 from at least 4 individual organoids per batch. Quantification of the immunofluorescence images
277 revealed no significant differences among the number of NPC cells positive for the markers SOX2,
278 PAX6, and NESTIN or IPC marker TBR2 (Supplemental Figure 5F). In agreement with the
279 defective neuroepithelial expansion, the overall architecture in MT-ATP6/PDH organoids was
280 compromised. Few ventricle-like structures were present, and the foci of PAX6+ cells were not
281 organized in the expected radial pattern. Migration of early-born neurons *in vivo* depends on
282 pioneer Cajal-Retzius neurons that are positive for the glycoprotein REELIN (Lancaster et al.,
283 2017). Cells positive for this marker were identified in superficial regions of all organoids. Early-
284 born neurons at this time point are expected to migrate into the CP that will later give rise to the
285 deep cortical layers (Camp et al., 2015). CTIP2+ and TBR1+ cells were observed in all genotypes.
286 The neuronal marker Microtubule-associated protein 2 (MAP2) was also present in all samples at
287 similar levels to control (Supplemental Figure 5E and 5F). The outer radial glia marker
288 Homeodomain-only protein (HOPX) expression was significantly reduced in the PDH ($p<0.0001$)
289 and MT-ATP6/PDH mutant ($p=0.0417$). Metabolic stress has been correlated with reduced
290 specification in organoids, especially in oRG and newborn neurons (Bhaduri et al., 2020). Hence,
291 lower levels of HOPX positive cells in the cell lines harboring a PDH mutation may be associated
292 with defects in cellular fate specification at this timepoint.

293 To assess the proper cortical layer fate specification during development, we grew cerebral
294 organoids until day 100 and probed for upper cortical layer markers (Figure 7) (Florio and Huttner,
295 2014; Lui et al., 2011; Saito et al., 2011). RT-qPCR analysis of the gene expression at this time
296 point showed no significant differences in the expression of NPC markers *SOX2*, and *PAX6*; outer

297 Radial Glia (oRG) marker *HOPX* and IPC marker *TBR2*. Major dysregulation was observed in the
298 neuronal markers (Figure 5A). Cortical layer maker *CTIP2* ($p<0.0001$ in all cases), *TBR1*
299 ($p=0.0002$ for PDH and DLD, $p<0.0001$ for MT-ATP6/PDH), *SATB2* ($p<0.0001$ in all cases) and
300 *BRN2* ($p=0.0005$ for PDH, $p=0.0001$ for DLD and $p=0.0002$ for MT-ATP6/PDH) were significantly
301 reduced in all LS genotypes at this timepoint. Pan-neuronal marker *TUBB3* ($p=0.0013$ for PDH,
302 $p=0.0002$ for DLD, and $p=0.0003$ for MT-ATP6/PDH) was also reduced for all three mutants,
303 suggesting a reduced capacity of commitment to a neuronal fate. Interestingly, the neuronal
304 marker *CUX1* did not show significant differences in expression among cell types. While CUX1 is
305 predominantly expressed in pyramidal neurons of the upper layers II-IV of the developing cortex
306 (Leone et al., 2008; Nieto et al., 2004), its expression has been reported in the subventricular
307 zone (Nieto et al., 2004) and cortical plate (Saito et al., 2011). It has also been reported as being
308 co-expressed with PAX6+ and TBR2+ cells (Cipriani et al., 2015). Due to the reduced expression
309 of the cortical and neuronal markers, the maintained expression of *CUX1* could reflect its
310 conserved expression in NPC and IPC populations rather than in committed upper-layer neurons.
311 Quantification of the immunofluorescence images (Figure 5B-F) showed that the late-born
312 superficial layer marker SATB2 (layer IV) was reduced in PDH ($p=0.0305$) and DLD ($p=0.0013$)
313 organoids (Figure 5B and 5F). Cortical layer III marker BRN2 was reduced in the DLD mutant
314 ($p=0.0455$, Figure 5C and 5F). CTIP2+ cells were also reduced in DLD and MT-ATP6/PDH
315 organoids ($p<0.0001$ in both cases. Figure 5B-C and 5F). On day 100, MT-ATP6/PDH organoids
316 had a significant increase in PAX6+ cells ($p<0.0001$) compared to control (Figure 5B, 5C, and
317 5F). The reduction in the number and variety of cell types found in the LS organoids may explain
318 the decrease in their diameter at day 100 (Supplemental Figure 4D).
319 As astrogliosis is a hallmark for LS (Lake et al., 2015), we looked at the expression of
320 astrocyte markers at the mRNA and protein level. q-RT PCR analysis of neuronal marker *TUBB3*
321 reveals a marked downregulation in all three lines (PDH $p=0.0013$, DLD $p=0.0002$, and MT-
322 ATP6/PDH $p=0.0003$) that may be associated with the reduction in the number of cortical neurons.

323 Astrocyte marker *SOX9* (Sun et al., 2017) did not show major differences in expression when
324 compared to control. Analysis of other astrocyte markers such as Glial Fibrillary Acidic Protein
325 *(GFAP*), S100 calcium-binding protein-β *(S100B*), Aldehyde Dehydrogenase Family 1 Member
326 L1 (*ALDH1L1*), and *VIMENTIN* showed an increased, yet not significant, upregulation in some
327 genotypes (Figure 6A). In the case of DLD, all the above-mentioned markers were increased
328 compared to the control. The double mutant MT-ATP6/PDH had increased expression of
329 *VIMENTIN* and *ALDH1L1*, while PDH showed an increment in *S100B* and *VIMENTIN*. At a protein
330 level, DLD and PDH cerebral organoids showed increased staining of astrocyte markers GFAP
331 and S100B, respectively, at day 100 (Figure 5C, 6B, and 6D). S100B was also increased in the
332 double mutant, but not in a statistically significant manner. Staining for the pan-astrocyte marker
333 Aldehyde Dehydrogenase-1 Family Member L1 (ALDH1L1) did not show major differences
334 between the genotypes (Figure 6C and 6D). Immunofluorescence staining of the organoids for
335 β3-TUBULIN showed a statistical difference between control and DLD (p=0.0174), but not in the
336 other two mutants. The decrease in the diversity of neuronal cell types and the increase in the
337 presence of S100β+ cells in the double mutants may suggest a switch to astrocyte fate during
338 cortical development. Interestingly, the DLD organoids had higher GFAP staining when compared
339 to control (p=0.0141) that may suggest an increase in the reactivity of the astrocyte population.
340 Upregulation of the astrocyte markers GFAP, S100β*,* and VIMENTIN have been associated with
341 astrocyte reactivity and in response to injury (Clarke et al., 2018; Escartin et al., 2021; Liddelow
342 and Barres, 2017; Liddelow et al., 2017; Qi et al., 2017; Zamanian et al., 2012). Although the
343 gene expression of these pan-reactive markers was not significant when compared to control, it
344 may suggest activation of the glial population in response to the metabolic dysregulation in LS
345 organoids.
346

347 **Leigh syndrome-associated mutations disrupt the mitochondrial network in the ventricular**
348 **zone of cerebral organoids.**

349 Mitochondria in murine NPCs form an elongated network (Khacho et al., 2016) which
350 fragments as cells undergo neurogenesis (Iwata et al., 2020). Mitochondrial morphology was also
351 evaluated in the VZ NPCs of the cerebral organoids. Cells positive for NPC marker SOX2+
352 demonstrated elongated mitochondrial networks that extend radially from the ventricle-like lumen
353 (Supplemental Figure 6A). These results are significant because it is the first evidence
354 demonstrating that the mitochondrial networks are remodeled in the developing human brain as
355 reported in the developing mouse cortex (Iwata et al., 2020; Khacho et al., 2016). PDH mutant
356 organoid NPCs have an increased axis length of their mitochondrial network in comparison with
357 control ($p=0.0078$, Supplemental Figure 6B). As mentioned earlier, the stereotypical arrangement
358 of the VZ was compromised in most MT-ATP6/PDH organoids. In the few areas where ventricle-
359 like structures were identified with a conserved SOX2+ VZ, the mitochondrial network appeared
360 more aggregated. This morphology was also observed in the clusters of SOX2+ cells that were
361 scattered throughout the organoid. Quantification of the mitochondrial network for this mutant
362 (Supplemental Figure 6B) showed differences in the mitochondrial network's volume, diameter,
363 surface area, and axis length ($p<0.0001$, in all cases). A higher volume and diameter may suggest
364 an increase in mitochondrial aggregation in the VZ. Moreover, the difference in mitochondrial
365 length may also correlate with the increased expression of *TBR2* observed by RT-qPCR (Iwata
366 et al., 2020).

367 As NPCs generated by a dual SMAD monolayer method did not show major differences
368 among the different genotypes, we looked at their mitochondria morphology to evaluate if the
369 differences observed in the organoids were recapitulated in this setup. Characterization and
370 quantification of various parameters of the mitochondrial network using structured illumination
371 microscopy (SIM) showed that while control human NPCs showed elongation of the mitochondrial
372 network, the DLD mutant shows an increase in mitochondrial number and decreased sphericity.

373 Both DLD and PDH mutants have a significant increase in the number of branches in the network.
374 (Supplemental Figure 6C-6D) which may reflect an increase in fusion events (Sukhorukov et al.,
375 2012; Westrate et al., 2014). These parameters suggest that both the DLD and PDH mutant lines
376 present alterations in mitochondrial morphology, which could be linked to the underlying changes
377 in metabolic capacity (Rafelski, 2013) and developmental defects (Westrate et al., 2014).
378

379 **Metabolic dysregulation in Leigh syndrome-derived cerebral organoids**

380 To explore early changes in metabolites, we perform metabolomic profiling of Day 40
381 organoids from control and LS samples. Metabolomic analysis showed 43 different metabolites
382 that were statistically dysregulated in the LS organoids when compared to control (Supplemental
383 Table 2 and Supplemental Figure 7). Out of these metabolites, 8 were dysregulated in PDH, 16
384 in DLD, and 32 in MT-ATP6/PDH (Figure 7A and Supplemental Figure 7).

385 The metabolites proline, 6-phosphogluconic acid, and hydroxyphenyllactic acid were
386 dysregulated in all three LS mutants. Proline concentration was elevated when compared to
387 control. High levels of proline have been associated with negative effects in brain function by
388 interference in glutamatergic neurotransmission (Gogos et al., 1999; Vorstman et al., 2009). On
389 the other hand, 6-phosphogluconic acid was reduced in all three LS cell lines. High concentrations
390 of this metabolite have been associated with an active pentose phosphate pathway in early brain
391 development in rats (Hakim et al., 1980) and its supplementation increased the diameter of
392 neurospheres derived from the embryonic Ts1Cje mouse model of Down syndrome (Seth et al.,
393 2020). In addition, hydroxyphenyllactic acid was elevated in DLD and PDH mutant organoids but
394 downregulated in MT-ATP6/PDH. High levels of this metabolite have been reported in association
395 with high lactate and pyruvate in pediatric lactic acidosis in patients with PDHc deficiency (Kumps
396 et al., 2002; Stern, 1994).

397 Pyruvate was also increased in the MT-ATP6/PDH mutant organoids, correlating with the
398 lactic acidosis expected in the organoids based on the patient phenotypes and the presence of

399 the PDH mutation that hinders flux from pyruvate into the TCA cycle through acetyl-CoA.
400 Moreover, the glycolysis/gluconeogenesis intermediate phosphoenolpyruvate was also elevated
401 in these mutants. Increased levels of phosphoenolpyruvate in rat brains after ischemic injury are
402 thought to have a protective role in cerebral ischemia *in vivo* (Geng et al., 2021) and in
403 oxygen/glucose deprivation *in vitro* (Jiang et al., 2019).

404 Besides the previously mentioned metabolites, MT-ATP6/PDH mutant organoids presented
405 increased levels of choline, cytidine, and leucine. Choline is a crucial metabolite for normal CNS
406 development. Neural tube defects have been associated with a lack of choline during early
407 pregnancy (Zeisel, 2006). It has also been shown to increase cell proliferation and decrease
408 apoptosis in fetal rat hippocampal progenitor cells (Albright et al., 1999b, 1999a; Zeisel and
409 Niculescu, 2006). Choline is also crucial for the production of the neurotransmitter acetylcholine,
410 the sphingolipid sphingomyelin, and myelin (Oshida et al., 2003). Concomitantly, cytidine is used
411 with choline for the generation of cytidine-5-diphosphocholine, a crucial intermediate in the
412 biosynthesis of the cell membrane phospholipids phosphatidylcholine and
413 phosphatidylethanolamine (Cansev, 2006; Rema et al., 2008). Increased abundance of the
414 branched-chain amino acid leucine has been associated with the metabolic illness maple syrup
415 urine disease and can be extremely neurotoxic (Bridi et al., 2005; García-Cazorla et al., 2014).
416 This amino acid is considered ketogenic as its end products can enter the TCA cycle for energy
417 generation or act as precursors for lipogenesis and ketone body production (Manoli and Venditti,
418 2016).

419 Pathway analysis of the dysregulated metabolites (Supplemental Tables 3, 4, and 5) show
420 overlap in the pyrimidine metabolism, taurine, and hypotaurine metabolism, pentose phosphate
421 pathway, arginine and proline metabolism, and aminoacyl-tRNA biosynthesis. Pyrimidine
422 nucleotides are essential precursors for nucleic acid synthesis and are involved in polysaccharide
423 and phospholipid biosynthesis, detoxification processes, and protein and lipid glycosylation
424 (Fumagalli et al., 2017). Taurine and hypotaurine are osmotic regulators in the brain, as well as

425 agonists to GABAergic and glycinergic neurons (Albrecht and Schousboe, 2005). Its presence in
426 the developing brain is necessary for the correct development of axons and the formation of
427 synaptic connections (Sturman, 1993). Dysregulation of the aminoacyl-tRNA biosynthesis
428 pathways is well documented as causal etiology for several neurodevelopmental disorders such
429 as leukoencephalopathies, microcephaly, and Leigh syndrome (Francklyn and Mullen, 2019;
430 Ognjenović and Simonović, 2018).

431 We also performed metabolite set enrichment analysis (Figure 7B-C). Besides the previously
432 mentioned pathways, the Warburg effect or aerobic glycolysis was also shared among the LS
433 mutants. Although this effect is considered one of the hallmarks of cancer, it has also been
434 associated with several homeostatic processes, including cell turnover and proliferation, and brain
435 development (Bubici and Papa, 2019). Energy generation through aerobic glycolysis as a
436 compensatory mechanism to overcome the metabolic deficiency in LS could suggest a survival
437 adaptation of the cerebral organoids. Moreover, the shutoff of aerobic glycolysis is critical to
438 neuronal differentiation in human NPCs. Inability to transition to neuronal oxidative
439 phosphorylation causes apoptosis due to excessive conversion of pyruvate to lactate, and
440 potentially a cell fate shift into GFAP-positive glial cells (Zheng et al., 2016b). Considering our
441 observations that there is a marked deficit in MT-ATP6/PDH mutants to commit and generate
442 neuronal subtypes and an increased signal in astroglial markers, these mutations may be
443 impairing the ability to transition from aerobic glycolysis to OXPHOS as previously described with
444 SURF mutations (Inak et al., 2019, 2021). The preferential switch to a glial fate may be promoted
445 by astrocytes having low expression levels or lower active levels of the PDHα subunit (Bélanger
446 et al., 2011; Halim et al., 2010; Itoh et al., 2003; Laughton et al., 2007).

447 Considering all the previous findings, the cerebral organoid system emerges as a promising
448 model for the study of the effects of LS-associated mutations in brain development and the effects
449 of metabolic impairment during corticogenesis.

450

451 **Discussion**

452 Inborn errors of metabolism are rare genetic disorders resulting from defects in metabolic
453 pathways (Agana et al., 2018; Das et al., 2010). Mitochondrial diseases are the most common
454 group of inherited metabolic disorders and are among the most common forms of inherited
455 neurological disorders (Gorman et al., 2016). These illnesses are challenging not only at the time
456 of diagnosis but also during their medical evolution, as they involve multiple organ systems and
457 have limited therapeutic options (Grier et al., 2018; Parikh et al., 2017; Schaefer et al., 2019).

458 Leigh syndrome is one of these rare inherited neurometabolic diseases, with more than 75
459 causal genes identified in both nuclear and mitochondrial DNA. It has an early onset, affecting
460 most patients within their first year of life, although cases during teenage years and adulthood
461 have been reported (Finsterer, 2008; Lake et al., 2016). As it is a highly heterogeneous disease,
462 the establishment of animal and *in vitro* models has been challenging and limited to only select
463 mutations. The few animal models available have been utilized for the development of therapeutic
464 approaches with mixed results. Gene editing using adeno-associated virus in *Ndufs4*-/- mice has
465 shown partial rescue of the phenotype (Di Meo et al., 2017). Supplementation of nicotinamide
466 riboside to *Sco2*-/- mice showed improvement of the respiratory chain defect and increased
467 exercise tolerance due to improved mitochondrial biogenesis (Cerutti et al., 2014). Hypoxia and
468 low oxygen availability in the brain have also been shown to increase the life span and improve
469 neurological findings in *Ndufs4*-/- mice (Ferrari et al., 2017; Jain et al., 2016, 2019).

470 Molecular testing and prenatal diagnosis of respiratory chain disorders using skin fibroblasts
471 and muscle biopsies for diagnostic and research purposes are becoming mainstream procedures
472 (Baertling et al., 2014; Calvo et al., 2006, 2012; Schubert and Vilarinho, 2020). Nevertheless,
473 heteroplasmy in mitochondrial DNA among tissues can cause less pronounced or absent
474 phenotypes in cultured cells (Baertling et al., 2014). Here we report the characterization and the
475 subsequent generation of brain organoids from three commercially available Leigh syndrome
476 fibroblast cell lines and age-matched control.

477 Three-dimensional differentiation generates higher numbers of NPCs and more mature
478 neurons than two-dimensional differentiation (Chandrasekaran et al., 2017; Di Lullo and
479 Kriegstein, 2017; Muratore et al., 2014; Paşca et al., 2015) in part due to an improved spatial
480 cellular environment that influences cell fate specification. Tissue architecture, mechanical cues,
481 cell-to-cell communication (Pampaloni et al., 2007), nutrient accessibility, oxygen tension, as well
482 as morphogen gradients characteristic of 3D systems (Tibbitt and Anseth, 2012) aid to
483 recapitulate the development of the central nervous system (CNS) up to approximately 16 weeks
484 post-fertilization (Camp et al., 2015; Paşca et al., 2015). We observed that all the LS cerebral
485 organoids failed to thrive at different time points. Although organoid development initially
486 appeared normal in cell lines with nuclear-encoded LS mutations, at later time points the overall
487 diameter decreased, presumably due to failure to generate upper-layer neurons. This reduction
488 of late-born neurons may be due to the overall reduction in the PAX6+ NPCs in both PDH and
489 DLD compared to controls. Interestingly, PDH cerebral organoids displayed arrested growth very
490 early on, correlating with the microcephaly observed in the proband.

491 Clinical data from LS patients include marked gliosis as part of the characteristic findings
492 (Baertling et al., 2014, 2016; Lake et al., 2015; Schubert and Vilarinho, 2020). While this marked
493 gliosis is potentially associated with a reactive process secondary to neuronal damage, an
494 intriguing alternate possibility is that progenitor cells may have an increased propensity to
495 differentiate down the astrocyte lineage due to LS-causative mutations and mitochondrial-
496 associated dysregulations. Previous studies have shown that reactive astrocytes acquire
497 molecular hallmarks of radial glial cells. It was also shown through genetic fate mapping that
498 mature astroglial cells can dedifferentiate and resume proliferation (Robel et al., 2009, 2011).
499 Thus, the increase in the glial-specific marker S100β in PDH organoids and DLD multipotency
500 cultures, as well as in GFAP staining in DLD organoids and the upregulation trend in the mRNA
501 expression of the astrocyte markers could either reflect that chronic metabolic stress induced by
502 Leigh syndrome mutations activates a brain injury response, or that the inhibition of mitochondrial

503 metabolism in neural progenitor cells could cause defects in lineage selection (Escartin et al.,
504 2021). Due to the differential expression and activation levels of the PDH complex in astrocytes
505 (Bélanger et al., 2011; Halim et al., 2010), a predisposition of these cell lines to commit to an
506 astroglial fate cannot be ruled out. Also, longer culture (>100days) of these organoids may allow
507 for the interrogation of a gliosis phenotype in more detail. Analysis of A1 specific reactivity markers
508 may point out if the upregulation of *GFAP, S100B, ALDH1L1,* and *VIMENTIN* is associated with
509 a neuroinflammation type of response that has been associated with neuronal damage (Escartin
510 et al., 2021; Liddelow et al., 2017).

511 The formation of lesions in LS has been described as the result of OXPHOS dysfunction and
512 subsequent ATP depletion. Neuronal dysfunction is suspected to trigger chronic gliosis (Baertling
513 et al., 2016). In patients, the gliosis phenotype can be accompanied by vascular hypertrophy and
514 the production of excess ROS, which increases neuronal damage (Lake et al., 2015). However,
515 due to the lack of vascularization in the organoid model, replicating the vascular abnormalities
516 associated with LS is not feasible in this system.

517 In a previous study (Hattori et al., 2016), the metabolic signature analysis of iPSCs derived
518 from a mitochondrial encoded LS mutation (m.10191T>C) showed differences in the abundance
519 of pyruvate and lactate, among others. Interestingly, the metabolic difference between control and
520 LS cells was reported to revert to normal after EB differentiation (Hattori et al., 2016). In our study,
521 metabolomic analysis from organoids shows that the observed changes in the metabolites are in
522 line with the clinical observations of LS patients. Changes in blood and cerebral spinal fluid
523 concentration of lactate and pyruvate are common diagnostic tools for LS (Hattori et al., 2016)
524 and other mitochondrial diseases (Barshop, 2004; Buzkova et al., 2018; Esterhuizen et al., 2017;
525 Rahman and Rahman, 2018). While changes in the NADH/NAD+ ratio, *de novo* nucleotide
526 synthesis, and in other metabolites from the ETC complex III and TCA cycle, were also identified,
527 these were modest considering the genetic alterations in the mutant cell lines should directly affect
528 these pathways. This could point out to metabolic compensatory mechanisms that may be

529 engaged during development. Moreover, the disruption in the metabolic network observed in the
530 LS cerebral organoids correlates with the severity and mortality of the disease in the probands.
531 Although aerobic glycolysis was identified as a significantly affected pathway in all the mutants,
532 the effects of the MT-ATP6/PDH mutation reflected the importance of competent glycolysis to
533 OXPHOS transition in the early brain development (Zheng et al., 2016b).

534 The metabolic dysregulation of the affected tissues in LS may have a direct effect on
535 mitochondrial morphology and function. Mitochondrial fragmentation is a hallmark of glycolytic
536 cell types such as stem cells and cancer cells (Chen and Chan, 2017; Rastogi et al., 2019).
537 Moreover, neurogenesis defects have been observed in the context of mitochondrial morphology
538 dysregulation and are considered to be upstream regulators of self-renewal and cell fate decisions
539 in stem cells (Iwata et al., 2020; Khacho et al., 2016). In addition, energetic requirements have
540 been shown to directly impact the capacity of progenitor cells to migrate and thrive in 3D
541 environments (Zanotelli et al., 2018, 2019). Hence, mitochondrial morphology disruption observed
542 in the double mutant MT-ATP6/PDH organoids is congruent with the metabolic and
543 developmental profiles of these mutant organoids. To our knowledge, this is the first time that
544 mitochondrial morphology in the cortex has been analyzed in a human model system of LS brain
545 development and highlights the critical function of mitochondrial network plasticity for the proper
546 specification of cell fate and survival. Studies in murine brains demonstrated a period of plasticity
547 in postmitotic cells where mitochondrial morphology determines the fate of the daughter cells
548 (Iwata et al., 2020). Our results also highlight the direct link of mitochondrial morphology with early
549 events in human brain development.

550 The profound dysregulation of corticogenesis in the double mutant MT-ATP6/PDH may
551 suggest that some pregnancies harboring LS-causing mutations may not be viable, which could
552 lead to an underestimation of the prevalence of the disease in the population (Feeney et al.,
553 2019). Prenatal genetic evaluation is now being performed for cases where there is a known risk
554 for mitochondrial mutations (Craven et al., 2017; White et al., 1999). This testing can be performed

555 as early as 10-12 weeks post conception and is usually requested if there is a history of a
556 previously affected child or first-degree relative (Nesbitt et al., 2014). Interpretation of these tests
557 is challenging in the case of mitochondrial mutations due to heteroplasmy; the biopsied tissues
558 may exhibit a different mutational burden compared with other fetal tissues (Ferlin et al., 1997;
559 Harding et al., 1992; Nesbitt et al., 2014; Steffann et al., 2007).

560 Taken together, our study sheds new light on the morphological and functional LS alterations
561 impacting early events of neurogenesis. We were able to identify new genetic alterations in LS
562 samples by using whole-exome sequencing and mitochondrial DNA sequencing. We described
563 the effects of LS mutations on early development, underscoring the critical function of metabolism
564 in human neurogesis. Our works also provides a comprehensive phenotypic characterization of
565 available patient samples to encourage their utilization as model systems for uncovering the
566 mechanisms underlying neuronal cell death in the context of LS and as human platforms for drug
567 discovery.
568

569 **Figure Legends**

570 **Figure 1.** Whole exome sequencing identifies novel mutations in Leigh syndrome fibroblasts. A.
571 Schematic of the WES and mitochondrial sequencing workflow. B. Representation of whole-
572 genome sequencing data, highlighting the top 20 genes containing high impact indels. C.
573 Representation of whole-genome sequencing data, highlighting the top 20 genes containing high
574 impact SNPs (increased likelihood of disrupting protein function). D. Mitochondrial sequencing
575 identifies novel mutations in LS fibroblasts. Representation of mitochondrial sequencing data,
576 highlighting mitochondrial genes containing mutations (transitions, deletions, or transversions).
577 Red dots: represent the DLD line. Green dots: represent the PDH line. Orange dots: represent
578 the MT-ATP6/PDH line. E. Representation of the affected proteins in the LS mutant cell lines.
579 PDH and DLD are part of the pyruvate dehydrogenase complex (PDHc). MT-ATP6 is a subunit
580 of the ATP synthase, represented here as the electro transport chain complex V. PDH: Pyruvate
581 dehydrogenase. DLD: Dihydrolipoyl dehydrogenase. MT-ATP6/PDH: Mitochondrially Encoded
582 ATP Synthase Membrane Subunit 6/ Pyruvate dehydrogenase.

583

584 **Figure 2.** Induced pluripotent stem cells derived from Leigh syndrome patient fibroblasts are
585 capable of differentiation into specific lineages. A. Representative images of the three embryonic
586 lineages markers. Ectoderm marker Pax6, endoderm marker SOX17, and mesoderm markers
587 Brachyury and CXCR4. Scale bar: 100µm. B. Immunofluorescence quantification for the
588 aforementioned markers. Three independent differentiations were performed. Positive nuclei for
589 the analyzed markers were divided by the total number of nuclei stained with DAPI. C. RT-qPCR
590 analysis for the ectodermal genes *GATA3* and *PAX6*, ectodermal genes *CDX2* and *SOX17* the
591 mesodermal genes *TBXT* and *NCAM*. Fold change normalized to GPI and GAPDH as
592 housekeeping genes. Graphs represent mean ± SEM from at least three independent
593 experiments.

594

595 **Figure 3.** Leigh syndrome-derived NPCs are multipotent and do not show aberrant mitochondrial
596 morphology compared to control. A. Representative images of the expression of neural
597 multipotency markers. Neural progenitor cells stained by PAX6 and NESTIN, neurons marked
598 with βIII-TUBULIN (TUBB3), oligodendrocyte progenitor cells (OPCs) were stained with Olig2,
599 and astrocytes are marked with S100β. Merged panels show the color image of the grayscale
600 lineage marker and the nuclear staining DAPI in blue. Scale bar: 100μm. B. Immunofluorescence
601 quantification for the aforementioned markers. Three independent differentiations were
602 performed. Mean fluorescence intensity for each marker was normalized to the nuclear DAPI
603 intensity and the intensity values of control. C. RT-qPCR Analysis of the NPC markers *PAX6* and
604 *NESTIN*, as well as the multipotency markers *MAP2* and *TUBB3* for neuronal lineage, *S100B* and
605 *GFAP* for astrocytic lineage, and *OLIG2* and *FOXO4* for OPCs. Fold change normalized to GPI
606 and GAPDH as house-keeping genes.
607
608 **Figure 4.** Three-dimensional differentiation reveals abnormalities during induction of neural
609 rosettes in LS cell lines. A. Schematic of neural rosette generation protocol. B. Embryoid body
610 diameter is increased in the three LS cell lines. C-E. Representative confocal images of neural
611 rosettes (C) show decreased numbers of neural rosettes per field in the DLD mutant line (D).
612 Quantification of the lumen area (μm^2) indicates increased lumen area in the PDH and MT-
613 ATP6/PDH mutant cell lines and a decreased lumen area in the DLD mutant line (E). Scale bar:
614 50μm.
615
616 **Figure 5.** Leigh syndrome-derived brain organoids show defects in cortical layer formation at day
617 100. A. RT-qPCR quantification of the day 100 organoids. Neural progenitor cell populations were
618 evaluated by the expression of *SOX2* and *PAX6*. Intermediate progenitor cells (IPCs) were
619 identified with the marker *TBR2* and outer radial glia (oRG) was evaluated by the expression of
620 *HOPX*. Markers *CTIP2*, *TBR1*, *SATB2*, *BRN2*, and *CUX1* were assessed for cortical

621 development. B-D. Representative confocal images of day 100 brain organoids. LS-derived brain
622 organoids present reduced expression of the upper layer markers SATB2 (B) and BRN2 (C) and
623 deep layer marker CTIP2 (B & C). Expression of the astrocyte marker S100β was also observed
624 in the cell lines (C). LS-derived brain organoids express the upper layer marker CUX1 and NPC
625 marker PAX6 (D). Images were generated from at least three different organoids per genotype
626 from independent organoid batches. Scale bar for B-D: 100μm. E. Schematic representation of
627 the expected organization of the brain organoids at day 100. F. Quantification of day
628 immunofluorescence staining for day 100 brain organoids. Upper layer marker SATB2 was
629 significantly reduced in PDH mutant ($p=0.0305$). DLD mutant presented reduced expression of
630 the cortical layer markers CTIP2 ($p<0.0001$), SATB2 ($p=0.0013$), and BRN2 ($p=0.0455$). The
631 double mutant MT-ATP6/PDH shows a significant increase in the PAX6+ population ($p<0.0001$),
632 as well as reduced expression of the cortical plate marker CTIP2 ($p<0.0001$). Data are shown as
633 mean ±SEM. Comparisons were performed as ordinary one-way ANOVA with a Dunnett's multiple
634 comparisons test post-hoc. SVZ: subventricular zone, VZ: ventricular zone, DL: deep layers UL:
635 upper layers, MZ: marginal zone.
636
637 **Figure 6.** LS brain organoids show dysregulation of neuronal and glial markers at day 100. A.
638 RT-qPCR analysis of neuronal and astrocytic genes at day 100. Neuronal marker *TUBB3* and
639 astrocytic markers *SOX9*, *GFAP*, *S100B*, *VIMENTIN*, and *ALDH1L1* were evaluated. A significant
640 decrease in the expression of the neuronal marker *TUBB3* was observed in all phenotypes. Fold
641 change normalized to GPI and GAPDH as housekeeping genes. B-C. Day 100
642 immunofluorescence images of astrocytic markers GFAP (B) and ALDH1L1 (C), and neuronal
643 marker βIII TUBULIN (TUBB3). Nuclei in the merged image correspond to the blue channel. Scale
644 bar: 100μm. D. Immunofluorescence quantification of the neuronal and astrocytic staining. DLD
645 mutant presented decrease staining in the neuronal marker TUBB3 ($p=0.0174$) and an increase

646 in the astrocytic marker GFAP (p=0.0141); The PDH mutant shows a significant increase in the
647 S100β+ population (p=0.0354). Scale bar for B-C: 100μm. Data are shown as mean ±SEM.
648 Comparisons were performed as ordinary one-way ANOVA with a Dunnett's multiple comparisons
649 test post-hoc.
650
651 **Figure 7.** Day 40 LS organoids show changes in their metabolic profiles. A. 43 metabolites were
652 statistically dysregulated ($p<0.05$ and FDR of 0.01) segregated by affected cell line. A total of
653 three batches of 40-day organoids per line (4 independent organoids per line per batch) were
654 analyzed as described in methods. B. Metabolite Set Enrichment Analysis for dysregulated
655 metabolites enriched in the PDH mutant. C. Metabolite Set Enrichment Analysis for dysregulated
656 metabolites enriched in the DLD mutant. D. Metabolite Set Enrichment Analysis for dysregulated
657 metabolites enriched in the MT-ATP6/PDH mutant. Diameter of the node is determined by the
658 level of enrichment, while the color of the node represents the p-value of the interaction.
659

660 **Detailed Methods**

661 **Key Resource Table**

REAGENT or RESOURCE	SOURCE	IDENTIFIER
ANTIBODIES		
Primary Antibodies (Immunocytochemistry)		
Mouse anti-MAP2	Thermo Fisher Scientific	Cat # 131500, AB_2533001
Rabbit anti-GFAP	Agilent Technologies	Cat # Z0334, AB_10013382
Rabbit anti-HOPX	Sigma-Aldrich	Cat # HPA030180, AB_10603770
Mouse anti-mitochondria	Abcam	Cat # ab92824, AB_10562769
Rabbit anti-SOX2	Cell Signaling Technology	Cat # 5049S, AB_10828386
Rabbit anti-PAX6	Cell Signaling Technology	Cat # 60433, AB_2797599
Rabbit anti-SOX17	Cell Signaling Technology	Cat # 81778S, AB_2650582
Rabbit anti-BRACHYURY	Cell Signaling Technology	Cat # 81694S, AB_2799983
Mouse anti-CD184 (CXCR4)	STEMCELL Technologies	Cat # 60089
Mouse anti-β3 TUBULIN	Cell Signaling Technology	Cat # 4466, AB_10270973
Rabbit anti-S100	Abcam	Cat # ab868, AB_306716
Mouse anti-Olig2	Millipore Sigma	Cat # MABN50, AB_10807410
Rat anti-α TUBULIN	Thermo Fisher Scientific	Cat # MA180017, AB_2210201
Mouse anti-ZO-1	Thermo Fisher Scientific	Cat # 339100, AB_2533147
Rabbit anti-CDK5RAP2	Bethyl Laboratories	Cat # IHC00063, AB_2076863
Mouse anti-NESTIN	STEMCELL Technologies	Cat # 60091, AB_2650581
Chicken anti-TBR2	Millipore Sigma	Cat # AB15894, AB_10615604
Mouse anti-REELIN	Millipore Sigma	Cat # MAB5366, AB_2285132
Rat anti-CTIP2	Abcam	Cat # ab18465, AB_2064130
Rabbit anti-TBR1	Abcam	Cat # ab31940, AB_2200219
Rabbit anti-TOM20	Cell Signaling Technology	Cat # 42406, AB_2687663
Mouse anti-SATB2	Abcam	Cat # ab51502, AB_882455
Mouse anti-BRN2 (POU3F2)	Millipore Sigma	Cat # MABD51, AB_11204531
Mouse anti-CASP (CUX1)	Abcam	Cat # ab54583, AB_941209
Rabbit anti-ALDH1L1	Cell Signaling Technology	Cat # 85828S

Secondary Antibodies (Immunocytochemistry)		
Goat anti Chicken Alexa Fluor 647	Thermo Fisher Scientific	Cat # A-21449, AB_2535866
Goat anti Rat Alexa Fluor 647	Thermo Fisher Scientific	Cat # A-21247, AB_2535864
Donkey anti Rabbit Alexa Fluor 647	Thermo Fisher Scientific	Cat # A-31573, AB_2536183
Donkey anti Mouse Alexa Fluor 647	Thermo Fisher Scientific	Cat # A-31571, AB_162542
Donkey anti Rabbit Alexa Fluor 546	Thermo Fisher Scientific	Cat # A-10040, AB_2534016
Donkey anti Mouse Alexa Fluor 546	Thermo Fisher Scientific	Cat # A-10036, AB_2534012
Donkey anti Rabbit Alexa Fluor 488	Thermo Fisher Scientific	Cat # A-21206, AB_2535792
Donkey anti Mouse Alexa Fluor 488	Thermo Fisher Scientific	Cat # A-21202, AB_141607
Primary Antibodies (Western Blotting)		
Rabbit anti-PAX6	Cell Signaling Technology	Cat # 60433, AB_2797599
Mouse anti-NESTIN	STEMCELL Technologies	Cat # 60091, AB_2650581
Rabbit anti-Sox2	Cell Signaling Technology	Cat # 3579, AB_2195767
Mouse anti- α TUBULIN	Sigma-Aldrich	Cat # T9026, AB_477593
Secondary Antibodies -HRP conjugated (Western Blotting)		
Peroxidase AffiniPure Donkey Anti-Rabbit IgG (H+L)	Jackson ImmunoResearch Inc	Cat # 711-035-152, AB_10015282
Peroxidase AffiniPure Donkey Anti-Mouse IgG (H+L)	Jackson ImmunoResearch Inc	Cat # 715-035-151, AB_2340771
CHEMICALS, PEPTIDE, AND RECOMBINANT PROTEINS		
Y-27632 Rho/Rock pathway inhibitor	STEMCELL Technologies	Cat # 72307
Dorsomorphin	Millipore Sigma	Cat # P5499
SB431542	REPROCELL	Cat # 04-0010-10
Etoposide	Millipore Sigma	Cat # E1383
Carbonyl cyanide 3-chlorophenylhydrazone (CCCP)	Sigma Aldrich	Cat # C2759
Nocodazole	Sigma Aldrich	Cat # M1404
Neocarzinostatin	Sigma Aldrich	Cat # 9162

CRITICAL COMMERCIAL ASSAYS AND KITS		
PluriTest Assay	Thermo Fisher Scientific	Cat# A38154
KaryoStat Assay	Thermo Fisher Scientific	Cat# A38153
Mitochondrial DNA sequencing	Girihlet	
Whole Exome sequencing	Genewiz LLC	
CytoTune iPS 2.0 Sendai Reprogramming Kit	Thermo Fisher Scientific	Cat # A16517
STEMdiff Trilineage Differentiation Kit	STEMCELL Technologies	Cat# 05230
NeuroCult™ media	STEMCELL Technologies	Cat # 05752
Astrocyte medium	ScienCell	Cat # 1801
CellTiter Blue Viability Assay	Promega	Cat # G8081
DEPOSITED DATA		
Raw and analyzed sequencing data	Done by Creative Solutions (J.P.C, Vanderbilt University	https://www.ncbi.nlm.nih.gov/sra/PRJNA626388 https://vandydata.github.io/Romero-Morales-Gama-Leigh-Syndrome-WES/
EXPERIMENTAL MODELS: CELL LINES		
AG16409 control fibroblasts	Coriell Institute	https://www.coriell.org/0/Sections/Search/Sample_Detail.aspx?Ref=AG16409&Product=CC
GM13411 (MT-ATP6/PDH) fibroblasts	Coriell Institute	https://www.coriell.org/0/Sections/Search/Sample_Detail.aspx?Ref=GM13411&Product=CC
GM03672 (PDH Mutant) fibroblasts	Coriell Institute	https://www.coriell.org/0/Sections/Search/Sample_Detail.aspx?Ref=GM03672&Product=CC
GM01503 (DLD Mutant) fibroblasts	Coriell Institute	https://www.coriell.org/0/Sections/Search/Sample_Detail.aspx?Ref=GM01503&Product=CC
SEQUENCE-BASED REAGENTS		
Primers for Trilineage assay		
POU5F1	Integrated DNA Technologies	Forward GGGCTCTCCCATGCATTCAAAC Reverse CACCTTCCCTCCAACCAGTTGC
NANOG	Integrated DNA Technologies	Forward TGGGATTTACAGGCGTGAGCCAC Reverse AAGCAAAGCCTCCCAATCCCAAAC
GAPDH	Integrated DNA Technologies	Harvard Primer Bank, ID: 378404907c2 Forward ACAACTTTGGTATCGTGGAAGG Reverse GCCATCACGCCACAGTTTC
GPI	Integrated DNA Technologies	Forward GTGTACCTTCTAGTCCCGCC Reverse GGTCAAGCTGAAGTGGTTGAAGC

GATA3	Integrated DNA Technologies	Forward TGGAGGAGGAATGCCAATGGG Reverse GCCGGGTTAAACGAGCTGTTCTTG
NESTIN	Integrated DNA Technologies	Harvard Primer Bank, ID: 38176299c1 Forward CTGCTACCCTTGAGACACCTG Reverse GGGCTCTGATCTCTGCATCTAC
PAX6	Integrated DNA Technologies	Harvard Primer Bank, ID: 189083679c1 Forward TGGGCAGGTATTACGAGACTG Reverse ACTCCCGCTTATACTGGGCTA
CDX2	Integrated DNA Technologies	Forward CTGGAGCTGGAGAAGGAGTTTCAC Reverse GACACTTCTCAGAGGACCTGGCTG
SOX17	Integrated DNA Technologies	Harvard Primer Bank, ID:145275218c1 Forward GTGGACCGCACGGAATTTG Reverse GGAGATTCACACCGGAGTCA
TBXT	Integrated DNA Technologies	Forward ACAATGCCAGCCCACCTACCAG Reverse CGTACTGGCTGTCCACGATGTCTG
NCAM	Integrated DNA Technologies	Harvard Primer Bank, ID:316659209c1 Forward GGGGTTGCTTGTCAGTAGC Reverse TTCAGGTTCACCAATCGCTGT
Primers for Multipotency		
S100B	Integrated DNA Technologies	Harvard Primer Bank, ID: 114520588c1 Forward TGGCCCTCATCGACGTTTTC Reverse ATGTTCAAAGAACTCGTGGCA
GFAP	Integrated DNA Technologies	Reference: (Marton et al., 2019) Forward GGCAAAAGCACCAAAGACGG Reverse GGCGGCGTTCCATTTACAAT
O4 (FOXO4)	Integrated DNA Technologies	Harvard Primer Bank, ID: 283436081c1 Forward GGCTGCCGCGATCATAGAC Reverse GGCTGGTTAGCGATCTCTGG
OLIG2	Integrated DNA Technologies	Reference: (Marton et al., 2019) Forward AAGGCAGTTGCTGTGGAAAC Reverse GCAAACAGCTTAGCATTGCG
TUBB3	Integrated DNA Technologies	Harvard Primer Bank, ID: 308235961c1 Forward GGCCAAGGGTCACTACACG Reverse GCAGTCGCAGTTTTCACACTC
MAP2	Integrated DNA Technologies	Harvard Primer Bank, ID: 87578393c1 Forward CTCAGCACCGCTAACAGAGG Reverse CATTGGCGCTTCGGACAAG
Primers for Brain Organoids		
Reelin	Integrated DNA Technologies	Harvard Primer Bank, ID: 223718142c2 Forward ACATCTACAAGTGTTCAGGCATC Reverse TGGTTACCAAACTGGTGGTCA
HOPX	Integrated DNA Technologies	Harvard Primer Bank, ID: 21311737a1 Forward GAGACCCAGGGTAGTGATTTGA Reverse AAAAGTAATCGAAAGCCAAGCAC
CTIP2 (BCL11B)	Integrated DNA Technologies	Harvard Primer Bank, ID: 12597634c2 Forward TCCAGCTACATTTGCACAACA Reverse GCTCCAGGTAGATGCGGAAG

TBR2 (EOMES)	Integrated DNA Technologies	Harvard Primer Bank, ID: 22538469c2 Forward GTGCCCACGTCTACCTGTG Reverse CCTGCCCTGTTTCGTAATGAT
TBR1	Integrated DNA Technologies	Harvard Primer Bank, ID: 22547231c1 Forward GCAGCAGCTACCCACATTCA Reverse AGGTTGTCAGTGGTCGAGATA
SOX2	Integrated DNA Technologies	Forward CCATGCAGGTTGACACCGTTG Reverse TCGGCAGACTGATTCAAATAATACAG
SATB2	Integrated DNA Technologies	Harvard Primer Bank, ID: 289547595c2 Forward GACAGTGGCCGACATGCTAC Reverse AGGCAAGTCTTCCAACTTTGAA
BRN2 (POU3F2)	Integrated DNA Technologies	Harvard Primer Bank, ID: 380254475c1 Forward CGGCGGATCAAACTGGGATTT Reverse TTGCGCTGCGATCTTGTCTAT
CUX1	Integrated DNA Technologies	Harvard Primer Bank, ID: 321400113c1 Forward GAAGAACCAAGCCGAAACCAT Reverse AGGCTCTGAACCTTATGCTCA
VIMENTIN	Integrated DNA Technologies	Harvard Primer Bank, ID: 240849334c2 Forward AGTCCACTGAGTACCGGAGAC Reverse CATTTCACGCATCTGGCGTTC
SOX9	Integrated DNA Technologies	Harvard Primer Bank, ID: 182765453c1 Forward AGCGAACGCACATCAAGAC Reverse CTGTAGGCGATCTGTTGGGG
ALDH1L1	Integrated DNA Technologies	Harvard Primer Bank, ID: 21614512c3 Forward TCCAGACCTTCCGCTACTTTG Reverse CAGGGGATAGTTCCAGGGGAT
Housekeeping primers		
GAPDH	Integrated DNA Technologies	Harvard Primer Bank, ID: 378404907c2 Forward ACAACTTTGGTATCGTGGAAGG Reverse GCCATCACGCCACAGTTTC
GPI (F1/R1)	Integrated DNA Technologies	Forward GTGTACCTTCTAGTCCCGCC Reverse GGTCAAGCTGAAGTGGTTGAAGC
SOFTWARE AND ALGORITHMS		
Image Studio™ Lite	LI-COR	https://www.licor.com/bio/image-studio-lite/download
Fiji	Schindelin et al., 2012	https://imagej.net/Fiji
GraphPad Prism v8.1.2	GraphPad	https://www.graphpad.com/scientific-software/prism/
NIS-Elements	Nikon Instruments	https://www.microscope.healthcare.nikon.com/products/software/nis-elements
MetaboAnalyst 5.0	(Chong and Xia, 2018; Chong et al., 2018, 2019; Xia and Wishart, 2010, 2011a, 2011b; Xia et al., 2009)	https://www.metaboanalyst.ca/home.xhtml

SnpSift	(Cingolani et al., 2012)	http://snpeff.sourceforge.net/SnpSift.html
R 3.5.3	R Foundation	https://www.r-project.org/
BioCircos	(Cui et al., 2016)	https://cran.r-project.org/web/packages/BioCircos/index.html
OTHER		
Mitotracker Red CMXRos	Fisher Scientific	Cat # M7512
Matrigel™	Corning	Cat # 354277
Gentle dissociation solution	STEMCELL Technologies	Cat # 07174
Aggrewell™ 800 24-well plate	STEMCELL Technologies	Cat # 34815
AggreWell™ Rinsing Solution	STEMCELL Technologies	Cat # 07010
STEMdiff™ Cerebral Organoid Kit	STEMCELL Technologies	Cat # 08570
STEMdiff™ Cerebral Organoid Maturation Kit	STEMCELL Technologies	Cat # 08571

662

663 **Lead Contact and Materials Availability**

664 Further information and requests for resources and reagents should be directed to the Lead
665 Contact, Vivian Gama (vivian.gama@vanderbilt.edu).

666

667 **Experimental Model and Subject Details**

668 The Coriell cell line IDs were as follows: GM01503, GM03672, GM1341. Information about the
669 Leigh syndrome cell lines used in this study can be found in Supplementary Table1. Control skin
670 fibroblast cell line AG16409 was also obtained from Coriell Institute, Philadelphia, PA. The donor
671 was a 12-year-old apparently healthy Caucasian male. Cells were negative for Mycoplasma.
672 Fibroblasts were maintained in Dulbecco's Modified Eagle Medium: Nutrient Mixture F-12
673 DMEM/F-12 (Gibco cat # 11330032) supplemented with 10% Fetal bovine serum (Sigma cat#
674 F2442) in 100mm cell culture plates (Eppendorf, cat # 0030702115) in a 37°C 5% CO2 incubator.

675

676 **Method Details**

677 **Whole Exome sequencing**

678 Fibroblast cell pellets from each cell line (>1 million cells) were shipped on dry ice for whole-
679 genome exome sequencing to Genewiz, Plainfield, NJ. The Illumina HiSeq-X was used to perform
680 150nt paired-end sequencing.
681
682 **Mitochondrial sequencing**
683 Fibroblast cell pellets from each patient (>1 million cells) were shipped on dry ice for mitochondrial
684 sequencing to Girihlet Inc. Oakland, CA. The sequencing configuration used was 80bp single-end
685 sequencing, 20 million reads per sample.
686
687 **hiPSC Generation and Characterization**
688 Human fibroblasts were purchased from healthy control and patients (Coriell Institute,
689 Philadelphia, PA, USA). Induced pluripotent stem cells were derived from human fibroblasts using
690 Sendai virus-based reprogramming kit (CytoTune-iPS Sendai Reprogramming Kit; cat #. A13780-
691 01; Thermo Fisher), according to manufacturer's instructions. After 3-4 weeks, 2-3 colonies per
692 sample were transferred to fresh 6-well plates and were expanded and gardened for 3 passages
693 before freezing. All iPSC cell lines were maintained in E8 medium in plates coated with Matrigel
694 (Corning, cat # 354277) at 37°C with 5% CO_2. Culture medium was changed daily. Cells were
695 checked daily for differentiation and were passaged every 3-4 days using Gentle dissociation
696 solution (STEMCELL Technologies, cat # 07174). All experiments were performed under the
697 supervision of the Vanderbilt Institutional Human Pluripotent Cell Research Oversight (VIHPCRO)
698 Committee.
699
700 **Analysis of Pluripotency**
701 The pluripotency of each iPSC clone was determined using a microarray-based tool known as
702 PluriTest (Thermo Fisher; cat# A38154) as an alternative to the teratoma assay. Samples were
703 outsourced to Thermo Fisher for PluriTest and further analysis. Low passage iPSC cell pellets

704 (>1 million cells) were frozen and shipped on dry ice. Additionally, the expression of pluripotency
705 genes *POU5F1* and *NANOG* was assessed by qPCR.
706
707 **Analysis of Chromosomal abnormalities**
708 The presence of any chromosomal abnormalities in the newly generated iPSCs was determined
709 using a microarray-based tool known as KaryoStat (Thermo Fisher; cat# A38153) as an
710 alternative to chromosomal G-banding. Samples were outsourced to Thermo Fisher for KaryoStat
711 and further analysis. Low passage iPSC cell pellets (>1 million cells) were frozen and shipped on
712 dry ice to Thermo Fisher.
713
714 **Trilineage differentiation**
715 The STEMdiff Trilineage differentiation kit (STEMCELL Technologies, cat# 05230) was used to
716 functionally validate the ability of newly established iPSCs to differentiate into three germ layers,
717 as per the manufacturer's instructions. Single-cell suspensions of $2x10^6$ cells/well, $5x10^5$
718 cells/well, $2x10^6$ cells/well were seeded for ectoderm, mesoderm, and endoderm, respectively, in
719 their corresponding medium at day 0 in 6 well plates. The cultures were maintained for 7 days, 5
720 days, and 5 days for ectoderm, mesoderm, and endoderm, respectively. The differentiation was
721 assessed by immunocytochemistry and qPCR.
722
723 **NPC differentiation and multipotency characterization**
724 For monolayer differentiation of the iPSCs into NPCs, cells were dissociated into single cells using
725 Gentle Cell Dissociation Reagent (STEMCELL Technologies, cat # 07174) for 8 minutes at 37°C.
726 Live cell counts were performed using Trypan blue (0.4%) staining (Invitrogen, cat # T10282)
727 using a Countess™ Automated Cell Counter. Cells were then seeded in a Matrigel-coated 6-well
728 plate (Eppendorf, cat # 0030720113) to $2.5x10^6$ cells/well with dual SMAD inhibitor media
729 supplemented with Dorsomorphin (1μM) and SB431542 (10μM) (Chambers et al., 2009)

730 supplemented with ROCK inhibitor. Daily media changes were performed and passaging of the
731 cells was done every 7-9 days. Cells for NPC marker analysis were collected at the end of the
732 first 9 days of differentiation.

733 Mitochondrial imaging was performed by fixing the NPCs at 90% confluency and staining with
734 anti-mitochondria (Abcam, cat #ab92824, 1:200 dilution). Structured Illumination Microscopy
735 (SIM) was accomplished in 3D-SIM mode on a Nikon Instruments N-SIM, equipped with an Apo
736 TIRF 100x SR 1.49NA objective, DU-897 EMCCD camera (Andor), 405nm and 561nm lasers.
737 Images presented herein are maximum intensity projections after image stacks were first acquired
738 (5 phase shifts and 3 rotations of diffraction grating, 120nm/axial step via piezo) and subsequent
739 stack reconstruction in NIS-Elements software (Nikon Instruments, Inc.). Other than linear
740 intensity scaling, no further image processing was performed post-reconstruction.

741 For multipotency analysis, culture media was changed to NeuroCult™ media and maintained for
742 4 weeks. Samples were then fixed and stained for neuron and oligodendrocyte markers. Astrocyte
743 differentiation was performed by seeding on a Matrigel-coated plate $1.5x10^6$ cells/cm^2 (TCW et
744 al., 2017). The following day, the media was changed to Astrocyte medium (ScienCell, cat # 1801)
745 and maintained for 20 days. Full media changes were done every 2 days. Samples were then
746 fixed and stained for an astrocyte marker. Images were acquired with a Nikon Instruments Ti2
747 inverted fluorescence widefield microscope equipped with a Plan Apo Lambda 20X 0.75 NA
748 objective, DS-Qi2 camera (Nikon Instruments), and X-Cite 120LED light source (Excelitas). The
749 differentiation was also assessed by qPCR.

750

751 **Neural rosette differentiation**

752 To generate neural rosettes, we dissociated the cells into a single-cell suspension and seeded
753 $3.0x10^6$ cells/well of an Aggrewell™ 800 in dual SMAD inhibitor media. EBs were incubated at
754 37°C with 5% CO2, with minimal disruption during the first 48 hours. Media changes, 50-75% of

755 the total volume, were performed every 2 days. On Day 5, EBs were harvested according to the
756 manufacturer protocol and transferred to a 35mm imaging plate (Cellvis, cat # D35-14-1.5-N)
757 coated with Matrigel. Daily media changes were performed up to day 9 when cells were fixed with
758 100% ice-cold Methanol (Fisher Scientific, cat # A454-4). Images were acquired on a Nikon
759 Instruments Ti2 inverted fluorescence microscope, equipped with a Yokogawa X1 spinning disk
760 head, Andor DU-897 EMCCD, Plan Apo Lambda 0.75 NA 20X objective for representative figures,
761 and Plan Fluor 0.45 NA 10X objective for neural rosette quantification, piezo Z-stage, as well as
762 405-,488-,561-, and 647 -nm lasers. Acquisition and analysis were performed using NIS-
763 Elements. Neural rosette quantification was accomplished by scripting a segmentation-based
764 image analysis routine to detect, enumerate, and measure rosette lumen area based on the ZO-
765 1 signal. Briefly, max intensity projections of each field were generated, followed by GPU-based
766 denoising of the resulting image. Intensity-based thresholding was then applied based on criteria
767 established for ZO-1 signal segmentation using control images. Restrictions on resultant binaries
768 were implemented to throw out binaries intersecting image borders, morphometries deviating
769 severely from rosette associated geometries, as well as for those not meeting minimum size
770 requirements. This routine could be run in batch across many image stacks to increase the sample
771 size and robust nature of the data. Measured data was exported to Excel for further analysis.
772

773 **Cerebral Organoids**

774 Cerebral organoids were generated as described in (Romero-Morales et al., 2019) with some
775 modifications. Briefly, organoids were generated using the STEMdiff™ Cerebral Organoid Kit
776 (STEMCELL Technologies; Cat# 08571, 08570). iPSCs were dissociated into single cells using
777 Gentle Cell Dissociation Reagent (STEMCELL Technologies, cat # 07174) for 8 minutes at 37°C.
778 Homogeneous and reproducible EBs were generated by using a 24-well plate AggreWell™ 800
779 (STEMCELL Technologies, cat # 34815). On Day 7, high-quality EBs were embedded in Matrigel
780 (Corning, cat # 354277). On Day 10, the Matrigel coat was broken by vigorously pipetting up and

781 down and the healthy organoids were transferred to a 60mm low attachment culture plate
782 (Eppendorf, cat # 003070119). The plates were then moved to a 37°C incubator and to a Celltron
783 benchtop shaker for CO2 incubators (Infors USA, cat # I69222) set at 85rpm. Full media changes
784 were performed every 3–4 days. Transmitted-light images were acquired using an EVOS® XL
785 Core Imaging System. The software used for processing was ImageJ.
786 c. For qPCR, all organoids were pooled together for RNA extraction. Day 40 cerebral organoids
787 were utilized for metabolomics, 4 organoids per genotype were run and analyzed individually.
788

789 **Organoid tissue preparation and Immunohistochemistry**

790 Tissue preparation was performed as described in (Romero-Morales et al., 2019). Briefly,
791 organoids were fixed in 4% Paraformaldehyde in Phosphate Buffered Saline (PBS), washed 3
792 times with PBS, and then incubated in 30% sucrose solution overnight at 4°C. Organoids were
793 embedded in 7.5% gelatin/10% sucrose solution (Sigma, catalog G1890-100G and S7903-250G)
794 and sectioned with a cryostat (Leica CM1950) at 15um thickness. For immunostaining, slides
795 were washed with PBS before permeabilization with 0.2% Triton-X in PBS for 1 hr. Tissues were
796 blocked with blocking medium consisting of 10% donkey serum in PBS with 0.1% Tween-20
797 (PBST) for 30 min. Incubation with primary and secondary antibodies was done using standard
798 methods. Confocal images of the organoids were acquired using the aforementioned spinning
799 disk microscope with Plan Fluor 10X 0.45 NA and Plan Apo Lambda 0.75 NA 20X objectives
800 (macrostructures) and Apo TIRF 1.49 NA 100X objective (mitochondria imaging). NIS-Elements
801 software was used for image acquisition and rendering.
802

803 **RNA Extraction and Synthesis of cDNA**

804 Cells cultured in 6 well plate, were collected after a wash with PBS, using 600µl Trizol reagent.
805 The samples were spun down at 12,000 g after the addition of 130µl of chloroform and incubated
806 at room temperature for 3 minutes. The aqueous phase of the sample was collected 200µl at a

807 time until reaching the edge of phase separation. RNA precipitation was done by incubating with
808 300µl of isopropanol for 25 minutes, followed by centrifugation at 12,000 g for 10 min at 4°C. The
809 RNA pellet was washed with ethanol, semi-dried, and resuspended in 30µl of DEPC water. After
810 quantification and adjusting the volume of all the samples to 1µg/µl, the samples were treated
811 with DNAse (New England Biolabs, cat # M0303). 10µl of this volume was used to generate cDNA
812 using the manufacturer's protocol (Thermofisher, cat#4368814).
813 For RNA isolation from brain organoids, the same protocol mentioned above was followed with
814 the volumes adjusted for 1mL of Trizol.
815

816 **Quantitative RT PCR (RT-qPCR)**

817 1ug of cDNA sample was used to run RT-qPCR for the primers mentioned in the table.
818 QuantStudio 3 Real-Time PCR machine, SYBR green master mix (Thermo Fisher, cat#4364346),
819 and manufacturer instructions were used to set up the assay.
820

821 **Immunocytochemistry**

822 Cells were fixed with 4% paraformaldehyde (Electron Microscopy Sciences, cat # 15710-S) in
823 PBS for 20 min at 4ºC. Blocking and permeabilization were done in 5% donkey serum (Jackson
824 ImmunoResearch Inc, cat # 017-000-121) + 0.3% Triton X-100 (Sigma Aldrich, cat # T9284) in
825 TBS for 1 hr at room temperature. After this, cells were treated with primary and secondary
826 antibodies using standard methods. Cells were mounted in Vectashield (Vector Laboratories, cat
827 # H-1000) prior to imaging.
828

829 **Western Blotting**

830 Cultured cells were lysed in 1% Triton buffer containing PMSF (ThermoFisher Scientific, cat #
831 36978), PhosSTOP (Roche, cat # 4906837001), and protease inhibitor cocktail (Roche, cat #
832 4693132001). Protein concentrations were determined using the bicinchoninic acid (BCA) method

833 (Thermo Scientific, cat # 23227). Gel samples were prepared by mixing 30µg of protein with LDS
834 sample buffer (Life Technologies, cat # NP0007) and 2-Mercaptoethanol (BioRad, cat # 1610710)
835 and boiled at 95°C for 5 minutes. Samples were run on 4-20% Mini-PROTEAN TGX precast gels
836 (BioRad, cat # 4561096) and transferred onto polyvinylidene difluoride (PVDF) membrane
837 (BioRad, cat # 1620177) overnight at 4°C. Membranes were blocked in 5% milk in TBST prior to
838 primary antibody incubation. Antibodies used for Western blotting are described in the Key
839 Resource table.
840
841 **Cell titer blue assay**
842 After the 24-h exposure to individual treatments of 50µM etoposide, 80µM CCCP, 100ng/mL
843 nocodazole, and 5ng/mL neocarzinostatin, 20 µl of Cell Titer Blue reagent from Cell Titer Blue
844 assay (Promega, cat # G8081) was added to each well of 96 well plate. Background fluorescence
845 was calculated by adding 10% Triton in PBS to some wells. The fluorescence generated by the
846 reduction of resazurin to resorufin by live cells was measured using a Beckman coulter DTX 880
847 multimode plate reader (Beckman Coulter, Brea, California) (570/600 nm).
848
849 **Metabolomics analysis**
850 Day 40 brain organoids, at least 4 individual organoids per genotype, were collected rinsed with
851 ice-cold sterile 0.9% NaCl and flash-freeze in liquid nitrogen. For metabolite extraction, cells were
852 resuspended in 225uL of cold 80% HPLC grade methanol/20% HPLC grade water per $1x10^6$ cells.
853 After resuspension, cells were flash-frozen in liquid nitrogen and thawed rapidly in a 37°C water
854 bath 3 times. Next debris was removed by centrifugation at max speed in a tabletop
855 microcentrifuge at 4°C for 15 min. Metabolite-containing supernatant was transferred to a new
856 tube, dried, and resuspended in 50% acetonitrile while the pellet was used for protein
857 quantification. Samples were analyzed by Ultra-High-Performance Liquid Chromatography and
858 High-Resolution Mass Spectrometry and Tandem Mass Spectrometry (UHPLC-MS/MS).

859 Specifically, the system consisted of a Thermo Q-Exactive in line with an electrospray source and
860 an Ultimate3000 (Thermo) series HPLC consisting of a binary pump, degasser, and auto-sampler
861 outfitted with an Xbridge Amide column (Waters; dimensions of 4.6mm × 100mm and a 3.5μm
862 particle size). Mobile phase A contained 95% (vol/vol) water, 5% (vol/vol) acetonitrile, 10mM
863 ammonium hydroxide, 10mM ammonium acetate, pH = 9.0; and mobile phase B was 100%
864 Acetonitrile. The gradient was as follows: 0 min, 15% A; 2.5 min, 30% A; 7 min, 43% A; 16 min,
865 62% A; 16.1-18 min, 75% A; 18-25 min, 15% A with a flow rate of 400μL/min. The capillary of the
866 ESI source was set to 275°C, with sheath gas at 45 arbitrary units, auxiliary gas at 5 arbitrary
867 units, and the spray voltage at 4.0kV. In positive/negative polarity switching mode, an m/z scan
868 range from 70 to 850 was chosen, and MS1 data was collected at a resolution of 70,000. The
869 automatic gain control (AGC) target was set at $1x10^6$ and the maximum injection time was 200
870 ms. The top 5 precursor ions were subsequently fragmented, in a data-dependent manner, using
871 the higher energy collisional dissociation (HCD) cell set to 30% normalized collision energy in
872 MS2 at a resolution power of 17,500. Data acquisition and analysis were carried out by Xcalibur
873 4.1 software and Tracefinder 4.1 software, respectively (both from Thermo Fisher Scientific). The
874 peak area for each detected metabolite was normalized by the total ion current which was
875 determined by the integration of all of the recorded peaks within the acquisition window.

876 Normalized data was uploaded to MetaboAnalyst (https://www.metaboanalyst.ca/home.xhtml) for
877 analysis. Samples were normalized to control, and a one-way ANOVA was performed to compare
878 between the groups. Fisher's least significant difference method (Fisher's LSD) was performed
879 as a post-HOC comparison. Enrichment and pathway analysis was also performed using this
880 platform.

881

882 **Bioinformatic Analysis**

883 Bioinformatic analysis began with Variant Call Format (VCF) files provided by GENEWIZ (see
884 *Whole Exome sequencing* section above), both for SNP and indels. SnpSift version 4.3t
885 (Cingolani et al., 2012) was used to process and filter these files for downstream analysis. Details
886 extracted included gene symbol, Entrez gene ID and name, UniProt ID, Ensembl ID, chromosome
887 and position, reference variant, alternative variant, quality of the call, allele name, type of SNP,
888 impact of the SNP, and the genotype of each sample. From these filtered outputs, we generated
889 SNP/indel reports that allowed us to look at sample-specific SNPs and indels, as well as perform
890 aggregate-level functions for grouping and statistical analysis.

891 To generate the SNP/indel circular chromosome plots, the top 20 genes that had variants in all
892 three samples were plotted, ranked by frequency of variants per gene. The outside track is used
893 to visualize the chromosomes and marked gene locations. For each sample, we used a single
894 track to show the variant frequency as a circular scatter plot, with the height of the scatter points
895 representative of the variant quality metric, which is a Phred-scaled probability that a REF/ALT
896 polymorphism exists at the variant site. Similarly, for SNPs in the mitochondrial chromosome, we
897 used the same approach for visualization.
898

899 **Quantification and Statistical Analysis**

900 No statistical methods were used to pre-determine sample sizes. All experiments were performed
901 with a minimum of 3 biological replicates unless specified. Statistical significance was determined
902 by unpaired Student's t-test or by one- or two-way ANOVA as appropriate for each experiment.
903 GraphPad Prism v8.1.2 was used for all statistical analysis and data visualization.
904 Error bars in all bar graphs represent the standard error of the mean or standard deviation as
905 described for each Figure, while scattered dot plots were represented with boxes (with median
906 and SD) and whiskers (minimum and maximum values).

907 For neural rosette experiments, ROI were randomly selected using the nuclear (DAPI) staining
908 channel. Images were processed with NIS Elements software with our Neural rosette lumen
909 identification Macro. Outliers were removed from the neural rosette area analysis as post-
910 processing quality control for the NIS Element macro using GraphPad Prism v8.1.2. ROUT
911 (Robust regression and Outlier removal) method was used with a False Discovery Rate of 1%.
912 For cerebral organoid experiments, 4 independent batches were generated. At time points day
913 30 and day 100, at least 5 organoids per cell line were collected. Immunofluorescence images of
914 at least 3 independent organoids were acquired per condition slide. Image processing was done
915 by NIS Elements and Fiji software. For the organoid quantification, images were processed with
916 NIS Elements using the General Analysis 3 tool. 3D thresholding macros were generated for each
917 set of slides and quantified by either bright spot count (nuclear staining) or mean intensity of the
918 ROI. For the day 30 mitochondria analysis, the ROUT (Robust regression and Outlier removal)
919 method was used with a False Discovery Rate of 1%.

920 Organoid efficiency evaluation was performed on day 10 using 4X transmitted-light images
921 acquired using an EVOS® XL microscope. Two observers were blinded to the cell line identifier
922 and counted the number of normal and defective (no epithelial buds or more than 75% of the area
923 is not developed) organoids. Criteria for normal and defective organoids was based on (Lancaster
924 and Knoblich, 2014).
925

926 **Software and Data Availability**

927 All raw data in FastQ format for whole-exome sequencing and mitochondrial sequencing have
928 been deposited to the Short Read Archive as BioProject PRJNA626388, available at
929 https://www.ncbi.nlm.nih.gov/sra/PRJNA626388. All source code and documents are available
930 via https://vandydata.github.io/Romero-Morales-Gama-Leigh-Syndrome-WES/.
931

932 **Author contributions**

933 A.R.M. and V.G. designed experiments, interpret the data, and wrote the manuscript. A.R.M.,
934 G.L.R., A.R., and M.L.R. performed experiments and analyzed data with technical support of H.T.
935 J.P.C. and L.H. analyzed the genomic data, generated the corresponding figures, and the
936 associated method section. P.M.A provided pluripotency data analysis and technical support for
937 data analysis. B.M generated the neural rosette analysis macro for NIS Elements. N.S.C., G.S.M.,
938 and R.P.C. provided technical support, led the experimental design and data analysis for
939 metabolomics and its corresponding method section.

940

941 **Conflict of interests**

942 The authors declare no competing interests.

943

944 **Acknowledgments**

945 We thank Dr. Nicholas Mignemi (Vanderbilt Nikon Center for Excellence) for his technical support
946 with image acquisition and processing. We would like to thank members of the Gama Laboratory
947 for helpful discussions and comments on the manuscript. Funding was provided by the following
948 grants: 1R35GM128915-01 (to VG); 1R21 CA227483-01A1 (to VG); the Precision Medicine and
949 Mental Health Initiative sponsored by the Vanderbilt Brain Institute (to VG). Image acquisition and
950 analysis were performed in part through the use of the Nikon Center of Excellence within the
951 Vanderbilt Cell Imaging Shared Resource (supported by NIH grants CA68485, DK20593,
952 DK58404, DK59637, and EY08126), Vanderbilt University Medical Center's Translational
953 Pathology Shared Resource supported by NCI/NIH Cancer Center Support Grant 2P30
954 CA068485-14, and the Vanderbilt Mouse Metabolic Phenotyping Center Grant 5U24DK059637-
955 13. Whole exome sequencing and mitochondrial sequencing results were analyzed by Creative
956 Solutions. Metabolite measurements were performed by the Northwestern University RHLCCC
957 Metabolomics Core (Dr. Peng Gao) and were supported by the following NIH grants to N.S.C.:

958 NIH2PO1HL071643-11A1, NIH1R35CA197532-01, NIH1PO1AG049665-01, NIH/NCI grant to
959 G.S.M: T32CA09560, and Northwestern University Pulmonary and Critical Care Department's
960 Cugell Predoctoral Fellowship to R.P.C.
961

962 **References**

963

964 Agana, M., Frueh, J., Kamboj, M., Patel, D.R., and Kanungo, S. (2018). Common metabolic
965 disorder (inborn errors of metabolism) concerns in primary care practice. Ann. Transl. Med. *6*,
966 469–469.

967 Albrecht, J., and Schousboe, A. (2005). Taurine Interaction with Neurotransmitter Receptors in
968 the CNS: An Update. Neurochem. Res. *30*, 1615–1621.

969 Albright, C.D., Friedrich, C.B., Brown, E.C., Mar, M.H., and Zeisel, S.H. (1999a). Maternal dietary
970 choline availability alters mitosis, apoptosis and the localization of TOAD-64 protein in the
971 developing fetal rat septum. Dev. Brain Res. *115*, 123–129.

972 Albright, C.D., Tsai, A.Y., Friedrich, C.B., Mar, M.-H., and Zeisel, S.H. (1999b). Choline availability
973 alters embryonic development of the hippocampus and septum in the rat. Dev. Brain Res. *113*,
974 13–20.

975 Baertling, F., Rodenburg, R.J., Schaper, J., Smeitink, J.A., Koopman, W.J.H., Mayatepek, E.,
976 Morava, E., and Distelmaier, F. (2014). A guide to diagnosis and treatment of Leigh syndrome. J.
977 Neurol. Neurosurg. Psychiatry *85*, 257–265.

978 Baertling, F., Klee, D., Haack, T.B., Prokisch, H., Meitinger, T., Mayatepek, E., Schaper, J., and
979 Distelmaier, F. (2016). The many faces of paediatric mitochondrial disease on neuroimaging.
980 Child's Nerv. Syst. *32*, 2077–2083.

981 Barshop, B.A. (2004). Metabolomic approaches to mitochondrial disease: Correlation of urine
982 organic acids. Mitochondrion *4*, 521–527.

983 Bélanger, M., Allaman, I., and Magistretti, P.J. (2011). Brain Energy Metabolism: Focus on
984 Astrocyte-Neuron Metabolic Cooperation. Cell Metab. *14*, 724–738.

985 Bhaduri, A., Andrews, M.G., Mancia Leon, W., Jung, D., Shin, D., Allen, D., Jung, D., Schmunk,
986 G., Haeussler, M., Salma, J., et al. (2020). Cell stress in cortical organoids impairs molecular
987 subtype specification. Nature *578*, 142–148.

988 Bridi, R., Latini, A., Braum, C.A., Zorzi, G.K., Wajner, M., Lissi, E., and Dutra-Filho, C.S. (2005).
989 Evaluation of the mechanisms involved in leucine-induced oxidative damage in cerebral cortex of
990 young rats. Free Radic. Res. *39*, 71–79.

991 Bubici, C., and Papa, S. (2019). Editorial: The Warburg Effect Regulation Under Siege: the
992 Intertwined Pathways in Health and Disease. Front. Cell Dev. Biol. *7*, 80.

993 Buniello, A., MacArthur, J.A.L., Cerezo, M., Harris, L.W., Hayhurst, J., Malangone, C., McMahon,
994 A., Morales, J., Mountjoy, E., Sollis, E., et al. (2019). The NHGRI-EBI GWAS Catalog of published
995 genome-wide association studies, targeted arrays and summary statistics 2019. Nucleic Acids
996 Res. *47*, D1005–D1012.

997 Buzkova, J., Nikkanen, J., Ahola, S., Hakonen, A.H., Sevastianova, K., Hovinen, T., Yki-Järvinen,
998 H., Pietiläinen, K.H., Lönnqvist, T., Velagapudi, V., et al. (2018). Metabolomes of mitochondrial
999 diseases and inclusion body myositis patients: treatment targets and biomarkers. EMBO Mol.
1000 Med. *10*.

1001 Calvo, S., Jain, M., Xie, X., Sheth, S.A., Chang, B., Goldberger, O.A., Spinazzola, A., Zeviani, M.,
1002 Carr, S.A., and Mootha, V.K. (2006). Systematic identification of human mitochondrial disease
1003 genes through integrative genomics. Nat. Genet. *38*, 576–582.

1004 Calvo, S.E., Compton, A.G., Hershman, S.G., Lim, S.C., Lieber, D.S., Tucker, E.J., Laskowski,

1005 A., Garone, C., Liu, S., Jaffe, D.B., et al. (2012). Molecular diagnosis of infantile mitochondrial
1006 disease with targeted next-generation sequencing. Sci. Transl. Med. *4*, 118ra10-118ra10.

1007 Camp, J.G., Badsha, F., Florio, M., Kanton, S., Gerber, T., Wilsch-Bräuninger, M., Lewitus, E.,
1008 Sykes, A., Hevers, W., Lancaster, M., et al. (2015). Human cerebral organoids recapitulate gene
1009 expression programs of fetal neocortex development. Proc. Natl. Acad. Sci. *112*, 201520760.

1010 Cansev, M. (2006). Uridine and cytidine in the brain: Their transport and utilization. Brain Res.
1011 Rev. *52*, 389–397.

1012 Cerutti, R., Pirinen, E., Lamperti, C., Marchet, S., Sauve, A.A., Li, W., Leoni, V., Schon, E.A.,
1013 Dantzer, F., Auwerx, J., et al. (2014). NAD+-dependent activation of Sirt1 corrects the phenotype
1014 in a mouse model of mitochondrial disease. Cell Metab. *19*, 1042–1049.

1015 Chambers, S.M., Fasano, C.A., Papapetrou, E.P., Tomishima, M., Sadelain, M., and Studer, L.
1016 (2009). Highly efficient neural conversion of human ES and iPS cells by dual inhibition of SMAD
1017 signaling. Nat. Biotechnol. *27*, 275–280.

1018 Chandrasekaran, A., Avci, H.X., Ochalek, A., Rösingh, L.N., Molnár, K., László, L., Bellák, T.,
1019 Téglási, A., Pesti, K., Mike, A., et al. (2017). Comparison of 2D and 3D neural induction methods
1020 for the generation of neural progenitor cells from human induced pluripotent stem cells. Stem Cell
1021 Res. *25*, 139–151.

1022 Chen, H., and Chan, D.C. (2017). Mitochondrial Dynamics in Regulating the Unique Phenotypes
1023 of Cancer and Stem Cells. Cell Metab. *26*, 39–48.

1024 Chong, J., and Xia, J. (2018). MetaboAnalystR: an R package for flexible and reproducible
1025 analysis of metabolomics data. Bioinformatics *34*, 4313–4314.

1026 Chong, J., Soufan, O., Li, C., Caraus, I., Li, S., Bourque, G., Wishart, D.S., and Xia, J. (2018).
1027 MetaboAnalyst 4.0: towards more transparent and integrative metabolomics analysis. Nucleic
1028 Acids Res. *46*, W486–W494.

1029 Chong, J., Wishart, D.S., and Xia, J. (2019). Using MetaboAnalyst 4.0 for Comprehensive and
1030 Integrative Metabolomics Data Analysis. Curr. Protoc. Bioinforma. *68*.

1031 Cingolani, P., Patel, V.M., Coon, M., Nguyen, T., Land, S.J., Ruden, D.M., and Lu, X. (2012).
1032 Using Drosophila melanogaster as a model for genotoxic chemical mutational studies with a new
1033 program, SnpSift. Front. Genet. *3*, 35.

1034 Cipriani, S., Journiac, N., Nardelli, J., Verney, C., Delezoide, A.-L., Guimiot, F., Gressens, P., and
1035 Adle-Biassette, H. (2015). Dynamic Expression Patterns of Progenitor and Neuron Layer Markers
1036 in the Developing Human Dentate Gyrus and Fimbria. Cereb. Cortex *27*, bhv223.

1037 Clarke, L.E., Liddelow, S.A., Chakraborty, C., Münch, A.E., Heiman, M., and Barres, B.A. (2018).
1038 Normal aging induces A1-like astrocyte reactivity. Proc. Natl. Acad. Sci. *115*, E1896–E1905.

1039 Craigen, W.J. (1996). Leigh disease with deficiency of lipoamide dehydrogenase: Treatment
1040 failure with dichloroacetate. Pediatr. Neurol. *14*, 69–71.

1041 Craven, L., Alston, C.L., Taylor, R.W., and Turnbull, D.M. (2017). Recent Advances in
1042 Mitochondrial Disease. Annu. Rev. Genomics Hum. Genet. *18*, 257–275.

1043 Cui, Y., Chen, X., Luo, H., Fan, Z., Luo, J., He, S., Yue, H., Zhang, P., and Chen, R. (2016).
1044 BioCircos.js: An interactive Circos JavaScript library for biological data visualization on web
1045 applications. Bioinformatics *32*, 1740–1742.

1046 Das, A.M., Steuerwald, U., and Illsinger, S. (2010). Inborn errors of energy metabolism associated
1047 with myopathies. J. Biomed. Biotechnol. *2010*.

1048 Elkabetz, Y., Panagiotakos, G., Al Shamy, G., Socci, N.D., Tabar, V., and Studer, L. (2008).
1049 Human ES cell-derived neural rosettes reveal a functionally distinct early neural stem cell stage.
1050 Genes Dev. *22*, 152–165.

1051 Englund, C. (2005). Pax6, Tbr2, and Tbr1 Are Expressed Sequentially by Radial Glia,
1052 Intermediate Progenitor Cells, and Postmitotic Neurons in Developing Neocortex. J. Neurosci. *25*,
1053 247–251.

1054 Escartin, C., Galea, E., Lakatos, A., O'Callaghan, J.P., Petzold, G.C., Serrano-Pozo, A.,
1055 Steinhäuser, C., Volterra, A., Carmignoto, G., Agarwal, A., et al. (2021). Reactive astrocyte
1056 nomenclature, definitions, and future directions. Nat. Neurosci. *24*, 312–325.

1057 Esterhuizen, K., van der Westhuizen, F.H., and Louw, R. (2017). Metabolomics of mitochondrial
1058 disease. Mitochondrion *35*, 97–110.

1059 Fang, Q., Zhang, Y., Chen, X., Li, H., Cheng, L., Zhu, W., Zhang, Z., Tang, M., Liu, W., Wang, H.,
1060 et al. (2020). Three-Dimensional Graphene Enhances Neural Stem Cell Proliferation Through
1061 Metabolic Regulation. Front. Bioeng. Biotechnol. *7*, 436.

1062 Fedorova, V., Vanova, T., Elrefae, L., Pospisil, J., Petrasova, M., Kolajova, V., Hudacova, Z.,
1063 Baniariova, J., Barak, M., Peskova, L., et al. (2019). Differentiation of neural rosettes from human
1064 pluripotent stem cells in vitro is sequentially regulated on a molecular level and accomplished by
1065 the mechanism reminiscent of secondary neurulation. Stem Cell Res. *40*, 101563.

1066 Feeney, C.L., Lim, A.Z., Fagan, E., Blain, A., Bright, A., Maddison, J., Devine, H., Stewart, J.,
1067 Taylor, R.W., Gorman, G.S., et al. (2019). A case-comparison study of pregnant women with
1068 mitochondrial disease – what to expect? BJOG An Int. J. Obstet. Gynaecol. *126*, 1380–1389.

1069 Ferlin, T., Landrieu, P., Rambaud, C., Fernandez, H., Dumoulin, R., Rustin, P., and Mousson, B.
1070 (1997). Segregation of the G8993 mutant mitochondrial DNA through generations and embryonic
1071 tissues family at risk of Leigh syndrome. J. Pediatr. *131*, 447–449.

1072 Ferrari, M., Jain, I.H., Goldberger, O., Rezoagli, E., Thoonen, R., Chen, K.-H., Sosnovik, D.E.,
1073 Scherrer-Crosbie, M., Mootha, V.K., and Zapol, W.M. (2017). Hypoxia treatment reverses
1074 neurodegenerative disease in a mouse model of Leigh syndrome. Proc. Natl. Acad. Sci. *114*,
1075 E4241–E4250.

1076 Finsterer, J. (2008). Leigh and Leigh-Like Syndrome in Children and Adults. Pediatr. Neurol. *39*,
1077 223–235.

1078 Florio, M., and Huttner, W.B. (2014). Neural progenitors, neurogenesis and the evolution of the
1079 neocortex. Development *141*, 2182–2194.

1080 Francklyn, C.S., and Mullen, P. (2019). Progress and challenges in aminoacyl-tRNA synthetase-
1081 based therapeutics. J. Biol. Chem. *294*, 5365–5385.

1082 Fumagalli, M., Lecca, D., Abbracchio, M.P., and Ceruti, S. (2017). Pathophysiological Role of
1083 Purines and Pyrimidines in Neurodevelopment: Unveiling New Pharmacological Approaches to
1084 Congenital Brain Diseases. Front. Pharmacol. *8*, 941.

1085 Galera-Monge, T., Zurita-Díaz, F., González-Páramos, C., Moreno-Izquierdo, A., Fraga, M.F.,
1086 Fernández, A.F., Garesse, R., and Gallardo, M.E. (2016). Generation of a human iPSC line from
1087 a patient with Leigh syndrome caused by a mutation in the MT-ATP6 gene. Stem Cell Res. *16*,
1088 766–769.

1089 García-Cazorla, A., Oyarzabal, A., Fort, J., Robles, C., Castejón, E., Ruiz-Sala, P., Bodoy, S.,
1090 Merinero, B., Lopez-Sala, A., Dopazo, J., et al. (2014). Two Novel Mutations in the BCKDK
1091 (Branched-Chain Keto-Acid Dehydrogenase Kinase) Gene Are Responsible for a

1092 Neurobehavioral Deficit in Two Pediatric Unrelated Patients. Hum. Mutat. *35*, 470–477.

1093 Geng, X., Shen, J., Li, F., Yip, J., Guan, L., Rajah, G., Peng, C., DeGracia, D., and Ding, Y.
1094 (2021). Phosphoenolpyruvate Carboxykinase (PCK) in the Brain Gluconeogenic Pathway
1095 Contributes to Oxidative and Lactic Injury After Stroke. Mol. Neurobiol. 1–13.

1096 Gerards, M., Sallevelt, S.C.E.H., and Smeets, H.J.M. (2016). Leigh syndrome: Resolving the
1097 clinical and genetic heterogeneity paves the way for treatment options. Mol. Genet. Metab. *117*,
1098 300–312.

1099 Gogos, J.A., Santha, M., Takacs, Z., Beck, K.D., Luine, V., Lucas, L.R., Nadler, J.V., and
1100 Karayiorgou, M. (1999). The gene encoding proline dehydrogenase modulates sensorimotor
1101 gating in mice. Nat. Genet. *21*, 434–439.

1102 Gorman, G.S., Chinnery, P.F., DiMauro, S., Hirano, M., Koga, Y., McFarland, R., Suomalainen,
1103 A., Thorburn, D.R., Zeviani, M., and Turnbull, D.M. (2016). Mitochondrial diseases. Nat. Rev. Dis.
1104 Prim. *2*, 1–22.

1105 Grace, H.E., Galdun, P., Lesnefsky, E.J., West, F.D., and Iyer, S. (2019). MRNA Reprogramming
1106 of T8993G Leigh's Syndrome Fibroblast Cells to Create Induced Pluripotent Stem Cell Models for
1107 Mitochondrial Disorders. Stem Cells Dev. *28*, 846–859.

1108 Grier, J., Hirano, M., Karaa, A., Shepard, E., and Thompson, J.L.P. (2018). Diagnostic odyssey
1109 of patients with mitochondrial disease Results of a survey. Neurol. Genet. *4*.

1110 Hakim, A.M., Moss, G., and Scuderi, D. (1980). The Pentose Phosphate Pathway in Brain during
1111 Development. Neonatology *37*, 15–21.

1112 Halim, N.D., Mcfate, T., Mohyeldin, A., Okagaki, P., Korotchkina, L.G., Patel, M.S., Jeoung, N.H.,
1113 Harris, R.A., Schell, M.J., and Verma, A. (2010). Phosphorylation status of pyruvate
1114 dehydrogenase distinguishes metabolic phenotypes of cultured rat brain astrocytes and neurons.
1115 Glia *58*, 1168–1176.

1116 Harding, A.E., Holt, I.J., Sweeney, M.G., Brockington, M., and Davis, M.B. (1992). Prenatal
1117 diagnosis of mitochondrial DNA8993 T→G disease. Am. J. Hum. Genet. *50*, 629–633.

1118 Hattori, T., Hamazaki, T., Kudo, S., and Shintaku, H. (2016). Metabolic Signature of MELAS/Leigh
1119 Overlap Syndrome in Patient-specific Induced Pluripotent Stem Cells Model. Osaka City Med. J.
1120 *62*, 69–76.

1121 Hinman, L.M., Sheu, K.-F.R., Baker, A.C., Kim, Y.T., and Blass, J.P. (1989). Deficiency of
1122 pyruvate dehydrogenase complex (PDHC) in Leigh's disease fibroblasts: An abnormality in
1123 lipoamide dehydrogenase affecting PDHC activation. Neurology *39*, 70–70.

1124 Homem, C.C.F., Repic, M., and Knoblich, J.A. (2015). Proliferation control in neural stem and
1125 progenitor cells. Nat. Rev. Neurosci. *16*, 647–659.

1126 Hříbková, H., Grabiec, M., Klemová, D., Slaninová, I., and Sun, Y.-M. (2018). Five steps to form
1127 neural rosettes: structure and function. J. Cell Sci. *131*, jcs206896.

1128 Huh, T.L., Casazza, J.P., Huh, J.W., Chi, Y.T., and Song, B.J. (1990). Characterization of two
1129 cDNA clones for pyruvate dehydrogenase E1β subunit and its regulation in tricarboxylic acid
1130 cycle-deficient fibroblast. J. Biol. Chem. *265*, 13320–13326.

1131 Hutton, S.R., and Pevny, L.H. (2011). SOX2 expression levels distinguish between neural
1132 progenitor populations of the developing dorsal telencephalon. Dev. Biol. *352*, 40–47.

1133 Inak, G., Lorenz, C., Lisowski, P., Zink, A., Mlody, B., and Prigione, A. (2017). Concise Review:
1134 Induced Pluripotent Stem Cell-Based Drug Discovery for Mitochondrial Disease. Stem Cells *35*,

1655–1662.

Inak, G., Rybak-Wolf, A., Lisowski, P., Juettner, R., Zink, A., Mlody, B., Glazar, P., Secker, C., Ciptasari, U.H., Stenzel, W., et al. (2019). SURF1 mutations causative of Leigh syndrome impair human neurogenesis. BioRxiv 551390.

Inak, G., Rybak-Wolf, A., Lisowski, P., Pentimalli, T.M., Jüttner, R., Glažar, P., Uppal, K., Bottani, E., Brunetti, D., Secker, C., et al. (2021). Defective metabolic programming impairs early neuronal morphogenesis in neural cultures and an organoid model of Leigh syndrome. Nat. Commun. *12*, 1–22.

Itoh, Y., Esaki, T., Shimoji, K., Cook, M., Law, M.J., Kaufman, E., and Sokoloff, L. (2003). Dichloroacetate effects on glucose and lactate oxidation by neurons and astroglia in vitro and on glucose utilization by brain in vivo. Proc. Natl. Acad. Sci. *100*, 4879–4884.

Itskovitz-Eldor, J., Schuldiner, M., Karsenti, D., Eden, A., Yanuka, O., Amit, M., Soreq, H., and Benvenisty, N. (2000). Differentiation of Human Embryonic Stem Cells into Embryoid Bodies Comprising the Three Embryonic Germ Layers. Mol. Med. *6*, 88–95.

Iwata, R., Casimir, P., and Vanderhaeghen, P. (2020). Mitochondrial dynamics in postmitotic cells regulate neurogenesis. Science (80-.). *369*, 858–862.

Iyer, S., Bergquist, K., Young, K., Gnaiger, E., Rao, R.R., and Bennett, J.P. (2012). Mitochondrial Gene Therapy Improves Respiration, Biogenesis, and Transcription in G11778A Leber's Hereditary Optic Neuropathy and T8993G Leigh's Syndrome Cells. Hum. Gene Ther. *23*, 647–657.

Jain, I.H., Zazzeron, L., Goli, R., Alexa, K., Schatzman-Bone, S., Dhillon, H., Goldberger, O., Peng, J., Shalem, O., Sanjana, N.E., et al. (2016). Hypoxia as a therapy for mitochondrial disease. Science (80-.). *352*, 54–61.

Jain, I.H., Zazzeron, L., Goldberger, O., Marutani, E., Wojtkiewicz, G.R., Ast, T., Wang, H., Schleifer, G., Stepanova, A., Brepoels, K., et al. (2019). Leigh Syndrome Mouse Model Can Be Rescued by Interventions that Normalize Brain Hyperoxia, but Not HIF Activation. Cell Metab. *0*, 824-832.e3.

Jiang, W., Tian, X., Yang, P., Li, J., Xiao, L., Liu, J., Liu, C., Tan, W., and Tu, H. (2019). Enolase1 Alleviates Cerebral Ischemia-Induced Neuronal Injury via Its Enzymatic Product Phosphoenolpyruvate. ACS Chem. Neurosci. *10*, 2877–2889.

Johnson, S.C., Martinez, F., Bitto, A., Gonzalez, B., Tazaerslan, C., Cohen, C., Delaval, L., Timsit, J., Knebelmann, B., Terzi, F., et al. (2019). mTOR inhibitors may benefit kidney transplant recipients with mitochondrial diseases. Kidney Int. *95*, 455–466.

Kelava, I., and Lancaster, M.A. (2016). Stem Cell Models of Human Brain Development. Cell Stem Cell *18*, 736–748.

Khacho, M., Clark, A., Svoboda, D.S., Azzi, J., MacLaurin, J.G., Meghaizel, C., Sesaki, H., Lagace, D.C., Germain, M., Harper, M.E., et al. (2016). Mitochondrial Dynamics Impacts Stem Cell Identity and Fate Decisions by Regulating a Nuclear Transcriptional Program. Cell Stem Cell.

Kuang, Y.-L., Munoz, A., Nalula, G., Santostefano, K.E., Sanghez, V., Sanchez, G., Terada, N., Mattis, A.N., Iacovino, M., Iribarren, C., et al. (2019). Evaluation of commonly used ectoderm markers in iPSC trilineage differentiation. Stem Cell Res. *37*, 101434.

Kühlbrandt, W., and Davies, K.M. (2016). Rotary ATPases: A New Twist to an Ancient Machine. Trends Biochem. Sci. *41*, 106–116.

Kumps, A., Duez, P., and Mardens, Y. (2002). Metabolic, nutritional, iatrogenic, and artifactual

1179 sources of urinary organic acids: A comprehensive table. Clin. Chem.

1180 Lake, N.J., Bird, M.J., Isohanni, P., and Paetau, A. (2015). Leigh syndrome: neuropathology and
1181 pathogenesis. J. Neuropathol. Exp. Neurol. *74*, 482–492.

1182 Lake, N.J., Compton, A.G., Rahman, S., and Thorburn, D.R. (2016). Leigh syndrome: One
1183 disorder, more than 75 monogenic causes. Ann. Neurol. *79*, 190–203.

1184 Lancaster, M.A., and Knoblich, J.A. (2014). Generation of cerebral organoids from human
1185 pluripotent stem cells. Nat. Protoc. *9*, 2329–2340.

1186 Lancaster, M.A., Corsini, N.S., Wolfinger, S., Gustafson, E.H., Phillips, A.W., Burkard, T.R., Otani,
1187 T., Livesey, F.J., and Knoblich, J.A. (2017). Guided self-organization and cortical plate formation
1188 in human brain organoids. Nat. Publ. Gr. *35*.

1189 Laughton, J.D., Bittar, P., Charnay, Y., Pellerin, L., Kovari, E., Magistretti, P.J., and Bouras, C.
1190 (2007). Metabolic compartmentalization in the human cortex and hippocampus: evidence for a
1191 cell- and region-specific localization of lactate dehydrogenase 5 and pyruvate dehydrogenase.
1192 BMC Neurosci. *8*, 35.

1193 Leigh, D. (1951). Subacute necrotizing encephalomyelopathy in an infant. J. Neurol. Neurosurg.
1194 Psychiatry *14*, 216–221.

1195 Leone, D.P., Srinivasan, K., Chen, B., Alcamo, E., and McConnell, S.K. (2008). The determination
1196 of projection neuron identity in the developing cerebral cortex. Curr. Opin. Neurobiol. *18*, 28–35.

1197 Liddelow, S.A., and Barres, B.A. (2017). Reactive Astrocytes: Production, Function, and
1198 Therapeutic Potential. Immunity *46*, 957–967.

1199 Liddelow, S.A., Guttenplan, K.A., Clarke, L.E., Bennett, F.C., Bohlen, C.J., Schirmer, L., Bennett,
1200 M.L., Münch, A.E., Chung, W.-S., Peterson, T.C., et al. (2017). Neurotoxic reactive astrocytes are
1201 induced by activated microglia. Nature *541*, 481–487.

1202 Lorenz, C., Lesimple, P., Bukowiecki, R., Zink, A., Inak, G., Mlody, B., Singh, M., Semtner, M.,
1203 Mah, N., Auré, K., et al. (2017). Human iPSC-Derived Neural Progenitors Are an Effective Drug
1204 Discovery Model for Neurological mtDNA Disorders. Cell Stem Cell *20*, 659-674.e9.

1205 Lui, J.H., Hansen, D. V., and Kriegstein, A.R. (2011). Development and evolution of the human
1206 neocortex. Cell *146*, 18–36.

1207 Di Lullo, E., and Kriegstein, A.R. (2017). The use of brain organoids to investigate neural
1208 development and disease. Nat. Rev. Neurosci. *18*, 573–584.

1209 Ma, H., Folmes, C.D.L., Wu, J., Morey, R., Mora-Castilla, S., Ocampo, A., Ma, L., Poulton, J.,
1210 Wang, X., Ahmed, R., et al. (2015). Metabolic rescue in pluripotent cells from patients with mtDNA
1211 disease. Nature *524*, 234–238.

1212 Manoli, I., and Venditti, C.P. (2016). Disorders of branched chain amino acid metabolism. Transl.
1213 Sci. Rare Dis. *1*, 91–110.

1214 Marton, R.M., Miura, Y., Sloan, S.A., Li, Q., Revah, O., Levy, R.J., Huguenard, J.R., and Pașca,
1215 S.P. (2019). Differentiation and maturation of oligodendrocytes in human three-dimensional
1216 neural cultures. Nat. Neurosci. *22*, 484–491.

1217 Mathieu, J., and Ruohola-Baker, H. (2017). Metabolic remodeling during the loss and acquisition
1218 of pluripotency. Dev. *144*, 541–551.

1219 Medelnik, J.-P., Roensch, K., Okawa, S., del Sol, A., Chara, O., Mchedlishvili, L., and Tanaka,
1220 E.M. (2018). Signaling-Dependent Control of Apical Membrane Size and Self-Renewal in Rosette-
1221 Stage Human Neuroepithelial Stem Cells. Stem Cell Reports *10*, 1751–1765.

1222 Di Meo, I., Marchet, S., Lamperti, C., Zeviani, M., and Viscomi, C. (2017). AAV9-based gene
1223 therapy partially ameliorates the clinical phenotype of a mouse model of Leigh syndrome. Gene
1224 Ther. *24*, 661–667.

1225 Müller, F.J., Schuldt, B.M., Williams, R., Mason, D., Altun, G., Papapetrou, E.P., Danner, S.,
1226 Goldmann, J.E., Herbst, A., Schmidt, N.O., et al. (2011). A bioinformatic assay for pluripotency in
1227 human cells. Nat. Methods *8*, 315–317.

1228 Muratore, C.R., Srikanth, P., Callahan, D.G., and Young-Pearse, T.L. (2014). Comparison and
1229 optimization of hiPSC forebrain cortical differentiation protocols. PLoS One *9*, e105807.

1230 Nesbitt, V., Alston, C.L., Blakely, E.L., Fratter, C., Feeney, C.L., Poulton, J., Brown, G.K., Turnbull,
1231 D.M., Taylor, R.W., and McFarland, R. (2014). A national perspective on prenatal testing for
1232 mitochondrial disease. Eur. J. Hum. Genet. *22*, 1255–1259.

1233 Nieto, M., Monuki, E.S., Tang, H., Imitola, J., Haubst, N., Khoury, S.J., Cunningham, J., Gotz, M.,
1234 and Walsh, C.A. (2004). Expression of Cux-1 and Cux-2 in the subventricular zone and upper
1235 layers II-IV of the cerebral cortex. J. Comp. Neurol. *479*, 168–180.

1236 Ognjenović, J., and Simonović, M. (2018). Human aminoacyl-tRNA synthetases in diseases of
1237 the nervous system. RNA Biol. *15*, 623–634.

1238 Oshida, K., Shimizu, T., Takase, M., Tamura, Y., Shimizu, T., and Yamashiro, Y. (2003). Effects
1239 of dietary sphingomyelin on central nervous system myelination in developing rats. Pediatr. Res.
1240 *53*, 589–593.

1241 Pampaloni, F., Reynaud, E.G., and Stelzer, E.H.K. (2007). The third dimension bridges the gap
1242 between cell culture and live tissue. Nat. Rev. Mol. Cell Biol. *8*, 839–845.

1243 Panopoulos, A.D., Yanes, O., Ruiz, S., Kida, Y.S., Diep, D., Tautenhahn, R., Herrerías, A.,
1244 Batchelder, E.M., Plongthongkum, N., Lutz, M., et al. (2012). The metabolome of induced
1245 pluripotent stem cells reveals metabolic changes occurring in somatic cell reprogramming. Cell
1246 Res. *22*, 168–177.

1247 Parikh, S., Goldstein, A., Karaa, A., Koenig, M.K., Anselm, I., Brunel-Guitton, C., Christodoulou,
1248 J., Cohen, B.H., Dimmock, D., Enns, G.M., et al. (2017). Patient care standards for primary
1249 mitochondrial disease: A consensus statement from the mitochondrial medicine society. Genet.
1250 Med. *19*, 1–18.

1251 Paşca, A.M., Sloan, S.A., Clarke, L.E., Tian, Y., Makinson, C.D., Huber, N., Kim, C.H., Park, J.-
1252 Y., O'Rourke, N.A., Nguyen, K.D., et al. (2015). Functional cortical neurons and astrocytes from
1253 human pluripotent stem cells in 3D culture. Nat Methods. *12*, 671–678.

1254 Pașca, S.P. (2018). The rise of three-dimensional human brain cultures. Nature *553*, 437–445.

1255 Pastores, G.M., Santorelli, F.M., Shanske, S., Gelb, B.D., Fyfe, B., Wolfe, D., and Willner, J.P.
1256 (1994). Leigh syndrome and hypertrophic cardiomyopathy in an infant with a mitochondrial DNA
1257 point mutation (T8993G). Am. J. Med. Genet. *50*, 265–271.

1258 Qi, Y., Zhang, X.-J., Renier, N., Wu, Z., Atkin, T., Sun, Z., Ozair, M.Z., Tchieu, J., Zimmer, B.,
1259 Fattahi, F., et al. (2017). Combined small-molecule inhibition accelerates the derivation of
1260 functional cortical neurons from human pluripotent stem cells. Nat. Biotechnol. *35*, 154–163.

1261 Quadrato, G., Brown, J., and Arlotta, P. (2016). The promises and challenges of human brain
1262 organoids as models of neuropsychiatric disease. Nat. Med. *22*, 1220–1228.

1263 Rafelski, S.M. (2013). Mitochondrial network morphology: Building an integrative, geometrical
1264 view. BMC Biol. *11*, 71.

1265 Rahman, J., and Rahman, S. (2018). Mitochondrial medicine in the omics era. Lancet *391*, 2560–
1266 2574.

1267 Rasmussen, M.L., and Gama, V. (2020). A connection in life and death: The BCL-2 family
1268 coordinates mitochondrial network dynamics and stem cell fate. In International Review of Cell
1269 and Molecular Biology, (Elsevier Inc.), p.

1270 Rastogi, A., Joshi, P., Contreras, E., and Gama, V. (2019). Remodeling of mitochondrial
1271 morphology and function: an emerging hallmark of cellular reprogramming. Cell Stress *3*, 181–
1272 194.

1273 Rema, V., Bali, K.K., Ramachandra, R., Chugh, M., Darokhan, Z., and Chaudhary, R. (2008).
1274 Cytidine-5-diphosphocholine supplement in early life induces stable increase in dendritic
1275 complexity of neurons in the somatosensory cortex of adult rats. Neuroscience *155*, 556–564.

1276 Robel, S., Mori, T., Zoubaa, S., Schlegel, J., Sirko, S., Faissner, A., Goebbels, S., Dimou, L., and
1277 Götz, M. (2009). Conditional deletion of β1-integrin in astroglia causes partial reactive gliosis. Glia
1278 *57*, 1630–1647.

1279 Robel, S., Berninger, B., and Götz, M. (2011). The stem cell potential of glia: Lessons from
1280 reactive gliosis. Nat. Rev. Neurosci. *12*, 88–104.

1281 Roberts, B., Hendershott, M.C., Arakaki, J., Gerbin, K.A., Malik, H., Nelson, A., Gehring, J.,
1282 Hookway, C., Ludmann, S.A., Yang, R., et al. (2019). Fluorescent Gene Tagging of
1283 Transcriptionally Silent Genes in hiPSCs. Stem Cell Reports *12*, 1145–1158.

1284 Romero-Morales, A.I., O'Grady, B.J., Balotin, K.M., Bellan, L.M., Lippmann, E.S., and Gama, V.
1285 (2019). Spin∞ an improved miniaturized spinning bioreactor for the generation of human cerebral
1286 organoids from pluripotent stem cells. BioRxiv 687095.

1287 Saito, T., Hanai, S., Takashima, S., Nakagawa, E., Okazaki, S., Inoue, T., Miyata, R., Hoshino,
1288 K., Akashi, T., Sasaki, M., et al. (2011). Neocortical Layer Formation of Human Developing Brains
1289 and Lissencephalies: Consideration of Layer-Specific Marker Expression. Cereb. Cortex *21*, 588–
1290 596.

1291 Sansom, S.N., Griffiths, D.S., Faedo, A., Kleinjan, D.-J., Ruan, Y., Smith, J., van Heyningen, V.,
1292 Rubenstein, J.L., and Livesey, F.J. (2009). The Level of the Transcription Factor Pax6 Is Essential
1293 for Controlling the Balance between Neural Stem Cell Self-Renewal and Neurogenesis. PLoS
1294 Genet. *5*, e1000511.

1295 Schaefer, A., Lim, A., and Gorman, G. (2019). Epidemiology of Mitochondrial Disease. In
1296 Diagnosis and Management of Mitochondrial Disorders, (Cham: Springer International
1297 Publishing), pp. 63–79.

1298 Schubert, M.B., and Vilarinho, L. (2020). Molecular basis of Leigh syndrome: A current look.
1299 Orphanet J. Rare Dis. *15*, 1–14.

1300 Seth, E.A., Lee, H.-C., Yusof, H.H. bin M., Nordin, N., Cheah, Y.K., Ho, E.T.W., Ling, K.-H., and
1301 Cheah, P.-S. (2020). Phenotype microarrays reveal metabolic dysregulations of neurospheres
1302 derived from embryonic Ts1Cje mouse model of Down syndrome. PLoS One *15*, e0236826.

1303 Sofou, K., De Coo, I.F.M., Isohanni, P., Ostergaard, E., Naess, K., De Meirleir, L., Tzoulis, C.,
1304 Uusimaa, J., De Angst, I.B., Lonnqvist, T., et al. (2014). A multicenter study on Leigh syndrome:
1305 disease course and predictors of survival. Orphanet J. Rare Dis. *9*, 52.

1306 Song, C., Xu, F., Ren, Z., Zhang, Y., Meng, Y., Yang, Y., Lingadahalli, S., Cheung, E., Li, G., Liu,
1307 W., et al. (2019). Elevated Exogenous Pyruvate Potentiates Mesodermal Differentiation through
1308 Metabolic Modulation and AMPK/mTOR Pathway in Human Embryonic Stem Cells. Stem Cell

1309 Reports *13*, 338–351.

1310 Sorbi, S., and Blass, J.P. (1982). Abnormal activation of private dehydrogenase in Leigh disease
1311 fibroblasts. Neurology *32*, 555–555.

1312 Steffann, J., Gigarel, N., Corcos, J., Bonnière, M., Encha-Razavi, F., Sinico, M., Prevot, S.,
1313 Dumez, Y., Yamgnane, A., Frydman, R., et al. (2007). Stability of the m.8993T→G mtDNA
1314 mutation load during human embryofetal development has implications for the feasibility of
1315 prenatal diagnosis in NARP syndrome. J. Med. Genet. *44*, 664–669.

1316 Stern, H.J. (1994). Lactic acidosis in paediatrics: Clinical and laboratory evaluation. Ann. Clin.
1317 Biochem. *31*, 410–419.

1318 Sturman, J.A. (1993). Taurine in development. Physiol. Rev. *73*, 119–148.

1319 Sukhorukov, V.M., Dikov, D., Reichert, A.S., and Meyer-Hermann, M. (2012). Emergence of the
1320 Mitochondrial Reticulum from Fission and Fusion Dynamics. PLoS Comput. Biol. *8*, e1002745.

1321 Sun, W., Cornwell, A., Li, J., Peng, S., Joana Osorio, M., Aalling, N., Wang, S., Benraiss, A., Lou,
1322 N., Goldman, S.A., et al. (2017). SOX9 is an astrocyte-specific nuclear marker in the adult brain
1323 outside the neurogenic regions. J. Neurosci. *37*, 4493–4507.

1324 Takahashi, K., Tanabe, K., Ohnuki, M., Narita, M., Ichisaka, T., Tomoda, K., and Yamanaka, S.
1325 (2007). Induction of Pluripotent Stem Cells from Adult Human Fibroblasts by Defined Factors. Cell
1326 *131*, 861–872.

1327 TCW, J., Wang, M., Pimenova, A.A., Bowles, K.R., Hartley, B.J., Lacin, E., Machlovi, S.I.,
1328 Abdelaal, R., Karch, C.M., Phatnani, H., et al. (2017). An Efficient Platform for Astrocyte
1329 Differentiation from Human Induced Pluripotent Stem Cells. Stem Cell Reports *9*, 600–614.

1330 Tibbitt, M.W., and Anseth, K.S. (2012). Dynamic microenvironments: The fourth dimension. Sci.
1331 Transl. Med. *4*, 160ps24-160ps24.

1332 Uittenbogaard, M., Brantner, C.A., Fang, Z.S., Wong, L.J.C., Gropman, A., and Chiaramello, A.
1333 (2018). Novel insights into the functional metabolic impact of an apparent de novo m.8993T>G
1334 variant in the MT-ATP6 gene associated with maternally inherited form of Leigh Syndrome. Mol.
1335 Genet. Metab. *124*, 71–81.

1336 Vescovi, A.L., and Snyder, E.Y. (1999). Establishment and properties of neural stem cell clones:
1337 Plasticity in vitro and in vivo. In Brain Pathology, (International Society of Neuropathology), pp.
1338 569–598.

1339 Vo, T.D., Paul Lee, W.N., and Palsson, B.O. (2007). Systems analysis of energy metabolism
1340 elucidates the affected respiratory chain complex in Leigh's syndrome. Mol. Genet. Metab. *91*,
1341 15–22.

1342 Vorstman, J.A.S., Turetsky, B.I., Sijmens-Morcus, M.E.J., De Sain, M.G., Dorland, B., Sprong,
1343 M., Rappaport, E.F., Beemer, F.A., Emanuel, B.S., Kahn, R.S., et al. (2009). Proline affects brain
1344 function in 22q11DS children with the low activity COMT158 allele. Neuropsychopharmacology
1345 *34*, 739–746.

1346 Westrate, L.M., Drocco, J.A., Martin, K.R., Hlavacek, W.S., and MacKeigan, J.P. (2014).
1347 Mitochondrial morphological features are associated with fission and fusion events. PLoS One *9*,
1348 95265.

1349 White, S.L., Collins, V.R., Wolfe, R., Cleary, M.A., Shanske, S., DiMauro, S., Dahl, H.H.M., and
1350 Thorburn, D.R. (1999). Genetic counseling and prenatal diagnosis for the mitochondrial DNA
1351 mutations at nucleotide 8993. Am. J. Hum. Genet. *65*, 474–482.

Wilson, P.G., and Stice, S.S. (2006). Development and differentiation of neural rosettes derived from human embryonic stem cells. Stem Cell Rev. *2*, 67–77.

Wu, J., Ocampo, A., and Belmonte, J.C.I. (2016). Cellular Metabolism and Induced Pluripotency. Cell *166*, 1371–1385.

Xia, J., and Wishart, D.S. (2010). MetPA: a web-based metabolomics tool for pathway analysis and visualization. Bioinformatics *26*, 2342–2344.

Xia, J., and Wishart, D.S. (2011a). Metabolomic data processing, analysis, and interpretation using MetaboAnalyst. Curr. Protoc. Bioinforma. *34*, 1–48.

Xia, J., and Wishart, D.S. (2011b). Web-based inference of biological patterns, functions and pathways from metabolomic data using MetaboAnalyst. Nat. Protoc. *6*, 743–760.

Xia, J., Psychogios, N., Young, N., and Wishart, D.S. (2009). MetaboAnalyst: a web server for metabolomic data analysis and interpretation. Nucleic Acids Res. *37*, W652–W660.

Zamanian, J.L., Xu, L., Foo, L.C., Nouri, N., Zhou, L., Giffard, R.G., and Barres, B.A. (2012). Genomic analysis of reactive astrogliosis. J. Neurosci. *32*, 6391–6410.

Zanotelli, M.R., Goldblatt, Z.E., Miller, J.P., Bordeleau, F., Li, J., VanderBurgh, J.A., Lampi, M.C., King, M.R., and Reinhart-King, C.A. (2018). Regulation of ATP utilization during metastatic cell migration by collagen architecture. Mol. Biol. Cell *29*, 1–9.

Zanotelli, M.R., Rahman-Zaman, A., VanderBurgh, J.A., Taufalele, P. V., Jain, A., Erickson, D., Bordeleau, F., and Reinhart-King, C.A. (2019). Energetic costs regulated by cell mechanics and confinement are predictive of migration path during decision-making. Nat. Commun. *10*, 1–12.

Zeisel, S.H. (2006). The fetal origins of memory: The role of dietary choline in optimal brain development. J. Pediatr. *149*, S131–S136.

Zeisel, S.H., and Niculescu, M.D. (2006). Perinatal Choline Influences Brain Structure and Function. Nutr. Rev. *64*, 197–203.

Zhang, S.-C., Wernig, M., Duncan, I.D., Brüstle, O., and Thomson, J.A. (2001). In vitro differentiation of transplantable neural precursors from human embryonic stem cells. Nat. Biotechnol. *19*, 1129–1133.

Zheng, X., Boyer, L., Jin, M., Kim, Y., Fan, W., Bardy, C., Berggren, T., Evans, R.M., Gage, F.H., and Hunter, T. (2016a). Alleviation of neuronal energy deficiency by mtor inhibition as a treatment for mitochondria-related neurodegeneration. Elife *5*.

Zheng, X., Boyer, L., Jin, M., Mertens, J., Kim, Y., Ma, L., Ma, L., Hamm, M., Gage, F.H., and Hunter, T. (2016b). Metabolic reprogramming during neuronal differentiation from aerobic glycolysis to neuronal oxidative phosphorylation. Elife *5*.

Figure 1

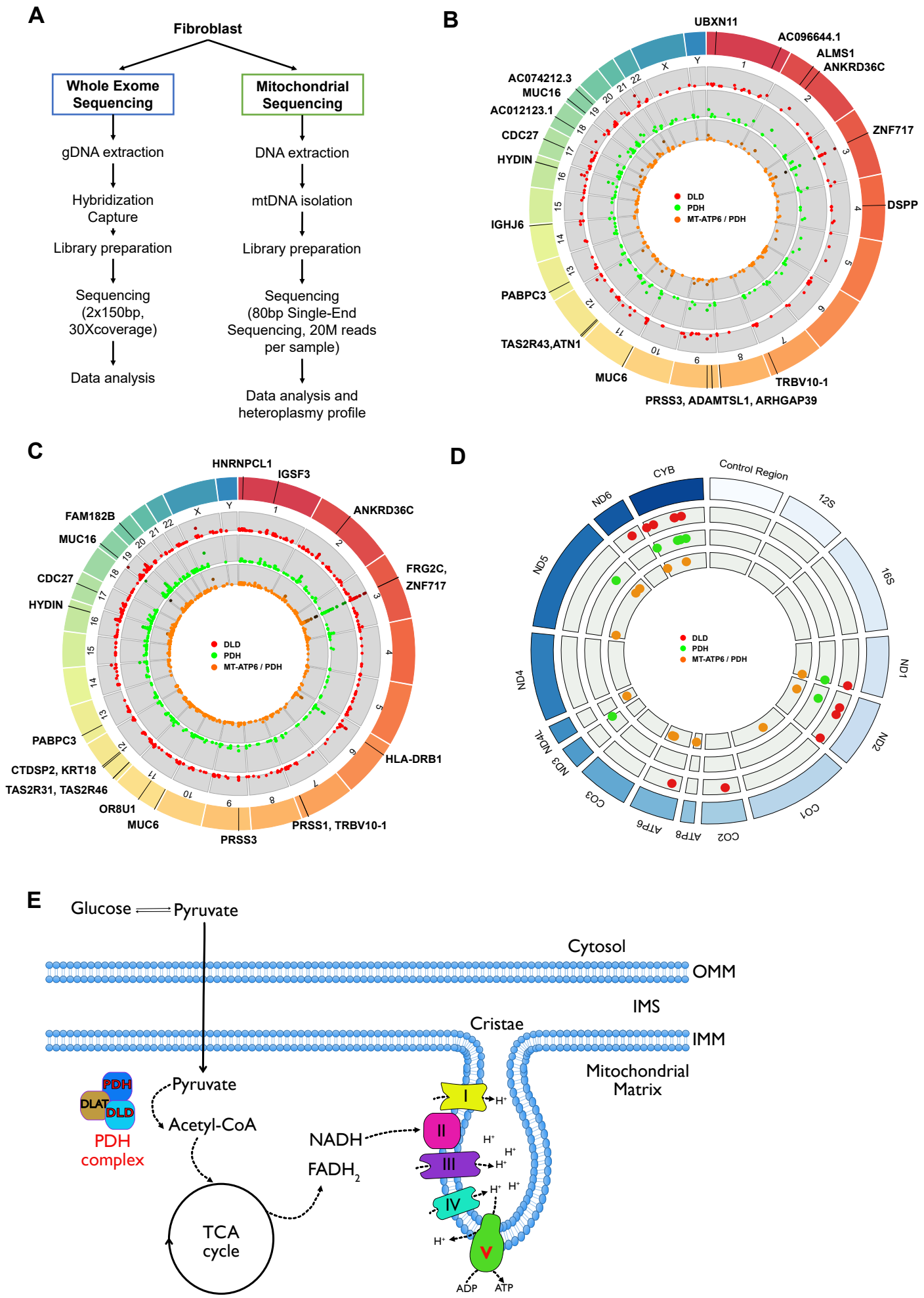
A
Fibroblast
Whole Exome Sequencing
Mitochondrial Sequencing
gDNA extraction
Hybridization Capture
Library preparation
Sequencing (2x150bp, 30Xcoverage)
Data analysis
DNA extraction
mtDNA isolation
Library preparation
Sequencing (80bp Single-End Sequencing, 20M reads per sample)
Data analysis and heteroplasmy profile
B
UBXN11
AC096644.1
ALMS1
ANKRD36C
ZNF717
DSPP
TRBV10-1
PRSS3, ADAMTSL1, ARHGAP39
MUC6
TAS2R43,ATN1
PABPC3
IGHJ6
HYDIN
CDC27
AC012123.1
MUC16
AC074212.3
DLD
PDH
MT-ATP6 / PDH
C
HNRNPCL1
IGSF3
ANKRD36C
FRG2C, ZNF717
HLA-DRB1
PRSS1, TRBV10-1
PRSS3
MUC6
OR8U1
TAS2R31, TAS2R46
CTDSP2, KRT18
PABPC3
HYDIN
CDC27
MUC16
FAM182B
DLD
PDH
MT-ATP6 / PDH
D
Control Region
12S
16S
ND1
ND2
CO1
CO2
ATP8
ATP6
CO3
ND3
ND4L
ND4
ND5
ND6
CYB
DLD
PDH
MT-ATP6 / PDH
E
Glucose
Pyruvate
Cytosol
OMM
IMS
Cristae
IMM
Mitochondrial Matrix
PDH
DLAT
DLD
PDH complex
Pyruvate
Acetyl-CoA
NADH
FADH2
TCA cycle
I
II
III
IV
V
H+
ADP
ATP

Figure 2

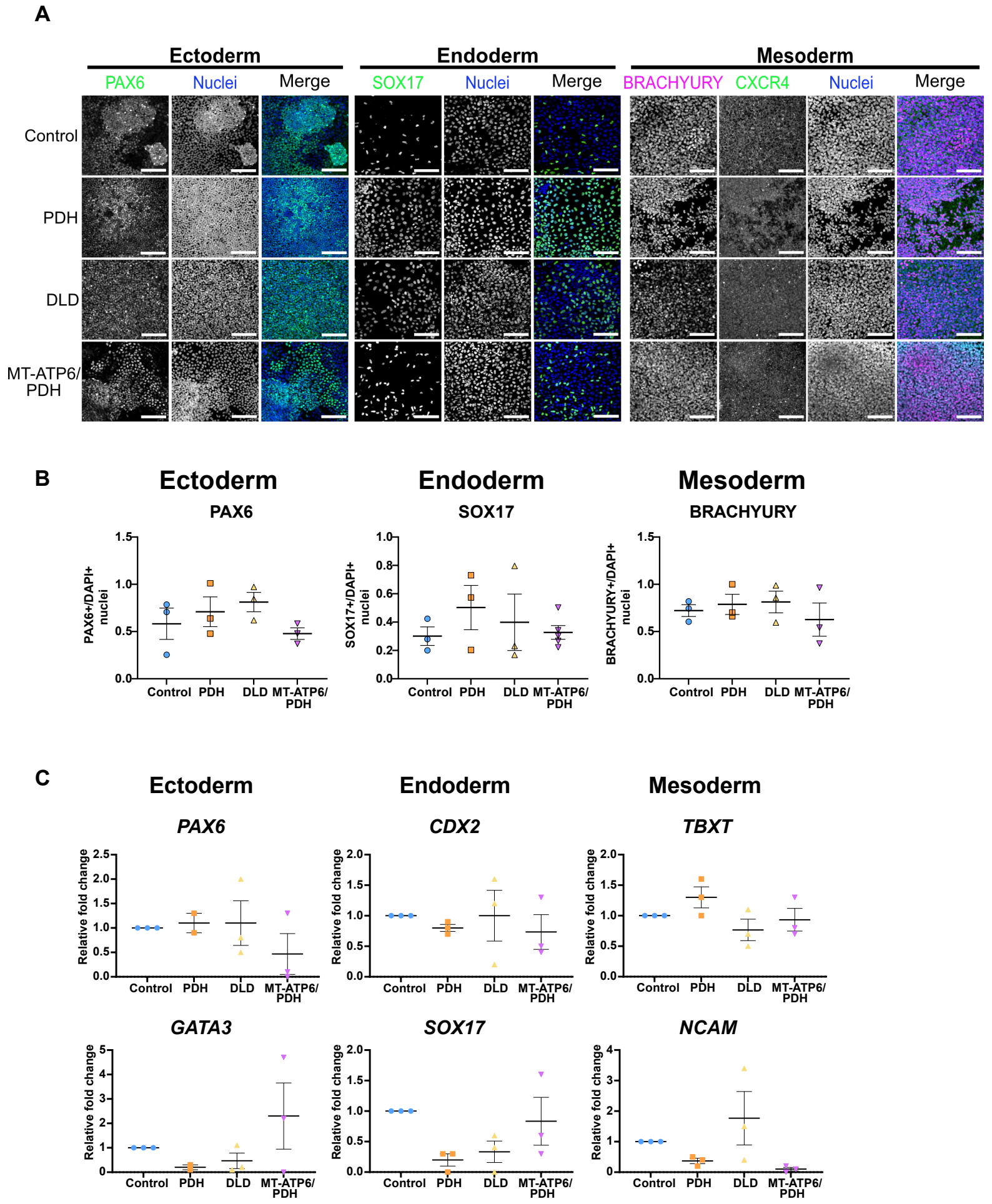
A
Ectoderm
Endoderm
Mesoderm
PAX6
Nuclei
Merge
SOX17
BRACHYURY
CXCR4
Control
PDH
DLD
MT-ATP6/ PDH
B
PAX6+/DAPI+ nuclei
SOX17+/DAPI+ nuclei
BRACHYURY+/DAPI+ nuclei
C
PAX6
CDX2
TBXT
GATA3
SOX17
NCAM
Relative fold change

Figure 3

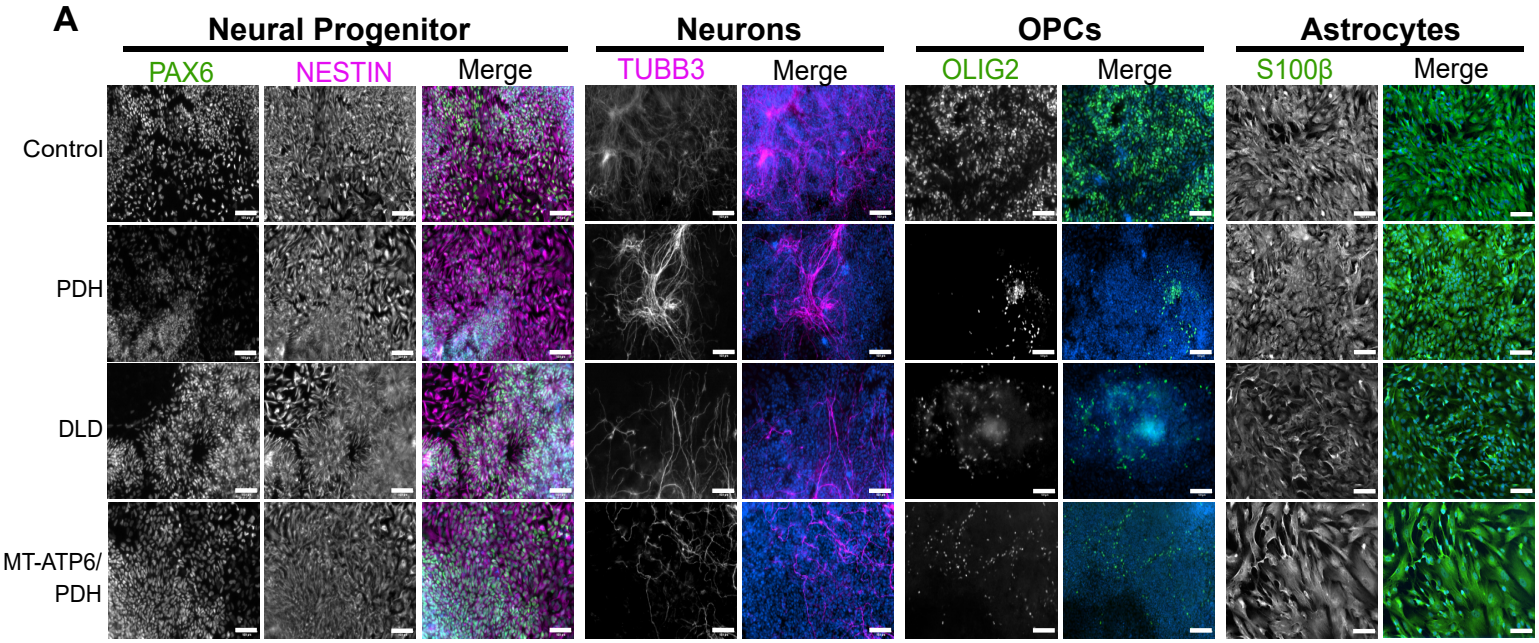
A
Neural Progenitor
Neurons
OPCs
Astrocytes
PAX6
NESTIN
Merge
TUBB3
Merge
OLIG2
Merge
S100β
Merge
Control
PDH
DLD
MT-ATP6/
PDH

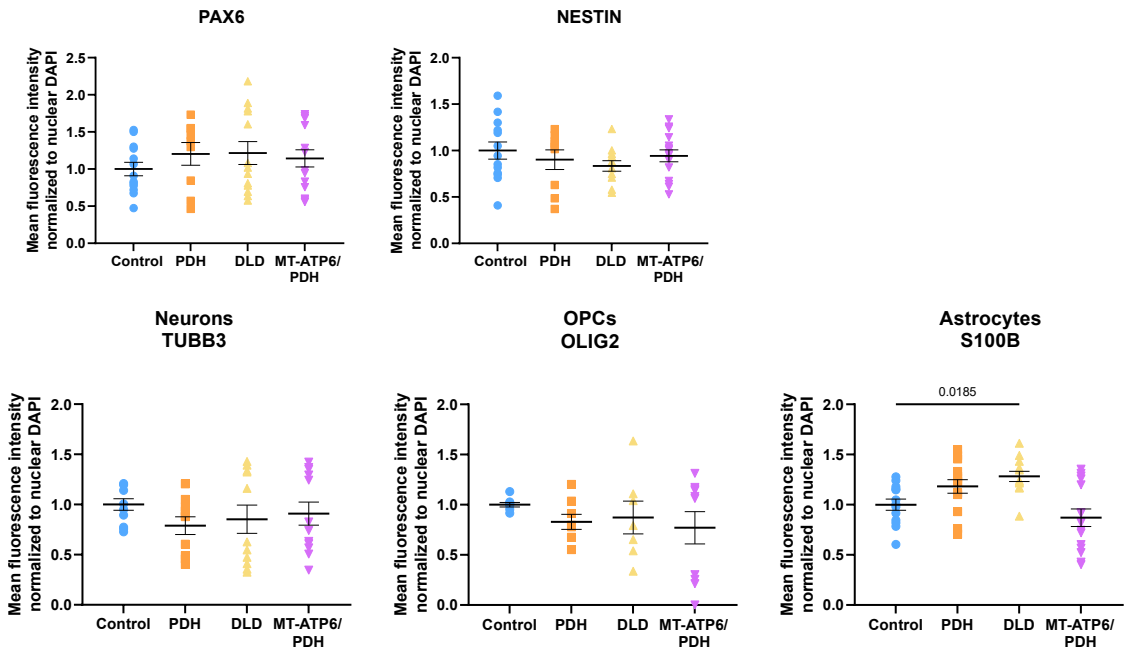
B
PAX6
NESTIN
Neurons
TUBB3
OPCs
OLIG2
Astrocytes
S100B
Mean fluorescence intensity normalized to nuclear DAPI
0.0185
Control
PDH
DLD
MT-ATP6/
PDH

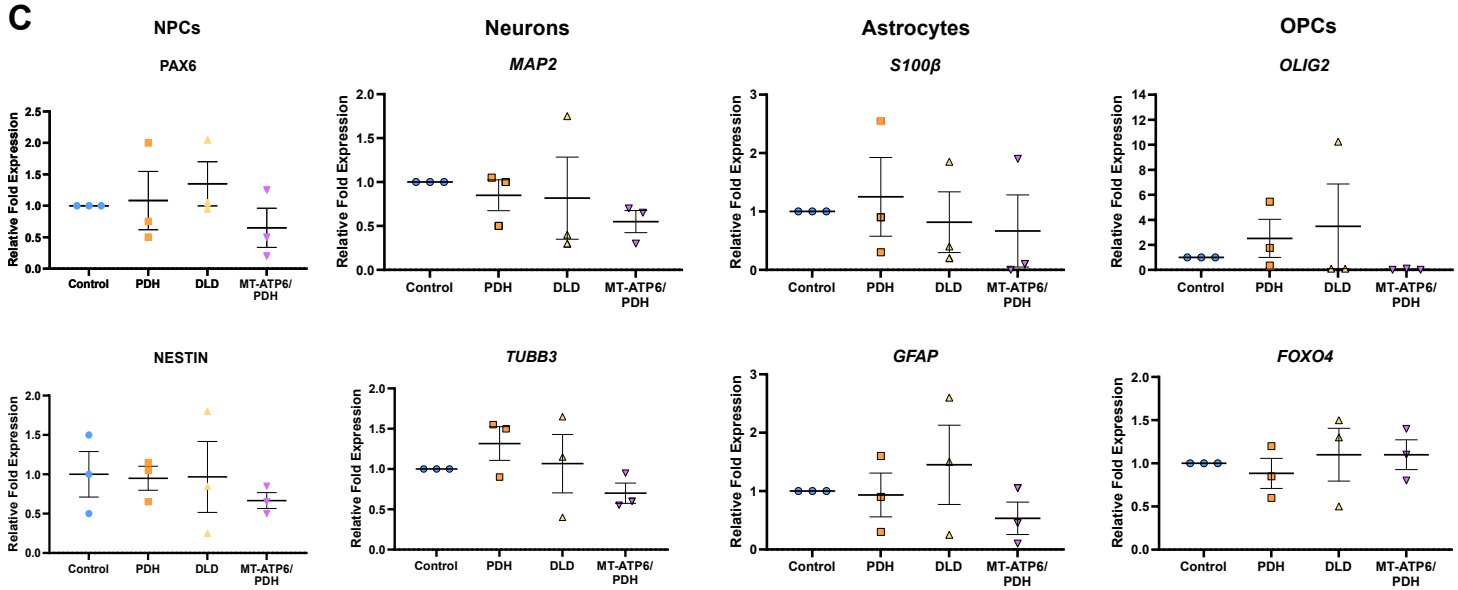
C
NPCs
PAX6
Neurons
MAP2
Astrocytes
S100β
OPCs
OLIG2
NESTIN
TUBB3
GFAP
FOXO4
Relative Fold Expression
Control
PDH
DLD
MT-ATP6/
PDH

Figure 4

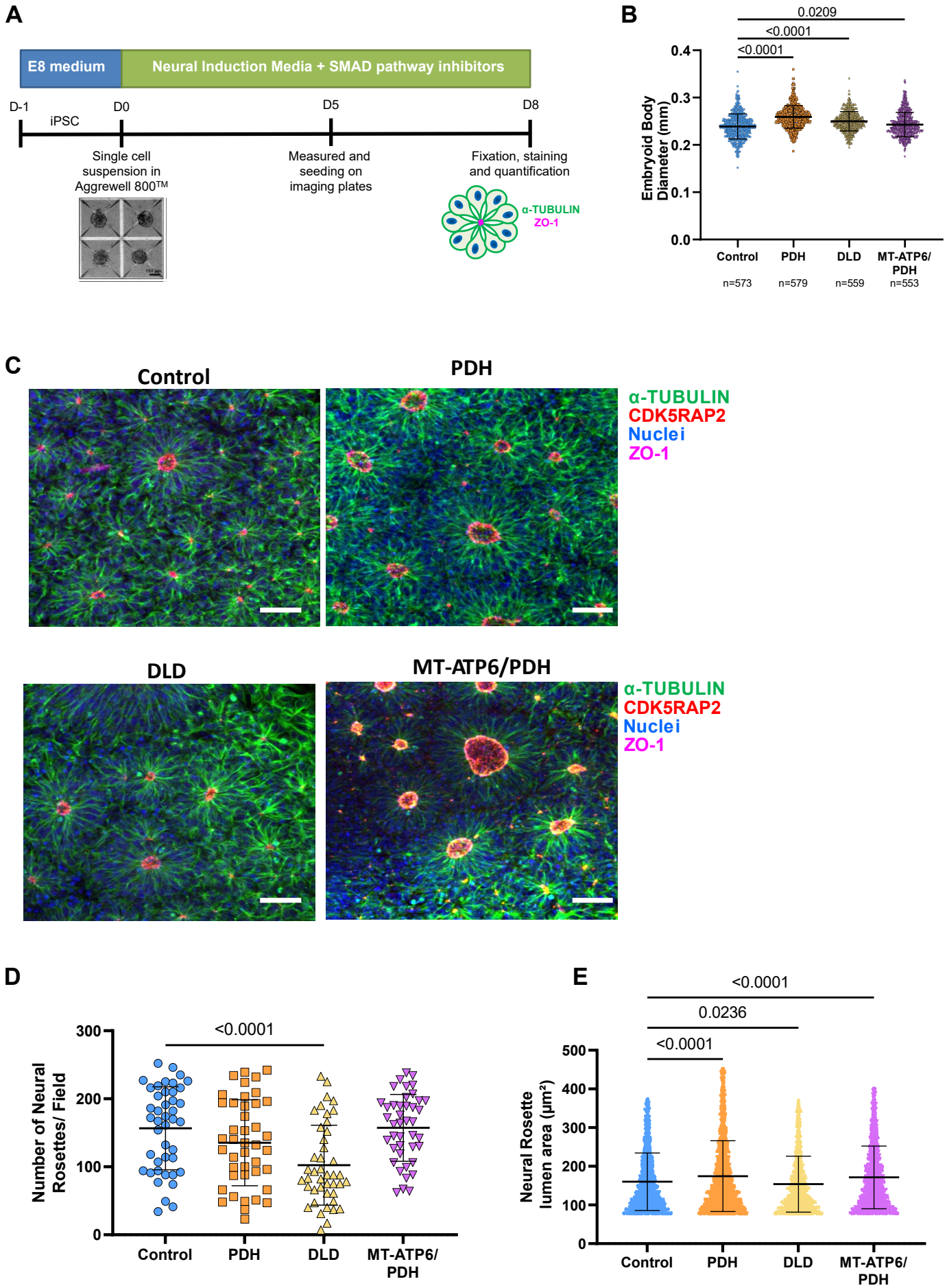
A
E8 medium
Neural Induction Media + SMAD pathway inhibitors
D-1
iPSC
D0
D5
D8
Single cell suspension in Aggrewell 800TM
Measured and seeding on imaging plates
Fixation, staining and quantification
α-TUBULIN
ZO-1
B
0.0209
<0.0001
<0.0001
Embryoid Body Diameter (mm)
0.4
0.3
0.2
0.1
0.0
Control
PDH
DLD
MT-ATP6/ PDH
n=573
n=579
n=559
n=553
C
Control
PDH
α-TUBULIN
CDK5RAP2
Nuclei
ZO-1
DLD
MT-ATP6/PDH
α-TUBULIN
CDK5RAP2
Nuclei
ZO-1
D
<0.0001
Number of Neural Rosettes/ Field
300
200
100
0
Control
PDH
DLD
MT-ATP6/ PDH
E
<0.0001
0.0236
<0.0001
Neural Rosette lumen area (μm²)
500
400
300
200
100
0
Control
PDH
DLD
MT-ATP6/ PDH

Figure 5

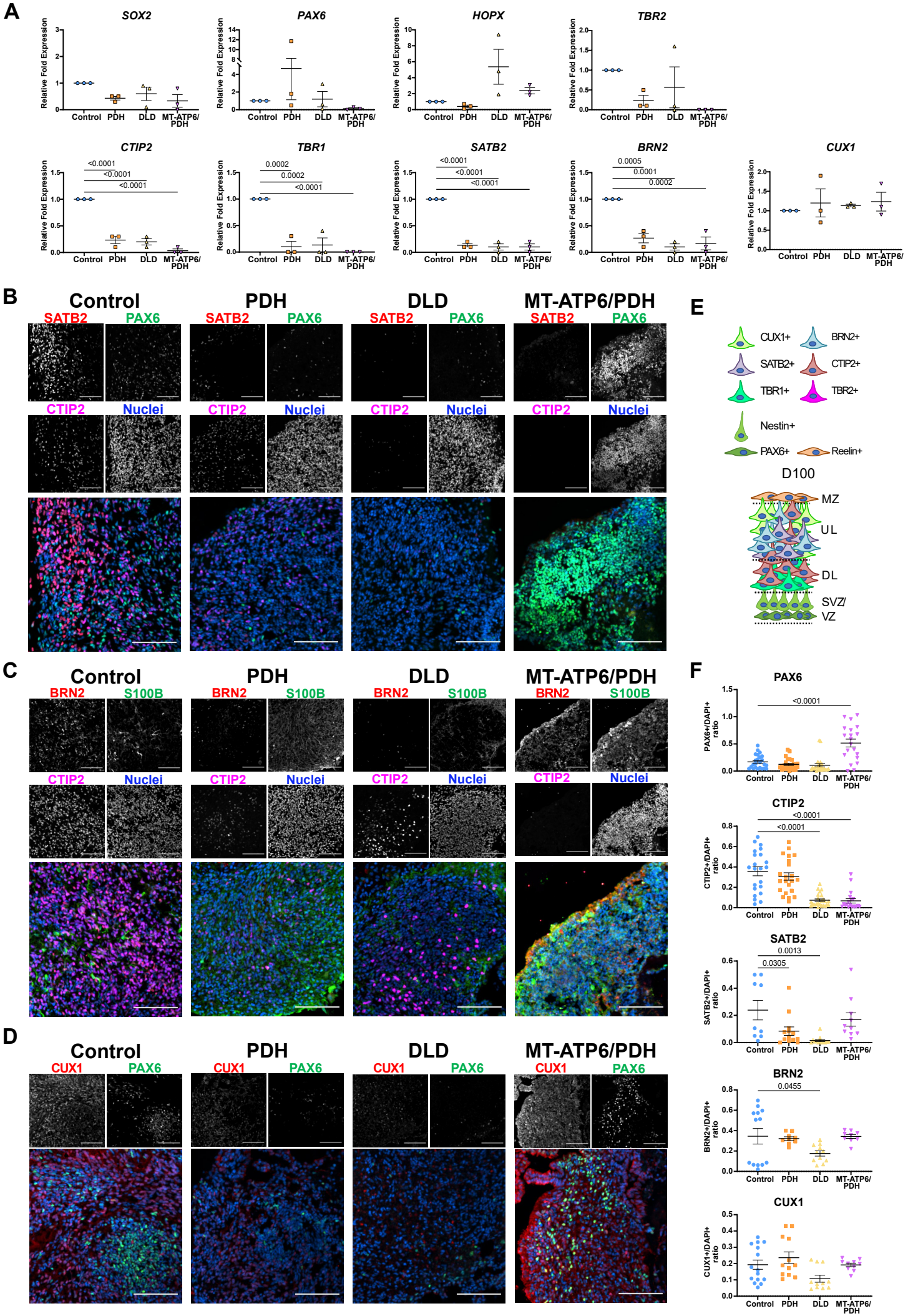
A
SOX2
PAX6
HOPX
TBR2
CTIP2
TBR1
SATB2
BRN2
CUX1
Relative Fold Expression
Control
PDH
DLD
MT-ATP6/PDH
<0.0001
0.0002
0.0005
0.0001
0.0455
B
Control
PDH
DLD
MT-ATP6/PDH
SATB2
PAX6
CTIP2
Nuclei
C
BRN2
S100B
D
CUX1
E
CUX1+
BRN2+
SATB2+
CTIP2+
TBR1+
TBR2+
Nestin+
PAX6+
Reelin+
D100
MZ
UL
DL
SVZ/
VZ
F
PAX6
CTIP2
SATB2
BRN2
CUX1
PAX6+/DAPI+ ratio
CTIP2+/DAPI+ ratio
SATB2+/DAPI+ ratio
BRN2+/DAPI+ ratio
CUX1+/DAPI+ ratio
0.0013
0.0305

Figure 6

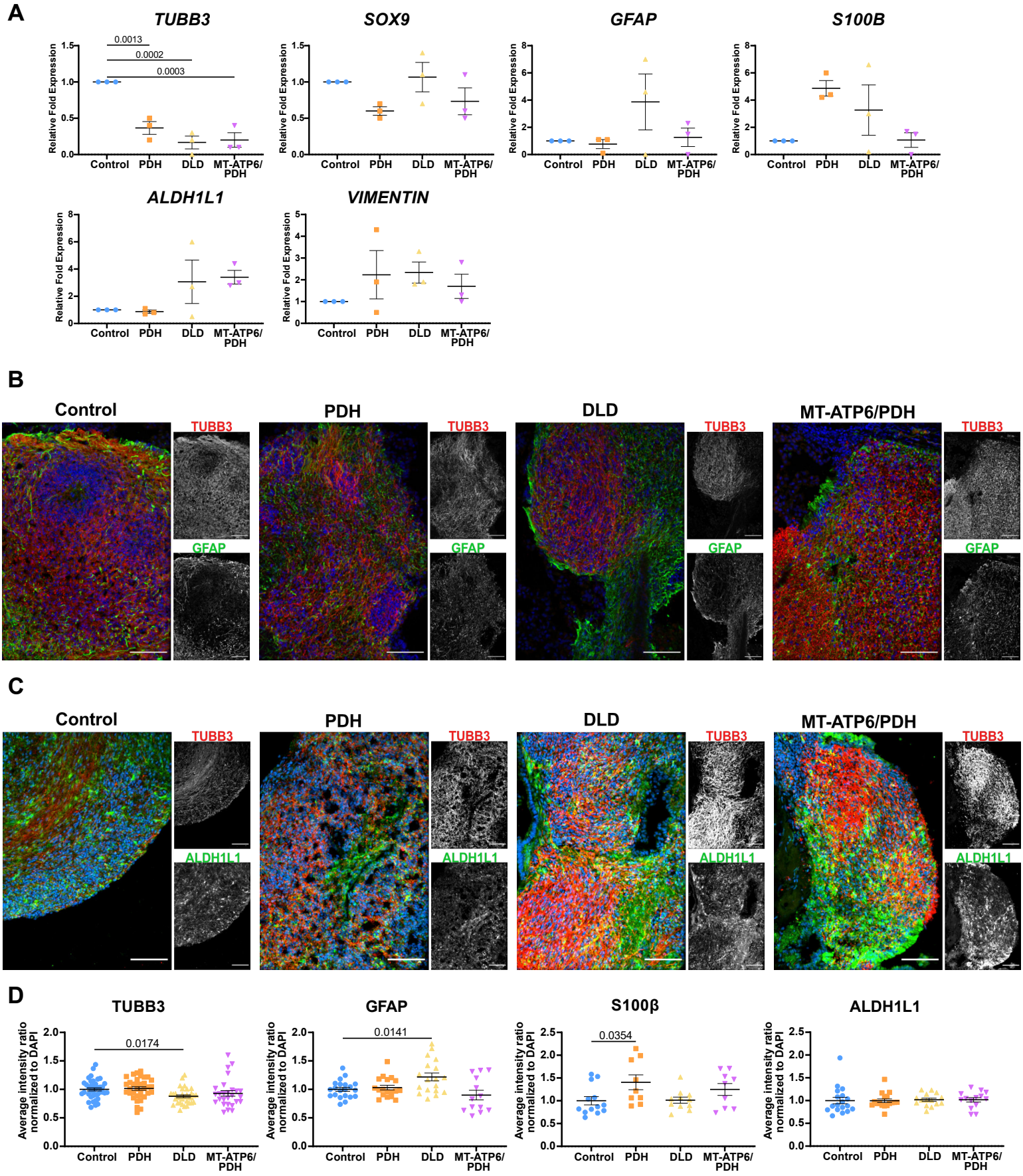
A
TUBB3
SOX9
GFAP
S100B
ALDH1L1
VIMENTIN
Relative Fold Expression
0.0013
0.0002
0.0003
Control
PDH
DLD
MT-ATP6/PDH
B
Control
PDH
DLD
MT-ATP6/PDH
TUBB3
GFAP
C
Control
PDH
DLD
MT-ATP6/PDH
TUBB3
ALDH1L1
D
TUBB3
GFAP
S100β
ALDH1L1
Average intensity ratio normalized to DAPI
0.0174
0.0141
0.0354

Figure 7

A

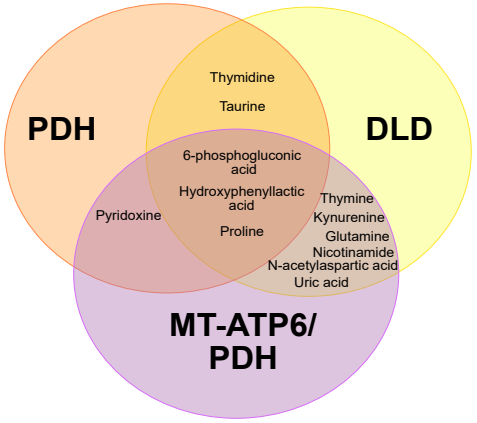

PDH	MT-ATP6/PDH		DLD
Deoxyuridine	NADP	Tyrosine	Sorbitol/Galactitol/L-iditol/Manitol
CDP-choline	Phenylalanine	Galactosamine/glucosamine	D-galactonic acid
	Leucine/isoleucine	Pyruvic acid	Guanosine
	Acetylcholine	N-acetylglucosamine 1/6-phosphate	Fructose-1-phosphate
	Lysine	DOPET	Deoxyinosine
	Cystine	Cysteine-S-sulfate	
	Alanine	Choline	
	Phosphoenolpyruvate	L-cysteic acid	
	Cytidine	3- / 7-methylguanine	
	Valine	D-sedoheptulose-7-phosphate	
	Pyrroline hydroxycarboxylic acid	Methionine	
	Histidine	DOPEG	

B PDH

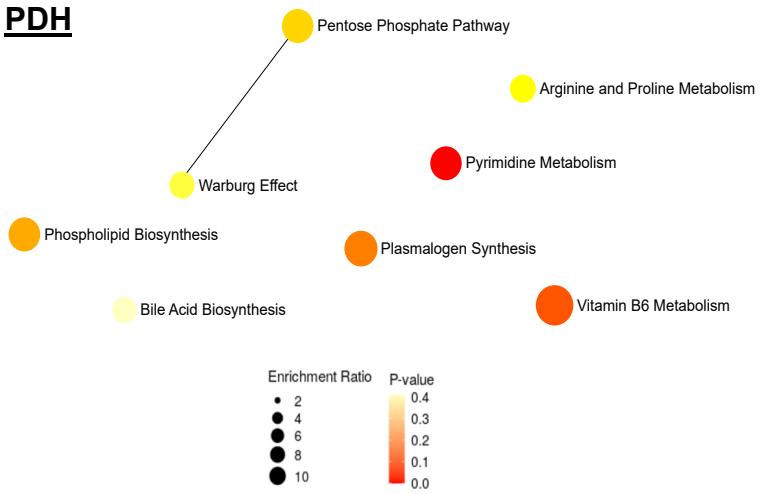

C DLD

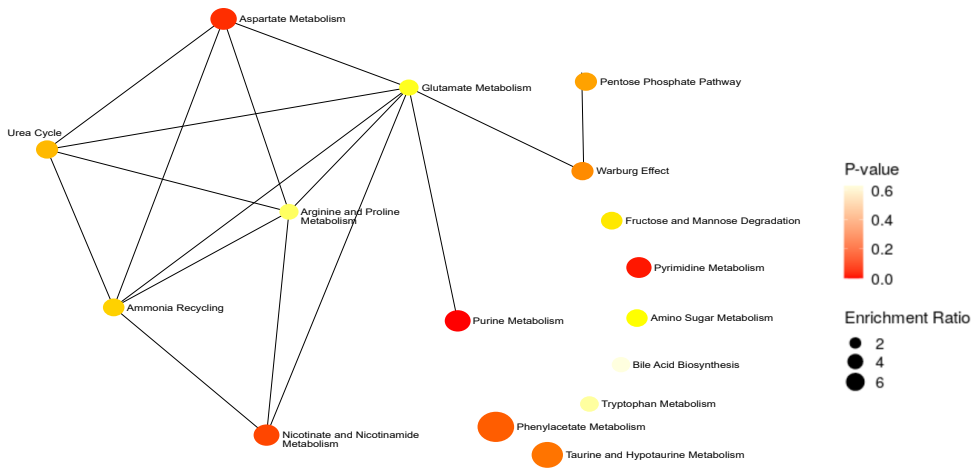

D MT-ATP6

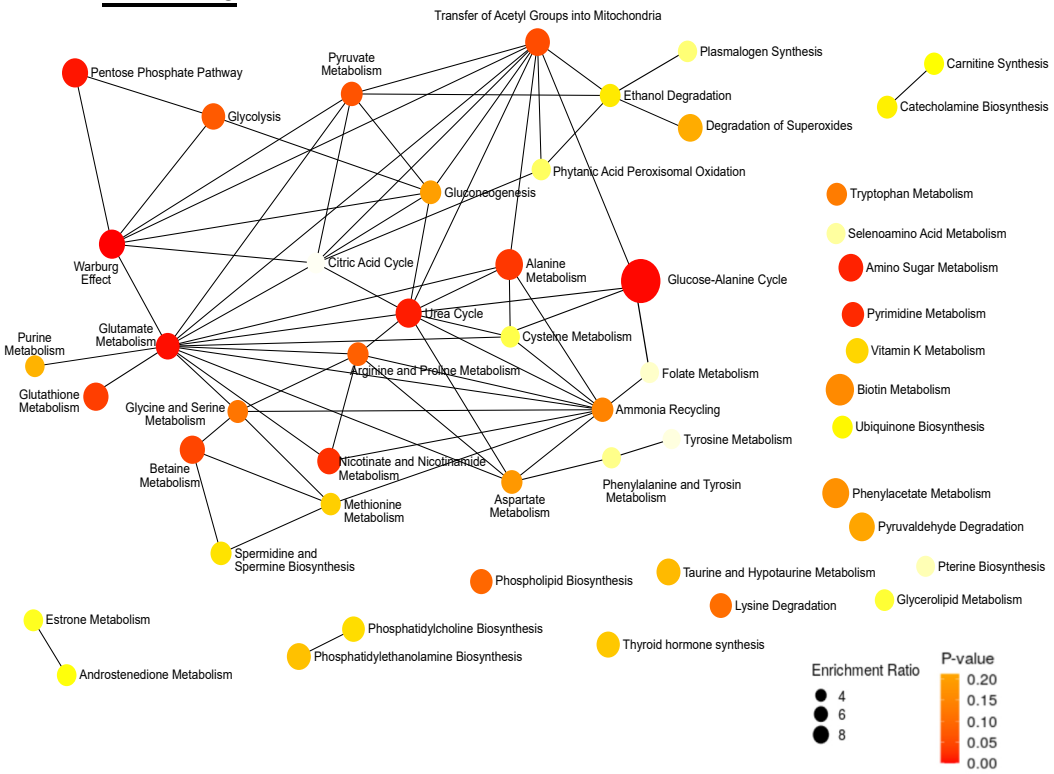

Supplemental Information

Supplemental Table 1, Related to Figure 1. Summary characteristics of the Leigh syndrome patient derived fibroblast cell lines including the patient phenotype at diagnosis, the mutations identified, and published literature using the cell line.

Supplemental Table 2, Related to Figure 7 and Supplemental Figure 7. Dysregulated metabolites in day 40 LS derived cerebral organoids. LC-MS measured metabolite peak areas were normalized to the total ion count (TIC) by sample and fold change was determined by dividing each LS TIC normalized peak area by the control TIC normalized peak area for each metabolite. One way ANOVA was utilized to identified metabolites that were significantly dysregulated ($p<0.05$). Post-hoc comparison column using Fisher's least significant difference method (Fisher's LSD) shows the comparisons between different levels that are significant given the p value threshold. Results shown are averages for 3 independent runs with 4 individual organoids per phenotype per run. FDR: False Discovery Rate.

Supplemental Table 3, Related to Related to Figure 7 and Supplemental Figure 7. Summary of the metabolic pathways analysis for metabolites enriched in day 40 PDH brain organoids. Statistical p values from enrichment analysis are adjusted for multiple hypothesis testing. Total: total number of compounds in the pathway. Hits: matched number from the uploaded data. Raw p: original p value calculated from the enrichment analysis. Holm p: p value adjusted by Holm-Bonferroni method. FDR p: adjusted p value using False Discovery Rate. Impact: pathway impact value calculated from pathway topology analysis.

Supplemental Table 4, Related to Related to Figure 7 and Supplemental Figure 7. Summary of the metabolic pathways analysis for metabolites enriched in day 40 DLD brain organoids. Statistical p values from enrichment analysis are adjusted for multiple hypothesis testing. Total: total number of compounds in the pathway. Hits: matched number from the uploaded data. Raw

p: original p value calculated from the enrichment analysis. Holm p: p value adjusted by Holm-Bonferroni method. FDR p: adjusted p value using False Discovery Rate. Impact: pathway impact value calculated from pathway topology analysis.

Supplemental Table 5, Related to Related to Figure 7 and Supplemental Figure 7. Summary of the metabolic pathways analysis for metabolites enriched in day 40 MT-ATP6/PDH brain organoids. Statistical p values from enrichment analysis are adjusted for multiple hypothesis testing. Total: total number of compounds in the pathway. Hits: matched number from the uploaded data. Raw p: original p value calculated from the enrichment analysis. Holm p: p value adjusted by Holm-Bonferroni method. FDR p: adjusted p value using False Discovery Rate. Impact: pathway impact value calculated from pathway topology analysis.

Supplemental Figure 1, Related to Figure 1. A-B. Venn diagram of the distribution of high, moderate and all impact annotations across samples for INDELs (A) and SNPs (B). Pie charts of the annotation distributions within samples. C. Top 15 genes with high impact SNP variants identified in the WES analysis. Number of overlapping SNPs per sample are denoted in as vertical bars, while the number of SNPs present in each phenotype are noted in the horizontal bars. *ZNF717*: Zinc finger protein 717, *HYDIN*: HYDIN axonemal central pair apparatus protein, *FRG2C*: FSHD region gene 2 family member C, *CDC27*: Cell division cycle 27, *TRBV10-1*: T cell receptor beta variable 10-1, *KIR2DL4*: Killer cell immunoglobulin like receptor, two Ig domains and long cytoplasmic tail 4, *ANKRD36C*: Ankyrin repeat domain 36C, *DUX4L6*: Double homeobox 4 like 6, *KIR3DL1*: Killer cell immunoglobulin like receptor, three Ig domains and long cytoplasmic tail 1, *DUX4L4*: Double homeobox 4 like 4 , *KIR2DL1*: Killer cell immunoglobulin like receptor, two Ig domains and long cytoplasmic tail 1, *KIR2DL3*: Killer cell immunoglobulin like receptor, two Ig domains and long cytoplasmic tail 3, *KRT18*: Keratin 18, *LDB3*: LIM domain binding 3, *MUC6*: Mucin 6.

Supplemental Figure 2, Related to Figure 2. Characterization of Leigh syndrome iPSCs. A. Schematic representation of the fibroblast reprogramming protocol. B-C. Pluripotency characterization of the LS iPSCs. Samples were analyzed against samples in a reference data set (The International Stem Cell Initiative, 2018) (B). The distribution of the samples compared with a non-iPSC control shows clustering of the samples in the high pluripotency and low novelty quadrant (C). D. qPCR for the pluripotency genes *POU5F1* and *NANOG (*$p < 0.001$*).* Fold change normalized to GPI and GAPDH as house-keeping genes. iPSC: induced pluripotent stem cells, NPC: neural progenitor cells, Multipot: neural multipotency differentiation.

Supplemental Figure 3, Related to Figure 3. Leigh syndrome derived NPCs are multipotent and do not present increased sensitivity to pharmacological stressors. A. Schematic of two-dimensional neural differentiation. B. Immunoblot of protein expression of neural markers PAX6,

NESTIN, and SOX2 (Left). Quantification of protein expression of neural markers PAX6, NESTIN and SOX2. Band density normalized to TUBULIN as a loading control (Right). C. Leigh syndrome NPCs do not show enhanced sensitivity towards different stressors. LS NPCs have similar cell viability compared to control when exposed to the DNA damaging agents etoposide and neocarzinostatin, the mitochondrial toxicant CCCP, and the microtubule destabilizer nocodazole.

Supplemental Figure 4. MT-ATP6/PDH brain organoids display defective differentiation at day 10. A. Schematic of the brain organoid generation protocol. B. Brightfield images (4X) of day 10 brain organoids. MT-ATP6/PDH shows disorganized cellular growth that do not resemble neuroepithelial buds. Scale bar: 300µm. C. Quantification of the defective organoids at day 10 by cell line. D. Brain organoid growth curves. LS derived brain organoids show reduction in size when grown for 100 days. * $p < 0.05$ for Control and PDH mutant; ǂ $p < 0.05$ for Control and DLD mutant, ɸ $p < 0.05$ for Control and MT-ATP6/PDH mutant.

Supplemental Figure 5. Leigh syndrome brain organoids show defects in SVZ/VZ and CP formation. A. qPCR quantification of the day 30 organoids. Neural progenitor cell populations were evaluated by the expression of *SOX2*, *PAX6* and *NESTIN*. Intermediate progenitor cells were identified with the marker *TBR2*. Marginal zone marker *REELIN*, cortical plate markers *TBR1* and *CTIP2*, and neuronal marker *TUBB3* were also evaluated. Fold change normalized to GPI and GAPDH as house-keeping genes. B. Schematic representation of the expected organization of the brain organoids on day 30. C-E. Representative immunostaining confocal images of day 30 brain organoids. MT-ATP6/PDH mutant presents severe disorganization of the SVZ/VZ markers PAX6 and TBR2, as well as the neural progenitor marker NESTIN (C). Cajal-Retzius neurons positive for REELIN were observed in the surface of the organoids (D). Cortical plate markers CTIP2 and TBR1 (D), as well as outer radial glia marker HOPX and the neuronal marker MAP2 (E). For E, nuclei in merge image correspond to the blue channel. Scale bar: 100µm. Images were generated from at least three different organoids per genotype from 3 independent

organoid batches. F. Quantification of day immunofluorescence staining for day 30 brain organoids. Outer radial glia marker HOPX was reduced PDH mutant ($p<0.0001$) and MT-ATP6/PDH mutant ($p=0.0417$) derived brain organoids. SVZ: subventricular zone, VZ: ventricular zone, CP: cortical plate, MZ: marginal zone

Supplemental Figure 6, Related to Figure 5. Leigh syndrome derived organoids show defects in mitochondrial morphology in the SVZ compartment. A. Representative confocal images of day 30 brain organoids showing mitochondrial morphology (TOM20). The red line divides the Sox2+ neural progenitor cells surrounding the lumen (L) from newly committed neurons. MT-ATP6/PDH mutant organoids show disorganization and fragmentation of the mitochondrial network compared to control. Scale bar: 10μm. B. Quantification of average mitochondrial volume, diameter, surface area, and major axis length are shown. Graphs represent mean ± SEM from at least three independent SVZs per phenotype from 3 independent organoid batches. Quantification was performed by 3D reconstruction of the mitochondrial network in interest. C. Representative super-resolution images of mitochondrial morphology (human anti-mitochondria) in LS and control NPCs. Scale bar: 5μm. D. Quantification of average mitochondrial number, volume, mitochondrial sphericity, and mitochondrial branching are shown, in which a spherical object would have a value of 1.0. Graphs represent mean ± SEM from at least three independent experiments ($n > 20$ cells per genotype).

Supplemental Figure 7, Related to Figure 7 and Supplemental Table 2. Day 40 LS organoids show changes in their metabolic profiles. Individual graph bars for the 43 metabolites identified as statistically dysregulated ($p<0.05$ and FDR of 0.01) in LS Organoids when compared to control. Statistical values can be found in Supplemental Table 2. A total of three batches of 40-day organoids per line (4 independent organoids per line per batch) were analyzed as described in methods.

Supplemental Figure 1

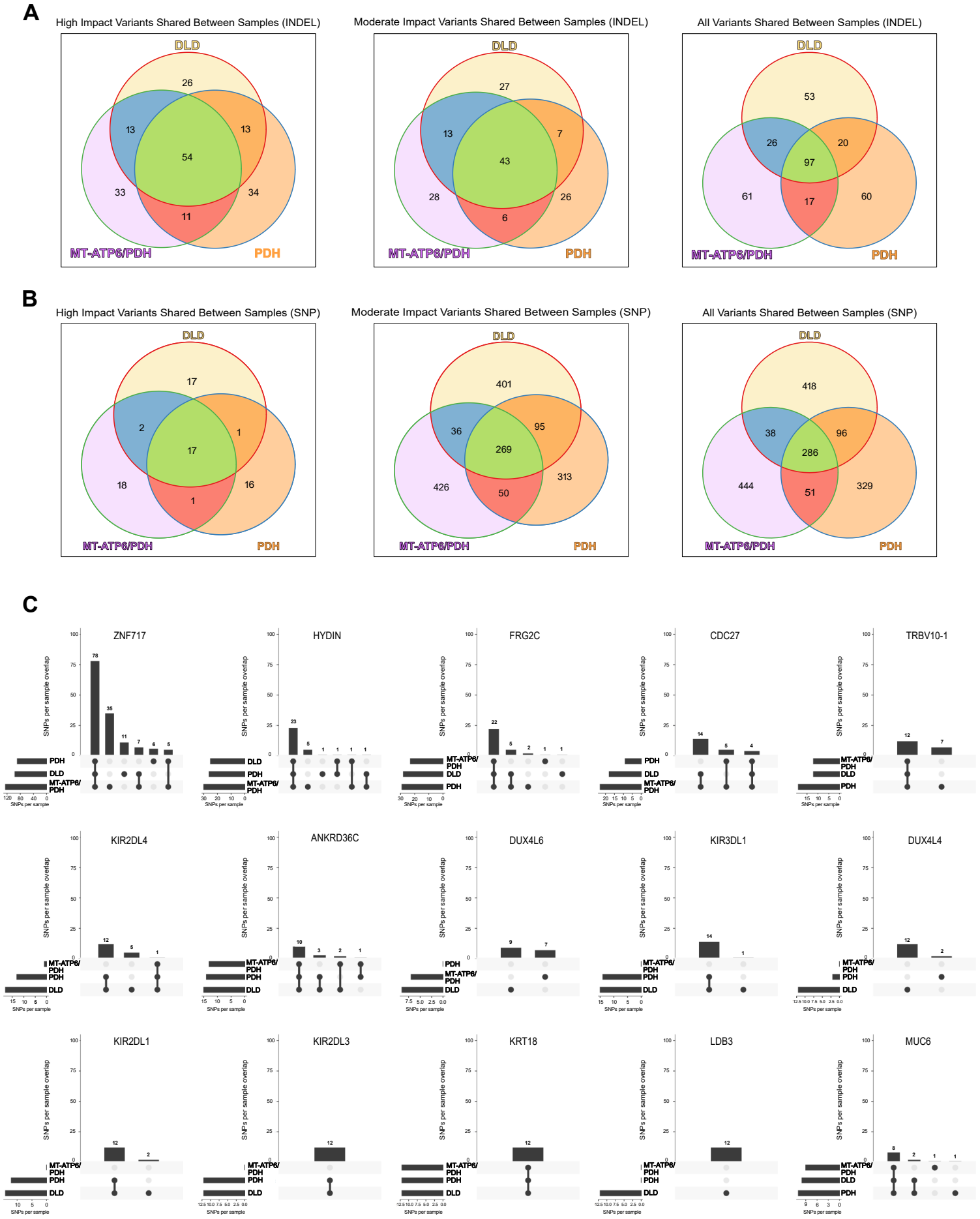

Supplemental Figure 2

A

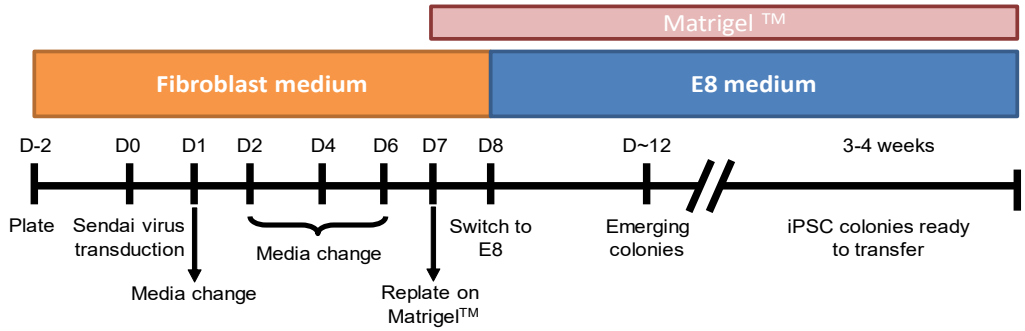

B

Sample	Pluritest Result	Pluricor	NovelCor
Control	Pass	38.62112	1.61562
PDH	Pass	37.78063	1.547368
DLD	Pass	36.43402	1.626429
MT-ATP6/ PDH	Pass	36.21865	1.509551
Non iPSC control	Fail	-48.9629	2.790166

C

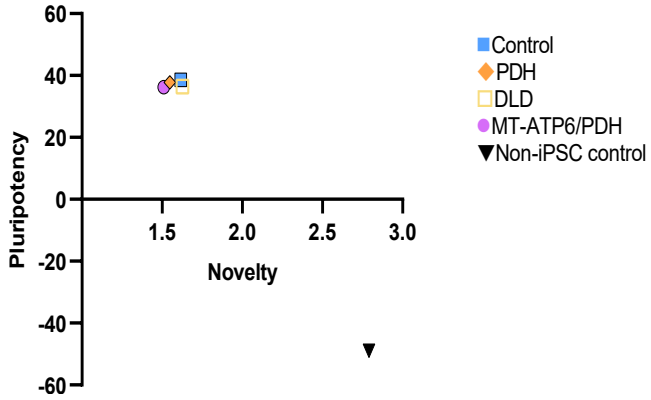

D

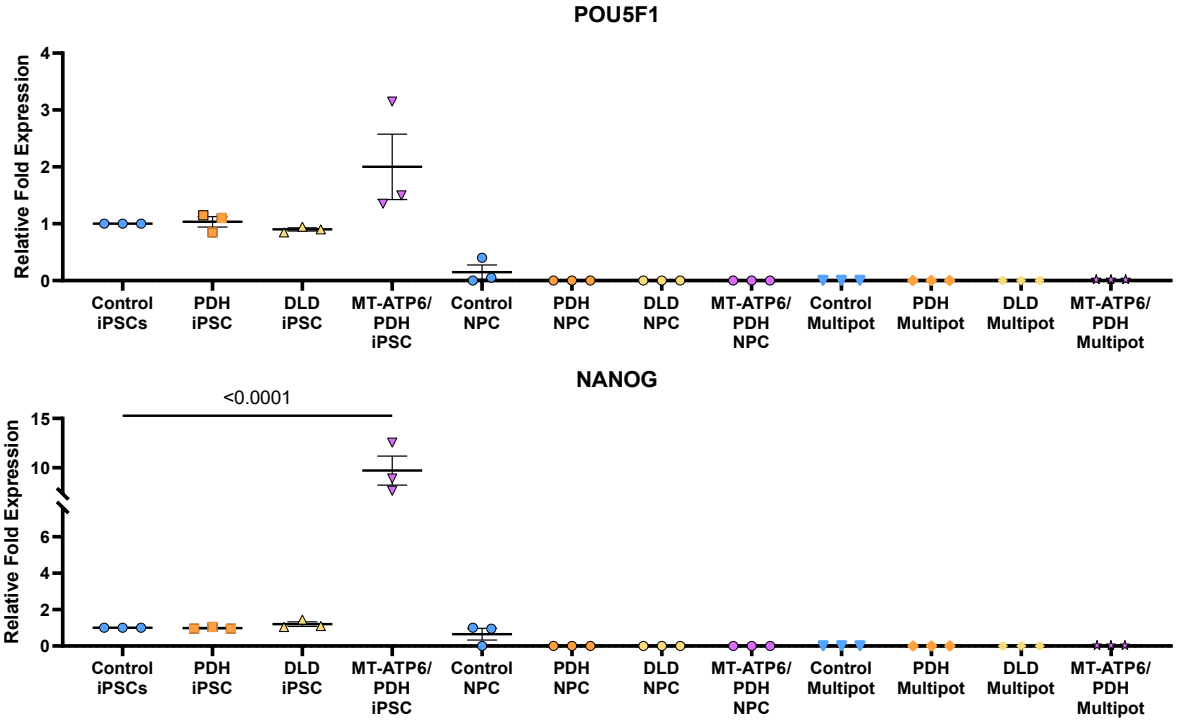

Supplemental Figure 3

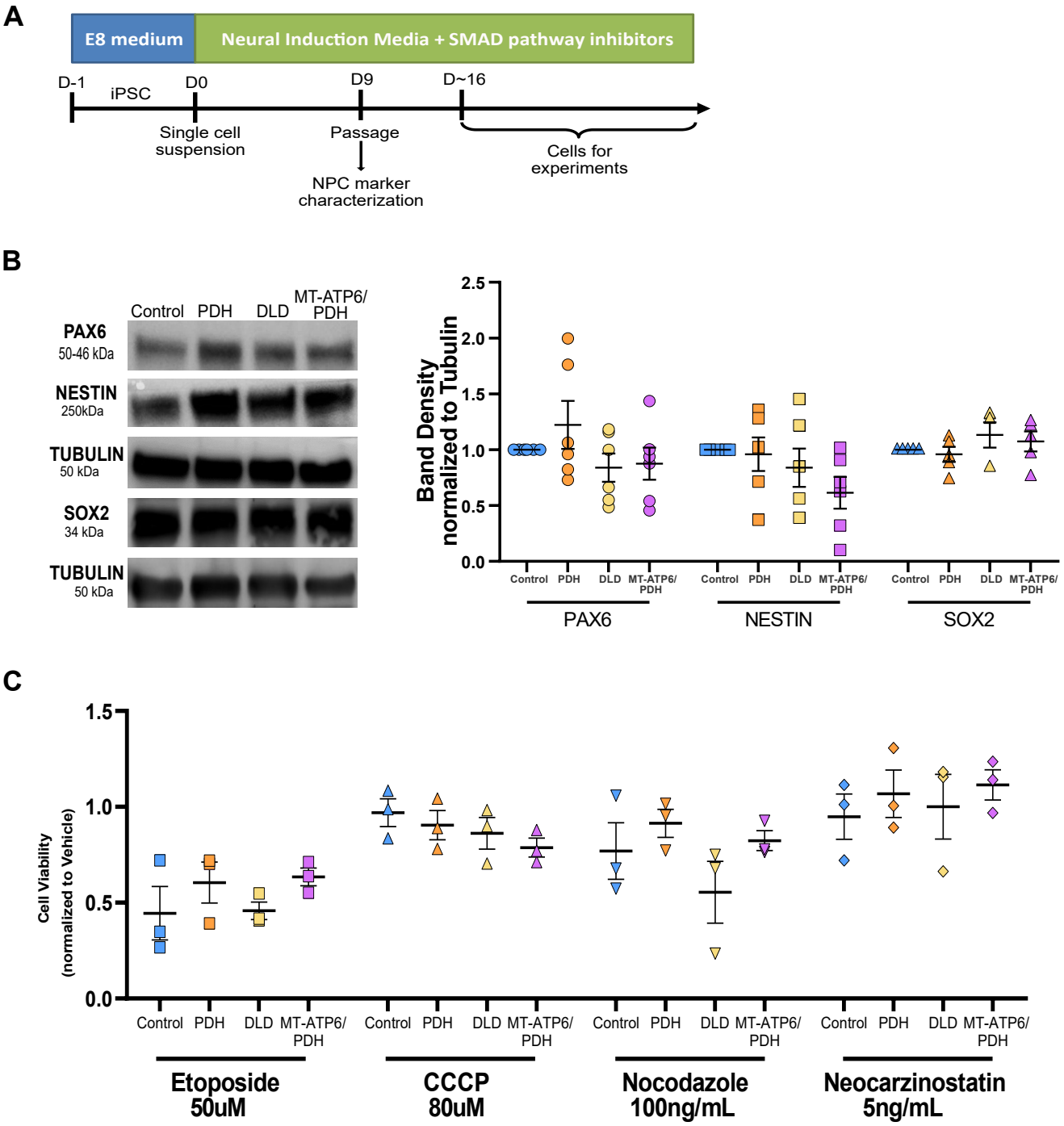

Supplemental Figure 4

A

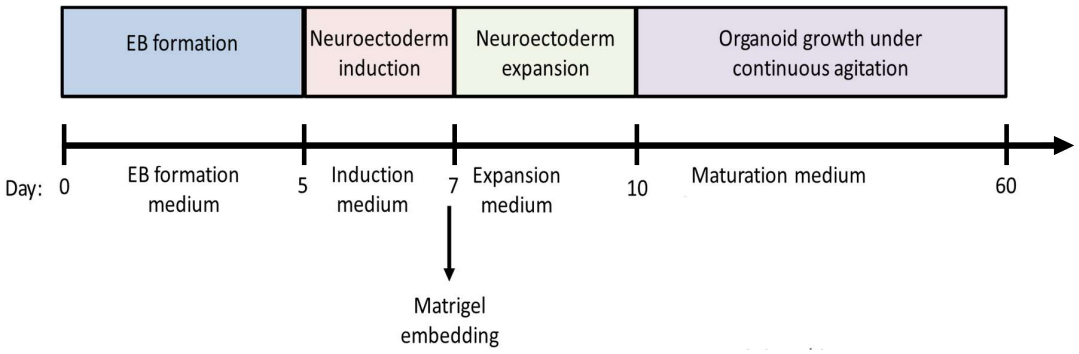

B

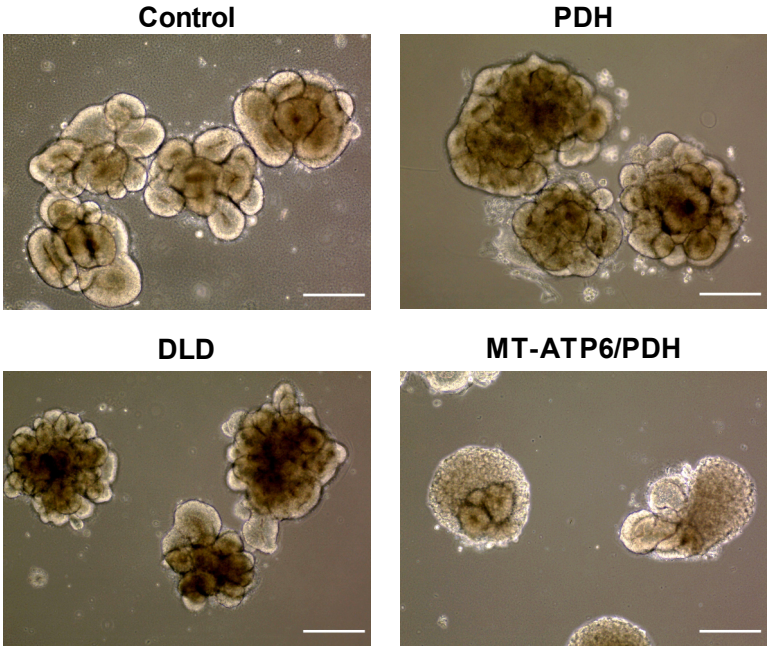

C

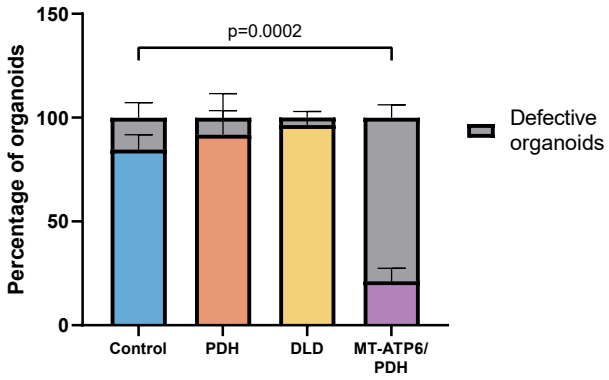

D

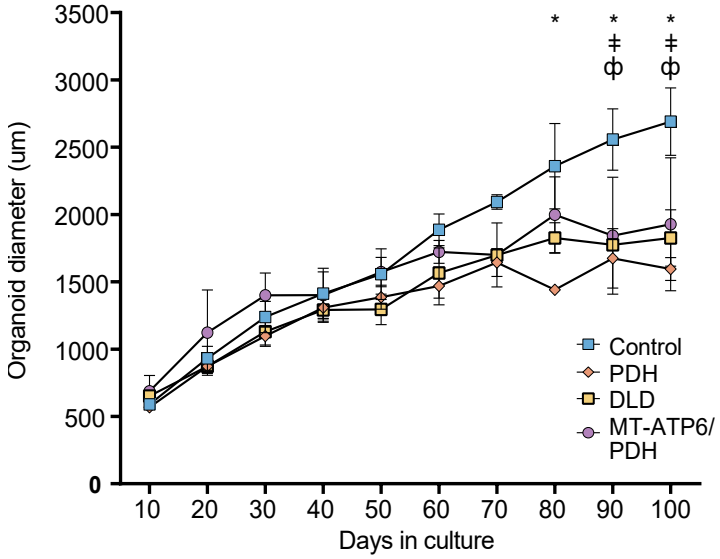

Supplemental Figure 5

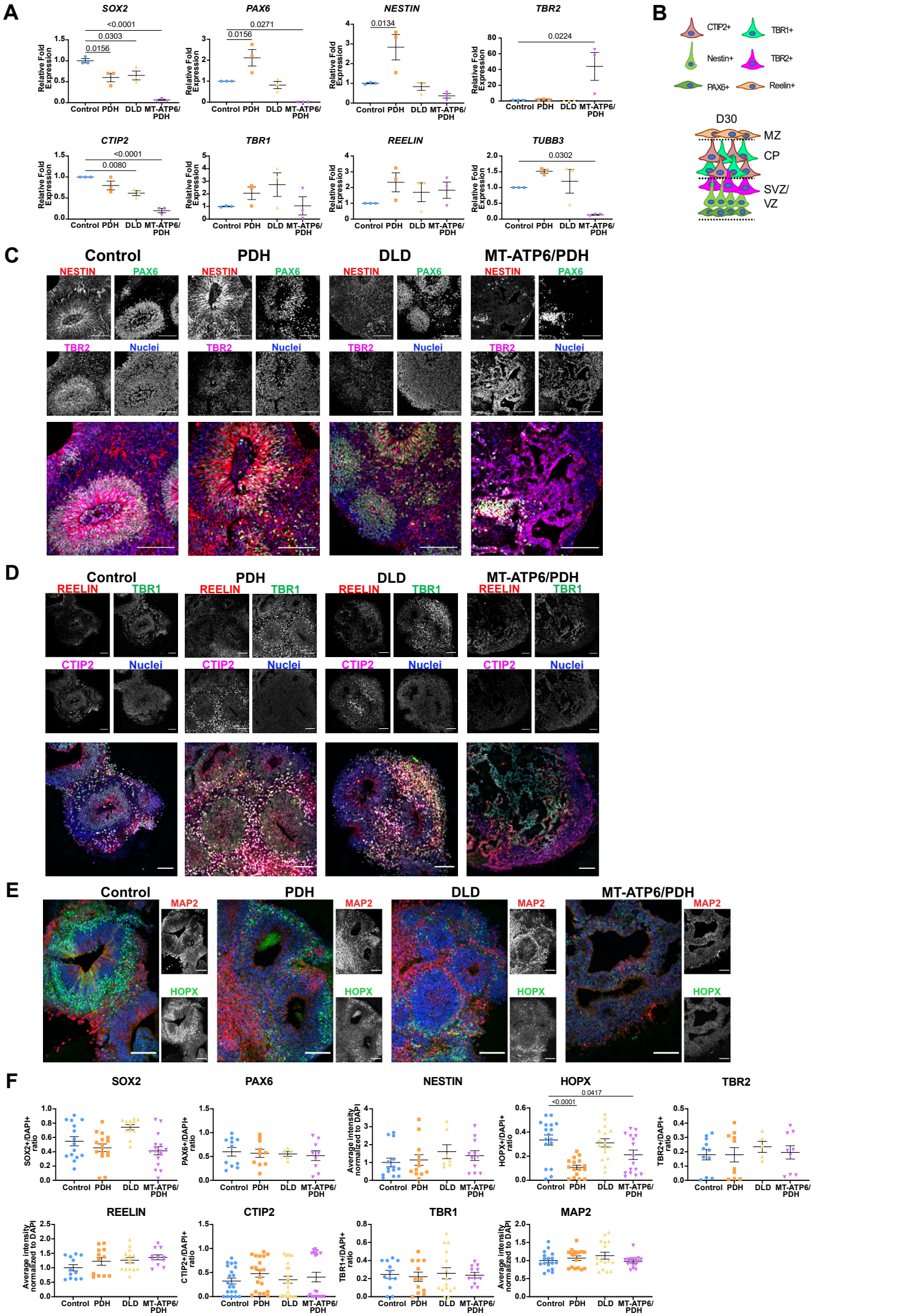

Supplemental Figure 6

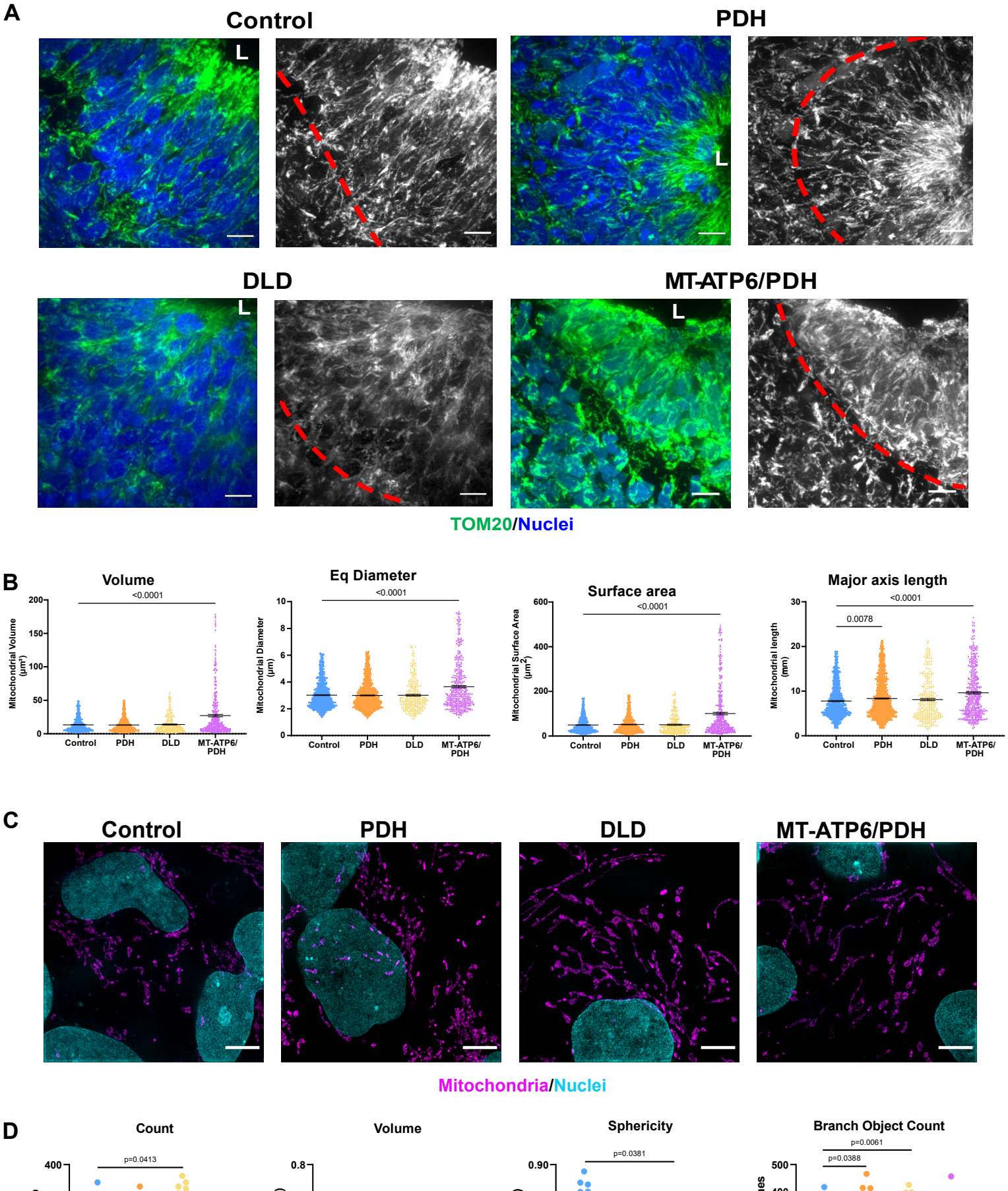

Supplemental Figure 7

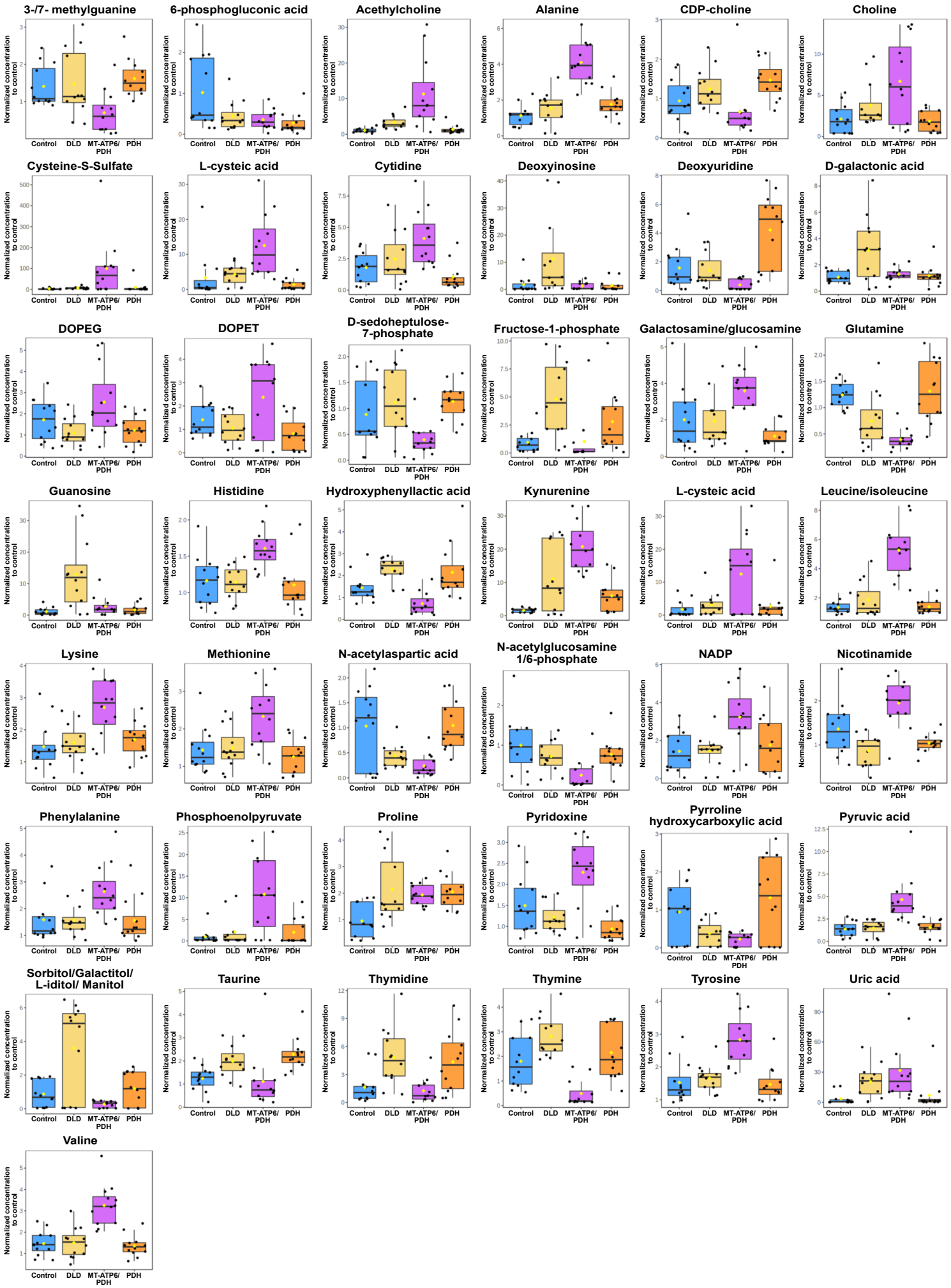

Supplemental Table 1

Cell line	Phenotype	Mutation	References
GM03672	1 y/o female, Caucasian. Developmental regression; microcephalic; elevated blood lactic acid and pyruvate; only affected family member	PDH (E1) LOF Pyruvate dehydrogenase (79delC, Arg27fs)	Hinman et al. 1989; Huh et al. 1990; Johnson et al. 2019
GM01503	3y/o female, Caucasian. Lactic acidosis, psychomotor delay; sister also affected. Subnormal activation of pyruvate dehydrogenase complex in disrupted fibroblasts	DLD (E3) Dihydrolipoamide dehydrogenase (A100G, Thr34Ala)	Cooper et al, 1969; Murphy JV, 1973; Sorbi& Blass, 1982; Hinman et al. 1989; Huh et al. 1990; Vo et al. 2007; Johnson et al. 2019
GM13411	8 month old male, Chinese. Lactic acidosis; developmental delay. Hypertrophic cardiomyopathy. Symmetric neural necrosis. Fibroblast: 90% heteroplasmy	MT-ATP6 (T8993G, Leu156Arg) PDH (E1) LOF Pyruvate dehydrogenase (79delC, Arg27fs)	Pastores et al. 1994; Iyer et al.2012; Ma et al. 2014; Galera-Monge et al. 2016; Zheng et al. 2016; Johnson et al. 2019

Supplemental Table 2

Metabolite	f.value	p.value	-LOG10(p)	FDR	Fisher's LSD
leucine / leucineiso	32.463	3.17E-11	10.499	7.00E-09	MT-ATP6/PDH - Control; MT-ATP6/PDH - DLD; MT-ATP6/PDH - PDH
alanine	28.604	2.04E-10	9.6912	2.25E-08	MT-ATP6/PDH - Control; MT-ATP6/PDH - DLD; MT-ATP6/PDH - PDH
valine	18.839	5.25E-08	7.2801	3.87E-06	MT-ATP6/PDH - Control; MT-ATP6/PDH - DLD; MT-ATP6/PDH - PDH
kynurenine	17.496	1.27E-07	6.896	7.02E-06	DLD - Control; MT-ATP6/PDH - Control; MT-ATP6/PDH - DLD; MT-ATP6/PDH - PDH
thymine	13.799	1.77E-06	5.7523	7.82E-05	DLD - Control; Control - MT-ATP6/PDH; DLD - MT-ATP6/PDH; PDH - MT-ATP6/PDH
tyrosine	13.55	2.14E-06	5.6703	7.87E-05	MT-ATP6/PDH - Control; MT-ATP6/PDH - DLD; MT-ATP6/PDH - PDH
glutamine	13.161	2.88E-06	5.5408	9.09E-05	Control - DLD; Control - MT-ATP6/PDH; DLD - MT-ATP6/PDH; PDH - DLD; PDH - MT-ATP6/PDH
pyruvic acid	12.95	3.39E-06	5.4697	9.37E-05	MT-ATP6/PDH - Control; MT-ATP6/PDH - DLD; MT-ATP6/PDH - PDH
nicotinamide	12.723	4.05E-06	5.3925	9.95E-05	Control - DLD; MT-ATP6/PDH - Control; MT-ATP6/PDH - DLD; MT-ATP6/PDH - PDH
deoxyuridine	12.392	5.26E-06	5.2794	0.00011615	PDH - Control; PDH - DLD; PDH - MT-ATP6/PDH
pyridoxine	11.7	9.16E-06	5.0381	0.00018405	MT-ATP6/PDH - Control; Control - PDH; MT-ATP6/PDH - DLD; MT-ATP6/PDH - PDH
sorbitol / galactitol / L-iditol / manitol	11.289	1.28E-05	4.8919	0.00023619	DLD - Control; DLD - MT-ATP6/PDH; DLD - PDH
acetylcholine	10.88	1.80E-05	4.7444	0.00030625	MT-ATP6/PDH - Control; MT-ATP6/PDH - DLD; MT-ATP6/PDH - PDH
guanosine	10.42	2.66E-05	4.5755	0.00041955	DLD - Control; DLD - MT-ATP6/PDH; DLD - PDH
hydroxyphenyllactic acid	10.302	2.94E-05	4.5318	0.00043306	DLD - Control; Control - MT-ATP6/PDH; PDH - Control; DLD - MT-ATP6/PDH; PDH - MT-ATP6/PDH
phosphoenolpyruvate	9.3744	6.59E-05	4.1812	0.00091016	MT-ATP6/PDH - Control; MT-ATP6/PDH - DLD; MT-ATP6/PDH - PDH
cystine	8.3901	0.00016027	3.7951	0.0020835	MT-ATP6/PDH - Control; MT-ATP6/PDH - DLD; MT-ATP6/PDH - PDH
N-acetylaspartic acid	8.239	0.00018425	3.7346	0.0022622	Control - DLD; Control - MT-ATP6/PDH; PDH - DLD; PDH - MT-ATP6/PDH
lysine	7.7264	0.00029759	3.5264	0.0034614	MT-ATP6/PDH - Control; MT-ATP6/PDH - DLD; MT-ATP6/PDH - PDH
methionine	6.9562	0.00062316	3.2054	0.0067872	MT-ATP6/PDH - Control; MT-ATP6/PDH - DLD; MT-ATP6/PDH - PDH
galactosamine / glucosamine	6.921	0.00064493	3.1905	0.0067872	MT-ATP6/PDH - Control; MT-ATP6/PDH - DLD; MT-ATP6/PDH - PDH
cytidine	6.8316	0.00070382	3.1525	0.0070702	MT-ATP6/PDH - Control; MT-ATP6/PDH - DLD; MT-ATP6/PDH - PDH
histidine	6.6085	0.00087664	3.0572	0.0084224	MT-ATP6/PDH - Control; MT-ATP6/PDH - DLD; MT-ATP6/PDH - PDH
L-cysteic acid	6.5655	0.00091465	3.0387	0.0084224	MT-ATP6/PDH - Control; MT-ATP6/PDH - DLD; MT-ATP6/PDH - PDH
pyrroline hydroxycarboxylic acid	6.3042	0.0011864	2.9258	0.010293	Control - MT-ATP6/PDH; PDH - DLD; PDH - MT-ATP6/PDH
D-galactonic acid	6.2562	0.0012448	2.9049	0.010293	DLD - Control; DLD - MT-ATP6/PDH; DLD - PDH
thymidine	6.2461	0.0012575	2.9005	0.010293	DLD - Control; PDH - Control; DLD - MT-ATP6/PDH; PDH - MT-ATP6/PDH
choline	6.1696	0.0013579	2.8671	0.010718	MT-ATP6/PDH - Control; MT-ATP6/PDH - DLD; MT-ATP6/PDH - PDH
F1P	6.0835	0.001481	2.8295	0.011286	DLD - Control; DLD - MT-ATP6/PDH
proline	5.6016	0.0024208	2.616	0.017833	DLD - Control; MT-ATP6/PDH - Control; PDH - Control
taurine	5.3747	0.0030613	2.5141	0.021824	DLD - Control; PDH - Control; DLD - MT-ATP6/PDH; PDH - MT-ATP6/PDH
6-phosphogluconic acid	5.202	0.0036652	2.4359	0.025313	Control - DLD; Control - MT-ATP6/PDH; Control - PDH
NADP	5.1267	0.0039663	2.4016	0.026562	MT-ATP6/PDH - Control; MT-ATP6/PDH - DLD; MT-ATP6/PDH - PDH
uric acid	4.9978	0.0045425	2.3427	0.027934	DLD - Control; MT-ATP6/PDH - Control; MT-ATP6/PDH - PDH
phenylalanine	4.9917	0.0045714	2.3399	0.027934	MT-ATP6/PDH - Control; MT-ATP6/PDH - DLD; MT-ATP6/PDH - PDH
deoxyinosine	4.981	0.0046237	2.335	0.027934	DLD - Control; DLD - MT-ATP6/PDH; DLD - PDH
D-sedoheptulose-7-phosphate	4.9702	0.0046767	2.3301	0.027934	Control - MT-ATP6/PDH; DLD - MT-ATP6/PDH; PDH - MT-ATP6/PDH
DOPET	4.9279	0.0048903	2.3107	0.028441	MT-ATP6/PDH - Control; MT-ATP6/PDH - DLD; MT-ATP6/PDH - PDH
cysteine-S-sulfate	4.8891	0.0050957	2.2928	0.028876	MT-ATP6/PDH - Control; MT-ATP6/PDH - DLD; MT-ATP6/PDH - PDH
3- / 7-methylguanine	4.8504	0.0053089	2.275	0.029331	Control - MT-ATP6/PDH; DLD - MT-ATP6/PDH; PDH - MT-ATP6/PDH
N-acetylglucosamine 1/6-phosphate	4.8231	0.0054652	2.2624	0.029459	Control - MT-ATP6/PDH; DLD - MT-ATP6/PDH; PDH - MT-ATP6/PDH
DOPEG	4.4575	0.0080819	2.0925	0.042526	MT-ATP6/PDH - DLD; MT-ATP6/PDH - PDH
CDP-choline	4.3847	0.0087424	2.0584	0.044932	PDH - Control; DLD - MT-ATP6/PDH; PDH - MT-ATP6/PDH

Supplemental Table 3

Metabolite	Total	Expected	Hits	Raw p	-LOG10(p)	Holm adjust	FDR	Impact
Pyrimidine metabolism	39	0.20129	2	0.0157	1.8041	1	1	0.1172
Taurine and hypotaurine metaboli	8	0.04129	1	0.0406	1.391	1	1	0.4286
Vitamin B6 metabolism	9	0.046452	1	0.0456	1.3408	1	1	0.0784
Pentose phosphate pathway	22	0.11355	1	0.1083	0.96538	1	1	0.1196
Glycerophospholipid metabolism	36	0.18581	1	0.1717	0.76513	1	1	0.0193
Arginine and proline metabolism	38	0.19613	1	0.1805	0.74359	1	1	0.0778
Primary bile acid biosynthesis	46	0.23742	1	0.2146	0.66836	1	1	0.0076
Aminoacyl-tRNA biosynthesis	48	0.24774	1	0.2229	0.65181	1	1	0

Supplemental Table 4

Metabolite	Total	Expected	Hits	Raw p	-LOG10(p)	Holm adjust	FDR	Impact
Purine metabolism	65	0.62903	4	0.00271	2.5662	0.22805	0.228	0.0059
Pyrimidine metabolism	39	0.37742	3	0.00544	2.2645	0.45142	0.228	0.0971
Alanine, aspartate and glutamate metabc	28	0.27097	2	0.02858	1.5439	1	0.8	0.2003
D-Glutamine and D-glutamate metabolisr	6	0.058065	1	0.05677	1.2459	1	0.916	0
Nitrogen metabolism	6	0.058065	1	0.05677	1.2459	1	0.916	0
Taurine and hypotaurine metabolism	8	0.077419	1	0.07501	1.1249	1	0.916	0.4286
Aminoacyl-tRNA biosynthesis	48	0.46452	2	0.07632	1.1174	1	0.916	0
Arginine biosynthesis	14	0.13548	1	0.12779	0.89352	1	1	0
Nicotinate and nicotinamide metabolism	15	0.14516	1	0.1363	0.86549	1	1	0.1943
Fructose and mannose metabolism	20	0.19355	1	0.17774	0.75021	1	1	0.0304
Pentose phosphate pathway	22	0.2129	1	0.19379	0.71267	1	1	0.1196
Glyoxylate and dicarboxylate metabolism	32	0.30968	1	0.26974	0.56905	1	1	0
Arginine and proline metabolism	38	0.36774	1	0.31205	0.50578	1	1	0.0778
Tryptophan metabolism	41	0.39677	1	0.33233	0.47842	1	1	0.0942
Primary bile acid biosynthesis	46	0.44516	1	0.36491	0.43782	1	1	0.0076

Supplemental Table 5

Metabolite	Total	Expected	Hits	Raw p	-LOG10(p)	Holm adjust	FDR	Impact
Aminoacyl-tRNA biosynthesis	48	0.71226	6	4.35E-05	4.3617	0.0036523	0.0036523	0
Alanine, aspartate and glutamate metabolism	28	0.41548	4	0.00059684	3.2241	0.049538	0.025067	0.20032
Cysteine and methionine metabolism	33	0.48968	3	0.011653	1.9336	0.95556	0.32629	0.10446
Arginine and proline metabolism	38	0.56387	3	0.017166	1.7653	1	0.33051	0.13058
Nicotinate and nicotinamide metabolism	15	0.22258	2	0.019673	1.7061	1	0.33051	0.1943
Citrate cycle (TCA cycle)	20	0.29677	2	0.034034	1.4681	1	0.47648	0.04634
Pyruvate metabolism	22	0.32645	2	0.040643	1.391	1	0.48771	0.20684
Glycolysis / Gluconeogenesis	26	0.38581	2	0.055171	1.2583	1	0.54228	0.20594
Phenylalanine, tyrosine and tryptophan biosynthesis	4	0.059355	1	0.058102	1.2358	1	0.54228	0.5
Glyoxylate and dicarboxylate metabolism	32	0.47484	2	0.079815	1.0979	1	0.55522	0
Glycine, serine and threonine metabolism	33	0.48968	2	0.084213	1.0746	1	0.55522	0
D-Glutamine and D-glutamate metabolism	6	0.089032	1	0.085928	1.0659	1	0.55522	0
Nitrogen metabolism	6	0.089032	1	0.085928	1.0659	1	0.55522	0
Glycerophospholipid metabolism	36	0.53419	2	0.097841	1.0095	1	0.5848	0.02582
Pyrimidine metabolism	39	0.57871	2	0.11206	0.95053	1	0.5848	0.03727
Taurine and hypotaurine metabolism	8	0.11871	1	0.11297	0.94705	1	0.5848	0
Ubiquinone and other terpenoid-quinone biosynthesis	9	0.13355	1	0.1262	0.89895	1	0.5848	0
Tyrosine metabolism	42	0.62323	2	0.12681	0.89685	1	0.5848	0.13972
Phenylalanine metabolism	10	0.14839	1	0.13924	0.85624	1	0.5848	0
Biotin metabolism	10	0.14839	1	0.13924	0.85624	1	0.5848	0
Arginine biosynthesis	14	0.20774	1	0.18957	0.72223	1	0.75827	0
Purine metabolism	65	0.96452	2	0.25062	0.60098	1	0.9489	0
Selenocompound metabolism	20	0.29677	1	0.25982	0.58533	1	0.9489	0
Pentose phosphate pathway	22	0.32645	1	0.28191	0.54989	1	0.98669	0.11955
Lysine degradation	25	0.37097	1	0.31387	0.50324	1	1	0
Glutathione metabolism	28	0.41548	1	0.34447	0.46285	1	1	0.0018
Tryptophan metabolism	41	0.60839	1	0.46262	0.33477	1	1	0.09417